

Solar Activity Reconstruction from Historical Observations of Sunspots

Dissertation
zur Erlangung des akademischen Grades
doctor rerum naturalium
(Dr. rer. nat.)
in der Wissenschaftsdisziplin Astrophysik

eingereicht an der
Mathematisch-Naturwissenschaftlichen Fakultät
der Universität Potsdam

Senthamizh Pavai Valliappan

November 29, 2017



Leibniz-Institut für Astrophysik Potsdam
An der Sternwarte 16
14482 Potsdam



Universität Potsdam
Institut für Physik und Astronomie
Karl-Liebknecht-Strasse 24/25
14476 Potsdam-Golm

Table of contents

Abstract	1
Zusammenfassung	3
1 Introduction	5
1.1 The solar cycle	6
1.2 Solar cycle properties	9
1.3 Indices of solar activity	11
1.3.1 Sunspot number	11
1.3.2 Sunspot area	12
1.3.3 Solar irradiance	13
1.4 Indirect solar indices	14
1.4.1 Geomagnetic activity	14
1.4.2 Aurorae	15
1.4.3 Cosmogenic radionuclides	15
1.5 Reconstruction of solar activity	16
1.6 Solar dynamo	17
1.6.1 Babcock-Leighton solar dynamo	17
1.7 Surface flux transport model	19
2 Sunspot areas and tilt angles for solar cycles 7–10	27
2.1 Calibration of sunspot areas	28
2.1.1 Indirect umbral areas for 1831–1867	29
2.1.2 Indirect umbral areas for 1825–1830	31
2.1.3 Umbral areas from parallel observations	33
2.1.4 Final mapping of sunspot sizes	33
2.1.5 Distribution of sunspot area	33
2.2 Group definitions	36
2.3 Tilt angles of groups	40
2.3.1 Determination of tilt and separation	40
2.3.2 Sources of errors	40
2.3.3 Distribution and averages	43
2.4 Summary	48
3 Sunspot group tilt angle measurements from historical observations	51
3.1 Data set	52
3.2 Tilt angle distributions	53
3.2.1 Comparison of cycle-averaged tilt angles	55
3.3 Conclusions	57
4 Sunspot positions, areas, and group tilt angles for 1611–1631 from observations by Christoph Scheiner	59
4.1 Description of the Rosa Ursina and Prodrumus drawings	60
4.2 The coordinate system of the drawings of 1618–1631	64
4.3 The observations of 1611–1612	66
4.4 Accuracy of the positions and areas	68
4.5 Data format and butterfly diagram	71

4.6	Sunspot group tilt angles	72
4.7	Summary	73
5	Wings of the butterfly: Sunspot groups for 1826–2015	75
5.1	Data	75
5.2	Separation of the butterfly wings	77
5.3	Evolution of characteristic wing latitudes	79
5.4	Relation to wing strength	81
5.5	Wing lengths, overlaps and asymmetries	84
5.6	Summary	87
6	Conclusions	89
7	Outlook	93
	Bibliography	97
	Acknowledgments	113
	Appendix A – List of acronyms	115

Abstract

The solar activity and its consequences affect space weather and Earth's climate. The solar activity exhibits a cyclic behaviour with a period of about 11 years. The solar cycle properties are governed by the dynamo taking place in the interior of the Sun, and they are distinctive. Extending the knowledge about solar cycle properties into the past is essential for understanding the solar dynamo and forecasting space weather. It can be acquired through the analysis of historical sunspot drawings. Sunspots are the dark areas, which are associated with strong magnetic fields, on the solar surface. Sunspots are the oldest and longest available observed features of solar activity.

One of the longest available records of sunspot drawings is the collection by Samuel Heinrich Schwabe during 1825–1867. The sunspot sizes measured from digitized Schwabe drawings are not to scale and need to be converted into physical sunspot areas. We employed a statistical approach assuming that the area distribution of sunspots was the same in the 19th century as it was in the 20th century. Umbral areas for about 130 000 sunspots observed by Schwabe were obtained. The annually averaged sunspot areas correlate reasonably well with the sunspot number. Tilt angles and polarity separations of sunspot groups were calculated assuming them to be bipolar. There is, of course, no polarity information in the observations. We derived an average tilt angle by attempting to exclude unipolar groups with a minimum separation of the two surmised polarities and an outlier rejection method, which follows the evolution of each group and detects the moment, when it turns unipolar as it decays. As a result, the tilt angles, although displaying considerable natural scatter, are on average $5.85^\circ \pm 0.25^\circ$, with the leading polarity located closer to the equator, in good agreement with tilt angles obtained from 20th century data sets. Sources of uncertainties in the tilt angle determination are discussed and need to be addressed whenever different data sets are combined.

Digital images of observations printed in the books *Rosa Ursina* and *Prodromus pro sole mobili* by Christoph Scheiner, as well as the drawings from Scheiner's letters to Marcus Welser, are analyzed to obtain information on the positions and sizes of sunspots that appeared before the Maunder minimum. In most cases, the given orientation of the ecliptic is used to set up the heliographic coordinate system for the drawings. Positions and sizes are measured manually displaying the drawings on a computer screen. Very early drawings have no indication of the solar orientation. A rotational matching using common spots of adjacent days is used in some cases, while in other cases, the assumption that images were aligned with a zenith–horizon coordinate system appeared to be the most likely. In total, 8167 sunspots were measured. A distribution of sunspot latitudes versus time (butterfly diagram) is obtained for Scheiner's observations. The observations of 1611 are very inaccurate, but the drawings of 1612 have at least an indication of the solar orientation, while the remaining part of the spot positions from 1618–1631 have good to very good accuracy. We also computed 697 tilt angles of apparent bipolar sunspot groups, which were observed in the period 1618–1631. We find that the average tilt angle of nearly 4° does not significantly differ from the 20th century values.

The solar cycle properties seem to be related to the tilt angles of sunspot groups, and it is an important parameter in the surface flux transport models. The tilt angles of bipolar sunspot groups from various historical sets of solar drawings including from Schwabe and Scheiner are analyzed. Data by Scheiner, Hevelius, Staudacher, Zucconi, Schwabe, and Spörer deliver a series of average tilt angles spanning a period of 270 years, in addition to previously found values for 20th-century data obtained by other authors. We find that the average tilt angles before the Maunder minimum were not significantly different from modern values. However, the average tilt angles of a period 50 years after the Maunder minimum, namely for cycles 0 and 1, were much lower and near zero. The typical tilt angles before the Maunder minimum suggest that abnormally low tilt angles were not responsible for driving the solar cycle into a grand minimum.

With the Schwabe (1826–1867) and Spörer (1866–1880) sunspot data, the butterfly diagram of sunspot groups extends back till 1826. A recently developed method, which separates the wings of the butterfly diagram based on the long gaps present in sunspot group occurrences at different latitudinal bands, is used to separate the wings of the butterfly diagram. The cycle-to-cycle variation in the start (F), end (L), and highest (H) latitudes of the wings with respect to the strength of the wings are analyzed. On the whole, the wings of the stronger cycles tend to start at higher latitudes and have a greater extent. The time spans of the wings and the time difference between the wings in the northern hemisphere display a quasi-periodicity of 5–6 cycles. The average wing overlap is zero in the southern hemisphere, whereas it is 2–3 months in the north. A marginally significant oscillation of about 10 solar cycles is found in the asymmetry of the L latitudes. This latest, extended database of butterfly wings provides new observational constraints, regarding the spatio-temporal distribution of sunspot occurrences over the solar cycle, to solar dynamo models.

This doctoral thesis is a cumulative thesis, which is based on the first four refereed articles listed below. The articles were amended by including footnotes for clarification. The Mercury transit on 2016 May 9 was observed from the solar observatory Einstein Tower, and I was in team carrying out the observations. The transit observations are included in the fifth article, but this article is not a part of this thesis.

1. Senthamizh Pavai, V., Arlt, R., Dasi-Espuig, M., Krivova, N.A., Solanki, S.K.: 2015, Sunspot areas and tilt angles for solar cycles 7–10. *Astron. Astrophys.* 584, A73 [see Chpt. 2].
2. Senthamizh Pavai, V., Arlt, R., Diercke, A., Denker, C., Vaquero, J.M.: 2016, Sunspot group tilt angle measurements from historical observations. *Adv. Space Res.* 58, 1468 [see Chpt. 3].
3. Arlt, R., Senthamizh Pavai, V., Schmiel, C., Spada, F.: 2016, Sunspot positions, areas, and group tilt angles for 1611–1631 from observations by Christoph Scheiner. *Astron. Astrophys.* 595, A104 [see Chpt. 4].
4. Leussu, R., Usoskin, I. G., Senthamizh Pavai, V., Diercke, A., Arlt, R., Denker, C., Mursula, K.: 2017, Wings of the butterfly: Sunspot groups for 1826–2015. *Astron. Astrophys.* 599, A131 [see Chpt. 5].
5. Denker, C., Heibel, C., Rendtel, J., Arlt, K., Balthasar, J.H., Diercke, A., González Manrique, S.J., Hofmann, A., Kuckein, C., Önel, H., Senthamizh Pavai, V., Staude, J., Verma, M.: 2016, Solar physics at the Einstein Tower. *Astron. Nachr.* 337, 1105

For the first, second, and third article, I worked on the data sets, which were extracted from historical sunspot drawings. My contributions comprised measurements of sunspots, defining reliable sunspot groups, and developing computer codes for calibrating the areas of sunspots as well as of sunspot group tilt angles in these sources. I generated the databases that are published along with the papers in the astronomical data centre CDS. I also wrote large parts of papers one and two, and some sections of paper three. I produced nearly all plots in those papers. For the fourth article, I contributed two data sets and participated in the discussion of the content of the article.

Zusammenfassung

Die Sonnenaktivität und ihre Folgen beeinflussen das Weltraumwetter und das Klima. Sie zeigt ein zyklisches Verhalten mit einer Periode von etwa 11 Jahren. Die Eigenschaften des Sonnenzyklus werden durch den magnetischen Dynamo bestimmt, der im Innern der Sonne Wärmeenergie über Bewegungsenergie in magnetische Energie umwandelt. Unser Wissen über den Sonnenzyklus in der Vergangenheit zu verbessern ist wichtig für das Verständnis des Sonnendynamos und die Vorhersage des Weltraumwetters. Durch die Auswertung historischer Sonnenfleckenzzeichnungen können wir diese Kenntnisse erweitern. Sonnenflecken sind die dunklen Bereiche auf der Sonnenoberfläche, die mit starken Magnetfeldern verbunden sind. Sonnenflecken sind das am längsten beobachtete Phänomen der Sonnenaktivität.

Eine der umfangreichsten Beobachtungsreihen von Sonnenflecken ist die Sammlung von Samuel Heinrich Schwabe aus den Jahren 1825–1867. Die in den Zeichnungen eingetragenen Sonnenflecken sind jedoch nicht maßstäblich. In der vorliegenden Arbeit wurde ein Verfahren entwickelt, mit dem die Fleckendaten des 19. Jahrhunderts unter der Annahme rekonstruiert werden können, dass deren Größnverteilung identisch zu der heutigen ist. Insgesamt konnten wir Positionen und Flächen von etwa 130 000 Sonnenflecken aus Schwabes Archiv bestimmen. Die Jahresmittel der Flächen korrelieren gut mit der so genannten Sonnenfleckenzahl, einer Größe, die aus der Anzahl der Fleckengruppen und der Gesamtzahl der Flecken konstruiert wird und üblicherweise als Standardmaß für die Sonnenaktivität verwendet wird. Fleckengruppen sind zumeist bipolar mit einer magnetisch positiven und einer magnetisch negativen Teilgruppe. Der Neigungswinkel dieser Gruppen gegen den Sonnenäquator wurde ebenfalls bestimmt. Ihr Mittelwert von $5.85^\circ \pm 0.25^\circ$ stimmt gut mit Werten aus dem 20. Jahrhundert überein.

Zusätzlich wurden Digitalisierte Beobachtungen von Christoph Scheiner aus dem 17. Jahrhundert analysiert, um Informationen über die Zeit vor dem Maunder-Minimum, einer Periode äußerst geringer Sonnenaktivität, zu erlangen. Bei den frühesten Beobachtungen gibt es keinen Hinweis auf die Ausrichtung des Sonnenbildes. Durch die Nutzung der Sonnenrotation über zwei oder mehr Tage können wir jedoch die Ausrichtungen fixieren. Insgesamt wurden 8167 Sonnenflecken vermessen. Darüberhinaus wurden auch 697 Neigungswinkel von bipolaren Gruppen aus den Jahren 1618–1631 berechnet. Der durchschnittliche Neigungswinkel von fast 4° unterscheidet sich nicht signifikant von den Werten im 20. Jahrhundert.

Die Neigungswinkel der Sonnenfleckengruppen scheinen Einfluss auf den Dynamo zu haben. Es wurden in der vorliegenden Arbeit noch weitere Neigungen bipolarer Sonnenfleckengruppen aus verschiedenen historischen Beobachtungsreihen aus 270 Jahren bestimmt, insgesamt von den Beobachtern Scheiner, Hevelius, Staudacher, Zuconi, Schwabe und Spörer. Die durchschnittlichen Neigungswinkel vor dem Maunder-Minimum unterschieden sich nicht wesentlich von modernen Werten, außer etwa 50 Jahren nach dem Maunder-Minimum, als die mittlere Neigung nahe Null war. Da die typischen Neigungswinkel vor dem Maunder-Minimum sich jedoch nicht wesentlich von modernen Werten unterscheiden, legt dies nahe, dass die ungewöhnlich niedrige Werte nicht für das Eintreten der Sonne in eine solche Minimums-Periode verantwortlich waren.

Mit den Sonnenfleckendaten von Schwabe (1826–1867) und Spörer (1866–1880) reicht das so genannte Schmetterlingsdiagramm von Sonnenfleckengruppen bis 1826 zurück. Eine kürzlich entwickelte Methode, die Nord- und Südhälften des Schmetterlingsdiagramms zu trennen, zeigte Zyklus-zu-Zyklus-Variationen in der Start-, End-, und höchsten Breite der Teilflächen. Die "Schmetterlingsflächen" der stärkeren Zyklen tendieren dazu, in höheren Breiten zu starten und eine größere Ausdehnung zu haben. Nord- und Südhemisphäre der Sonne zeigen einen neu beginnenden Zyklus zu leicht unterschiedlichen Zeiten. Der Phasenunterschied schwankt langsam mit einer Quasiperiode von 5–6 Zyklen.

Die oben erwähnten Resultate zeigen, wie hilfreich historische langzeit Analysen sind, um die Parameter des Sonnendynamos zu bestimmen und so Rückschlüsse auf die ihm zugrunde liegenden Prozesse ziehen zu können.



Chapter 1

Introduction

Sunspots have been observed by humankind from different parts of the world since very old days. There are many reports about naked-eye observations even before the invention of telescopes. Naked-eye observations of large sunspots are possible if the sunlight is attenuated by fog, a dust-storm, clouds, smoke of a fire, or during sunrise and sunset. A 3000-year-old Babylonian tablet likely contains the oldest observations of sunspots (Sayce, 1877). There are many naked-eye reports from Oriental countries like China, Korea, and Japan. Other historical naked-eye reports are from Arabic, European, Indian, and Maya people (Vaquero and Vázquez, 2009). The camera obscura was also used for sunspot observations in the 17th century (Vaquero and Vázquez, 2009, and references therein). With the invention of the telescope in the 17th century, more detailed and continuous observations of sunspots began. Numerous reports and drawings of those observations cover periods of months or years or decades, which can be used for scientific investigations. They are very useful not only in understanding our Sun but have also many other applications in studies of space and past terrestrial climate. An intense recurrent geomagnetic storm during December in 1128 AD, for example, has been deduced from historical aurorae and naked-eye observations (Willis and Stephenson, 2001).

With our ever-increasing dependence on technology, the forecast of space weather becomes important. Space weather refers to the influence of solar events on the interplanetary environment. Figure 1.1 shows possible impacts of solar activity on Earth, which explains the need to understand its effects and to improve the forecasting methods. Although less influential, minor events take place on a daily basis, while severe events occur very rarely, which affect our Earth. Different types of solar events cause different impacts on equipment, technical devices, and health in space and at high altitudes. They cause disturbance in the transmission of electric power, and affects or blocks radio transmission and satellite communication. They also affect the accuracy of the Global Positioning System (GPS) whose usage has increased in the last decade.

Geomagnetic storms, which are temporary disturbances of the Earth's magnetosphere, cause the above-mentioned effects. They are due to the interaction of solar wind shock waves and/or magnetic clouds with the Earth's magnetic field. Geomagnetic storms may be driven by a Coronal Mass Ejection (CME) or a high-speed stream (Corotating Interaction Region or CIR). The CME-driven geomagnetic storms often occur during the maximum phase of solar activity, while the CIR-driven storms occur mostly in the minimum phase of solar activity (Vaquero and Vázquez, 2009, and references therein). Geomagnetic storms also affect the corrosion rates of the pipelines, so the pipeline engineers need space weather alerts to take proactive measures (Trichtchenko and Boteler, 2002).

Solar flares, which release flashes of radiation, affect the radio communication. Solar Energetic Particles (SEPs) are energetic, charged particles, such as electrons and protons, which originate from a solar-flare site or from shock waves associated with CMEs. They can affect

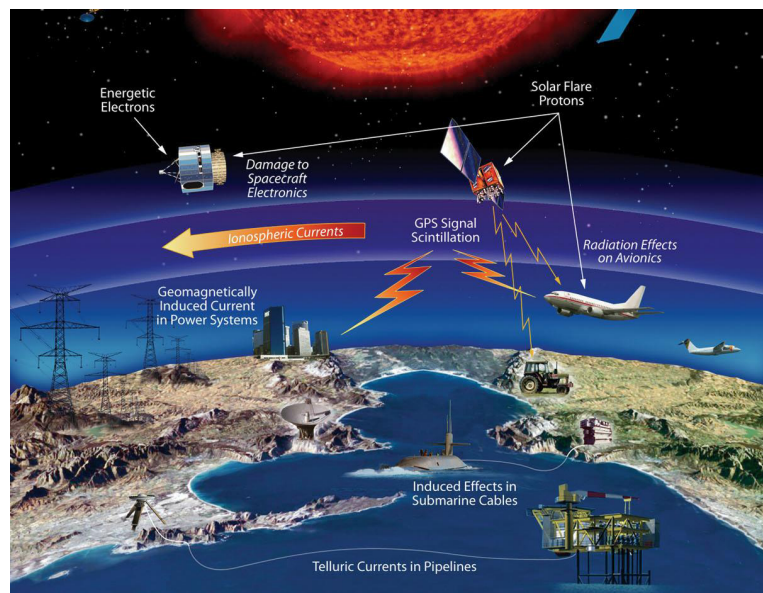


Figure 1.1: Possible impacts of solar activity on space weather and Earth¹.

satellite electronics and are potentially dangerous for astronauts in space. They also pose health hazards for airline travelers on high-altitude and polar routes. Extreme examples of such events are the disruption of the telegraph service caused by the solar storm of September 1859 and the nine-hour electric power outage at Hydro-Québec's electricity transmission system in Canada during the March 1989 geomagnetic storm (Boteler, Pirjola, and Nevanlinna, 1998, and references therein).

The solar and stellar activity play a vital role, through long-term effects over millions/billions of years, in making a planet habitable. The short-term impact of solar activity on Earth's climate has not been clearly determined, yet. The change in the total solar irradiance over the solar cycle does not vary much. However, the Maunder minimum, when a period of very low solar activity, is roughly correlated with the Little Ice Age (Eddy, 1977). Solar activity also modulates the cosmic ray flux reaching the inner solar system, which is higher during low and lower during high activity.

Space weather forecasting becomes inevitable but is a major challenge. The accuracy of the events and their impacts are still poorly known in advance since the underlying physics are not understood well, yet. The study of many more solar activity cycles may facilitate a better grasp of it. Solar activity of past centuries can be acquired from historical sunspot observations like drawings and verbal notes. The comparative study of solar activity with the terrestrial records like geomagnetic, aurorae, cosmogenic radionuclides, and climate over many centuries likely leads to a more realistic and reliable forecast.

1.1 The solar cycle

The generation and drivers of solar activity needs to be understood well before attempting to forecast space weather. Even though the solar cycle is a long-standing problem in solar physics, it still remains unsolved. Almost continuous (daily) solar observations started with the invention of telescopes in the early 1600s, but the cyclic behavior was not realized until 1844 even though Horrebow noticed the variability in 1773. The activity cycle was discovered by the German amateur astronomer Samuel Heinrich Schwabe from his solar observations covering a period of over 18 years. He found that the number of annual spotless days changes with a cycle of 10 years

¹Brian Dunbar, *Solar Storm and Space Weather – Frequently Asked Questions*, last updated: 4 August 2017, accessed 18 November 2017, www.nasa.gov

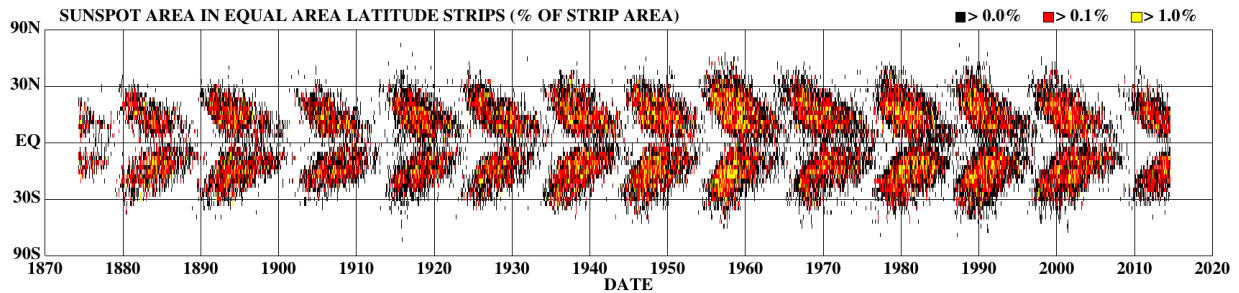


Figure 1.2: Time-latitude diagram of sunspots since the solar cycle no. 11 (Figure 9 in Hathaway, 2015).

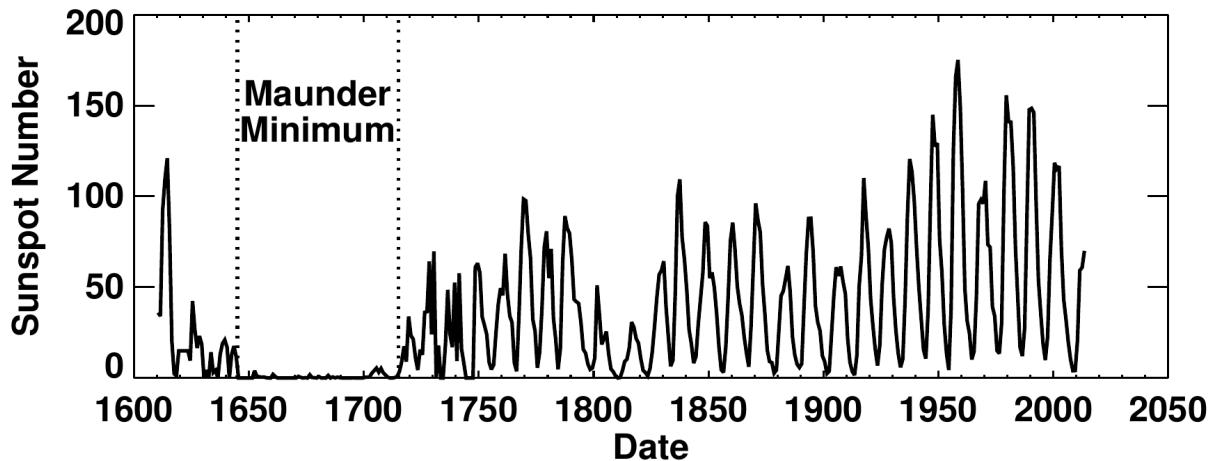


Figure 1.3: The group sunspot number record showing solar cycles with various activity levels (Figure 38 in Hathaway, 2015).

period (Schwabe, 1844). Nowadays we know that the solar activity displays roughly an 11-year cycle, but the length is not the same for all cycles, and it actually ranges from 9–14 years. The ascending phase, minimum to maximum activity, of the solar cycle is shorter than the descending phase, i.e., maximum to the next minimum.

Figure 1.2 shows that the end of one cycle overlaps with the beginning of the next cycle, but there are some cycles, for example, the cycles starting around 1911 and 2008, which are clearly separated. With sunspots, the overlapping period is 2–3 years, while it increases to 4–5 years when ephemeral regions and Ca II plages are also included. The ephemeral regions are small-scale bipolar magnetic flux elements, which have low flux density and total flux in comparison to a sunspot, and Ca II plages are brightened regions in the chromosphere associated with the magnetic field. The photospheric counterpart of plages are faculae, which are bright areas, in contrast to darker sunspots, seen in regions with or without sunspots. The ephemeral regions and small Ca II plages precede the sunspot emergence of a new solar cycle by 0.5–1.5 years, at higher latitudes than the spots, and continue near the equator for a period of nearly half a year after the end of the emergence of near-equator sunspots (Schrijver and Zwaan, 2000). This increases the overlap period. Tlatov, Vasil’eva, and Pevtsov (2010) even report that the cycle of ephemeral regions may begin at the maximum of the previous cycle.

While all solar cycles differ from each other, many of their characteristics are similar, which need to be understood to model solar activity. The activity levels of solar cycles are not homogeneous but display extreme levels of activity, i.e., variations from a very low-activity period of the Maunder minimum (Maunder, 1890; Eddy, 1976), to a moderate-activity period of the Dalton minimum, and finally to a high-activity period of the modern maximum (Solanki *et al.*, 2004), which is probably the strongest in the last 8000 years. The variability is demonstrated in Fig. 1.3. Not only the activity level varies, but also the shape, amplitude, and length of the cycles vary.

The cyclic pattern is seen in all the features mentioned below, which are called activity indices:

- **Sunspot number:** It is the count of a number of sunspots or groups, and it quantifies the activity levels of solar cycles. The proportionality between the sunspot number and the faculae/plages activity is similar to the proportionality between sunspot number and the strong magnetic activity of the Sun. Hence, it can be used to represent the full-disk magnetic activity of the Sun constituting both strong (sunspots) and weak (faculae/plages) magnetic fields (Li *et al.*, 2014). [See Sect. 1.3 for more details.]
- **Sunspot area:** This index refers to the solar surface area covered by the sunspots. It is a physical measure of solar activity given in units of millionths of the solar hemisphere (MSH). Since the area is proportional to the magnetic flux of sunspots, it is the most appropriate index to represent strong magnetic activity (Li *et al.*, 2014). [See Sect. 1.3 for more details.]
- **F10.7 index:** The full-disk integrated flux density of solar radio emission at the wavelength of 10.7 cm for a unit bandwidth is also a frequently used index in solar activity studies. It is fully objective and independent of Earth’s weather conditions (Hathaway, 2010). The bremsstrahlung radiation produced in hot coronal structures, which varies with plage and the magnetic network (weak fields), and the gyromagnetic radiation, which varies with the sunspot (strong) magnetic fields, are the sources of the F10.7 index. Hence, it is a suitable index for weak and full-disk magnetic activity of the Sun (Li *et al.*, 2014).
- **Flare index:** Flares represent the most powerful and explosive form of solar activity. The flare index Q , i.e., the mean of flare activity in a day, is a product of the flare’s relative importance I in the $H\alpha$ -range and its duration t , $Q = It$ (Kleczek, 1952; Özgüç, Ataç, and Rybák, 2003). It is roughly proportional to the total energy emitted by the flare. The X-ray flux of flares is measured in watts per square meter, and it is labeled for each decade with A, B, C, M, and X on a logarithmic scale from small to big.
- **Coronal index:** This optical index of the solar activity measures the averaged daily irradiance emitted by the coronal green line of Fe XIV $\lambda 530.3$ nm. It is correlated with solar activity, and it is useful in solar-terrestrial studies as it is modulated by sunspots, solar flares, CMEs, and coronal holes (Mavromichalaki, Petropoulos, and Zouganelis, 2002; Mavromichalaki *et al.*, 2005).
- **Solar irradiance:** This index comprises the total energy flux from the Sun per unit area at a distance of one astronomical unit (AU) from the Sun. The integrated energy of photons over all the wavelengths of the electromagnetic spectrum is the total solar irradiance. Solar activity modifies the distribution of emerging photons from different regions of the Sun and at different wavelengths. This index represents the amount of energy reaching Earth just above the atmosphere. Hence, it has its main application in solar-terrestrial relations. [See Sect. 1.3 for more details.]
- **Ca II K-index:** The weak magnetic field from plages and magnetic networks are easily observed at a wavelength of 393.37 nm, and the integrated line-core radiation comprises the Ca II K-index. It is very sensitive to the solar activities (Bertello, Pevtsov, and Pietarila, 2012) and so it can be used as proxies for the total solar magnetic flux (Ortiz and Rast, 2005) and chromospheric emission (Foukal *et al.*, 2009). The Ca II K-index from stars are used in stellar activity studies.
- **Mg II core-to-wing ratio:** This index of solar chromospheric ultraviolet emissions is based on the ratio of the Mg II h and k lines (line-core emission) with respect to the background of the solar continuum near 280 nm. This index is a very good proxy for the solar extreme ultraviolet (EUV) radiation (Viereck *et al.*, 2001).

The indices, which are more relevant to our work, are described in detail later.

1.2 Solar cycle properties

Sunspots do not emerge randomly across the solar surface but have preferred latitude bands over the course of a cycle. When the solar cycle begins, active regions appear at mid-latitudes of around 30° north and south of the equator and sometimes at higher latitudes for stronger cycles but never above 60° . However, ephemeral regions have a wider latitudinal distribution than sunspots (Harvey and Martin, 1973), or are perhaps even uniformly distributed over the solar surface (Hagenaar, Schrijver, and Title, 2003). As the cycle progresses, active regions emerge in lower latitudes and at the end of the cycle, they appear close to the equator. This equatorward migration of activity bands is called Spörer’s law (Carrington, 1858; Spörer, 1883). The time-latitude diagram of sunspots, representing Spörer’s law, was first plotted by R. C. Carrington (Carrington, 1858) but familiarized by E. Walter Maunder (Maunder, 1904). It is known as “butterfly diagram” or Maunder’s “butterfly diagram”. Figure 1.2 shows the butterfly diagram comprising sunspot areas and latitudes since solar cycle no. 11. The numbering of the solar cycles started with no. 1 for the solar minimum at 1755, and the cycle before that is numbered with 0 preceded with negative numbers.

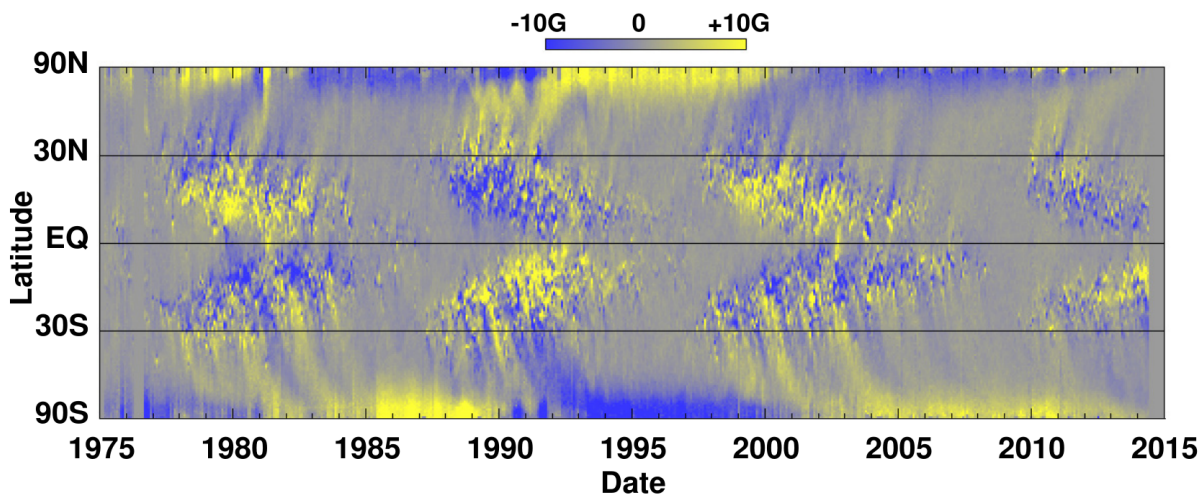


Figure 1.4: The “magnetic butterfly diagram” showing the activity belts as in Fig. 1.2 including poleward surges and polarity reversals in the photosphere (Figure 17 in Hathaway, 2015). The yellow color represents positive flux, whereas as the blue color represents negative flux.

While bipolar active regions appear around the equator, up to $\pm 60^\circ$ latitude, the magnetic flux above that latitude is predominantly single polarity as seen in Fig. 1.4, with opposite polarities at each pole, which are called polar caps (Schrijver and Zwaan, 2000). This gives the Sun’s magnetic field a dipolar moment, with the largest magnetic flux contained in the polar regions during minimum, when there are no active regions on the solar surface. After the solar maximum, in a time span of about 1–2 years, the polar caps change their polarities.

Sunspots emerge in pairs with two different polarities: the western polarity is referred to as leading/preceding (l-/p-) polarity and the eastern polarity as following (f-) polarity. Hale’s law states that the majority of leading magnetic polarities in a hemisphere is of one polarity, and that they are opposite in the northern and southern hemispheres. The switch of polarities takes place at the end of each cycle (Hale *et al.*, 1919) as can be seen in Fig. 1.4. From minima to maxima of solar cycles, the polarity of the leading spots matches that of the polar cap in the same hemisphere. The polarity reversal at the poles takes place during the cycle maximum, and it takes 22 years to return to the same polarity at the poles. This is called Hale’s magnetic cycle or as the “magnetic sun-spot” period as it was named by Hale and Nicholson (1925). There are also groups, which do not obey Hale’s law, called anti-Hale groups, constituting 8% or less as deduced from magnetogram data (Li and Ulrich, 2012; Sokoloff, Khlystova, and Abramenko, 2015).

The polarities of a group are located at different latitudes, and so the group is tilted towards the equator in the direction of rotation as shown in Fig. 1.5. The angle between the axis joining the group polarities and the E-W direction is called the “tilt angle”. The tilt angle is positive if the leading polarity lies closer to the equator than the following polarity and is of “Hale” polarity. However, there are different ways to calculate tilt angles (see Li and Ulrich, 2012; McClintock, Norton, and Li, 2014, for details). The average tilt angle of a group increases as the latitude of the group increases, which was observed by A. H. Joy, and it is commonly referred to as Joy’s law (Hale *et al.*, 1919). The tilt of the flux tube arises likely due to the kink instability and/or Coriolis force (van Driel-Gesztelyi and Green, 2015). The change in the tilt orientation, possibly by sub-surface flow vortices, was observed in an active region by González Hernández *et al.* (2013). The scatter in the tilt angles increases with a decrease in the areas of active regions, while ephemeral regions exhibit completely random tilt angles (Hagenaar, Schrijver, and Title, 2003). The mean tilt angle differs from cycle to cycle and varies from 4.6° to 6.6° for cycles 16–23 (Wang *et al.*, 2015). In addition, the tilt angle is a very important parameter in flux-transport dynamos (Babcock-Leighton dynamos, see e.g. Charbonneau, 2010, Sect. 4.8).

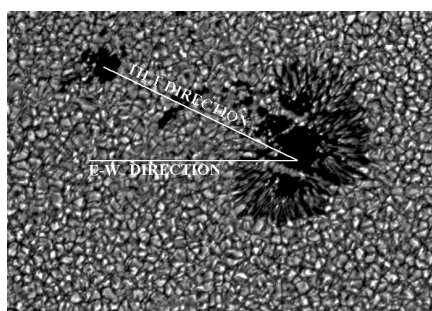


Figure 1.5: Definition of the tilt angle as the angle between “tilt” and “E–W” direction².

Active regions preferentially emerge near an existing active region, and such regions are referred to as active nests or active longitudes. Active nests have a lifetime up to about 6 months (Brouwer and Zwaan, 1990) and comprise more than 50% (Harvey and Zwaan, 1993) of active regions. The activity, in terms of the number of emerging active regions, shows an imbalance with respect to the solar hemispheres with periods from months to years which is known as North–South (N–S) asymmetry. From sunspot observations, this asymmetry has been found to be strong during the Maunder and Dalton minima. At the end of the Maunder minimum, sunspots were mostly observed in the southern hemisphere (Ribes and Nesme-Ribes, 1993). However, sunspots dominated in the northern hemisphere during the beginning of the Dalton minimum (Arlt, 2009; Usoskin *et al.*, 2009).

The positions of sunspots trace the differential rotation (defined in Sect. 1.7) and meridional circulation (defined in Sect. 1.7), so they can help us in constraining the surface flows. The sunspot positions also constrain the properties of dynamo model, as they indicate the migration of the strongest magnetic fields, a certain north–south asymmetry, and possibly active longitudes. They also help us in constraining the process of flux emergence, which is related to the strength of the dynamo.

Figure 1.4 shows the “magnetic butterfly diagram” illustrating the large-scale magnetic field evolution on the solar surface via the flux transport process. It is constructed from the longitudinally averaged radial magnetic fields obtained from magnetographs. Figures 1.2 and 1.4 allow us to deduce Spörer’s law, Hale’s polarity law, transport of higher latitude magnetic flux to the poles, and the polar reversals during solar maximum.

Some other relations, between different cycle characteristics, have also been observed and discussed. The cycle amplitude is anti-correlated with the length of the ascending phase of the cycle, which is known as Waldmeier effect (Waldmeier, 1935, 1939). However, not only

²Obtained from http://solarscience.msfc.nasa.gov/images/joys_law.jpg

the anti-correlation values differ with the type of data considered but also the effect is not even seen in sunspot area data (Hathaway, 2015, and references therein). The cycle amplitude is anti-correlated with the previous cycle, known as the Amplitude-Period effect (Chernosky, 1954; Wilson, Hathaway, and Reichmann, 1998), and is correlated with the activity level at the previous minimum and with the descending time of previous solar cycles called as the Amplitude-Minimum effect (Wilson, Hathaway, and Reichmann, 1998) and the Amplitude-Descending Time Effect (Du and Du, 2006), respectively. The correlation of all the effects varies with the type of sunspot number data series (Vaquero and Vázquez, 2009; Pérez Aparicio, Vaquero, and Cruz Gallego, 2012). The odd-numbered solar cycles are larger than their even-numbered precursors, which is referred to as the Even-Odd effect or GnevyshevOhl Rule (Gnevyshev and Ohl, 1948). This effect is seen in all solar cycle pairs, except for two or three cycle pairs depending on the data type (Hathaway, 2015).

Studying group properties of cycles with different activity levels will help to obtain improved empirical relations between average properties of sunspot groups and the strength of the solar cycle (Jiang *et al.*, 2011a). Since the variability of the solar cycle is likely to be a property of the underlying processes (dynamo, spot formation), studying as many solar cycles as possible will lead to a better understanding of the Sun and its dynamo.

1.3 Indices of solar activity

Various indices, as introduced above, are used to represent solar activity. The indices are broadly divided into two categories as direct and indirect indices of which some are physical and some are synthetic. Detailed information about all indices can be found in Usoskin (2017). A few of the indices, which are related to the current work are explained in detail below.

The direct indices are based on measurements made on direct solar activity phenomena in or near the solar photosphere, such as sunspot area and sunspot number. Indirect indices, such as a change in the cosmic ray flux intensity in the heliosphere and a change in geomagnetism, are observed outside the Sun, and their variability is (partly) associated with the variability of solar activity. Physical indices are directly measured quantities of solar activity such as sunspot area, while synthetic indices are calculated from observed phenomena such as sunspot number. The most frequently used direct indices to represent the long-term solar activity are sunspot number, sunspot area, and radio flux at 10.7 cm.

1.3.1 Sunspot number

The Zürich or Wolf Sunspot Number (WSN) was initiated in 1849 by Rudolf Wolf at the Zurich Observatory. It is a synthetic index, and it has no physical meaning. It is denoted as R_z and defined as

$$R_z = k(10g + n) , \quad (1.1)$$

where g is the number of sunspot groups, n is the total number of individual sunspots, and k is a correction factor to correct for differences in observational techniques and instruments used by different observers. The value of R_z is calculated for each day using only one reliable “primary” observer. Even though the method of a single primary observer yields a homogeneous time series, the possible errors by the observer cannot be estimated. For no sunspot observations, interpolations of available and proxy data were carried out, so that the WSN series is a mixture of sunspot observations and calculated values from interpolations and proxies. Hence, it has to be taken with caution for the period of 1749–1848, and it is hardly reliable before 1749 (Usoskin, 2017, and references therein). The production of the WSN series in Zurich was stopped in 1982, and since then the daily International Sunspot Number (ISN) R_i is calculated at the World Data Center – Sunspot Index and Long-term Solar Observations (WDC-SILSO) in Belgium (Clette

et al., 2007). The WDC-SILSO produces, preserves, and disseminates the ISN. The value R_i is calculated using the same Eq. (1.1) but with a weighted average of more than 20 observers.

Hoyt and Schatten (1998) re-examined the sunspot data, collected untapped data, and invented a new index called the Group Sunspot Number (GSN). GSN also uses data from many observers, in contrast to the single observer data in WSN, and it is defined as

$$R_G = \frac{12.08}{N} \sum_{i=1}^N k_i G_i, \quad (1.2)$$

where N is the number of observers, k_i is the i -th observer's correction factor, G_i is the number of sunspot groups observed by observer i , and 12.08 is a normalization factor between R_z and R_G obtained over the period of 1874–1976. Since GSN is independent of the number of individual spots detected by the observer in a given group, it is more robust and could be extended back to 1610, and so it is 140 years longer than the WSN series. While GSN and WSN are nearly identical since the 1870s, GSN is more reliable and homogeneous than the WSN before 1849 (Usoskin *et al.*, 2015; Vaquero *et al.*, 2016, and references therein).

The mismatch between sunspot number and group sunspot number led to the identification of many flaws, corrections, and revised versions of both series (Clette *et al.*, 2014; Clette and Lefèvre, 2016; Svalgaard and Schatten, 2016; Usoskin *et al.*, 2016a). A good agreement with the group sunspot number, for the periods before 1885 and around 1945, has been obtained while using the new version data. The main inference from the revised data is the probable absence of a predominant rise of activity in the 20th century – the Modern Grand Maximum (Clette and Lefèvre, 2015). Reconstructions of group sunspot number series have been attempted and the Modern Grand maximum is seen in some series (Usoskin *et al.*, 2016a; Willamo, Usoskin, and Kovaltsov, 2017) but not in others (Svalgaard and Schatten, 2016). The comparisons of reconstructed series with indirect proxies are not always conclusive (Usoskin, 2017).

Apart from the above two sunspot numbers, other sunspot numbers exist. They are the Boulder Sunspot Number and the American Relative Sunspot Number (ARSN). The Boulder Sunspot Number is produced by the U.S. Air Force (USAF) and the National Oceanic and Atmospheric Administration (NOAA) using sunspot drawings of Solar Optical Observing Network (SOON) sites since 1977. It is calculated using the Eq. (1.1) with $k = 1.0$ as in the ISN. The ARSN is provided by the American Association of Variable Star Observers (AAVSO) since 1944 (Taylor, 1985). This series sometimes deviates from the ISN, but it is usually aligned with the later, and it is on average about 3% lower (Hathaway, 2015).

1.3.2 Sunspot area

In contrast to sunspot numbers, areas of sunspots are physical quantities, and are an important measurement in long term studies of the Sun and dynamo models. Sunspot area records are not continuous before 1906 even though group sunspot areas are available since May 1874 from the photoheliographic observations of the Royal Greenwich Observatory (RGO). However, many long and short periods of sunspot drawings and reports exist since 1610.

Sunspot demarcate areas are the regions, where concentrated magnetic flux crosses the photosphere suppressing the convection cells (Biermann, 1941) and therefore appear as dark in continuum images of the photosphere. They are a straightforward proxy to represent the strong magnetic activity (Li *et al.*, 2014), since there is a close correlation between sunspot area and total magnetic flux, which shows that they have the same properties and distribution (Schrijver and Harvey, 1994). The lifetime of sunspots is proportional to their area and also depends on the phase of the solar cycle (van Driel-Gesztelyi and Green, 2015, and references therein).

Probing the distribution of sunspot areas and their magnetic flux likely tells us about the physical processes operating within the Sun. Bogdan *et al.* (1988) determined the umbral area

distribution using Mt. Wilson white-light data, and found it to be log-normally distributed suggesting fragmentation of magnetic flux in the convection zone. They also determined that the distribution is independent of the phase of the solar cycle. There are additional reports about the distribution being log-normal (Bogdan *et al.*, 1988; Schad and Penn, 2010), power-law (Zharkov, Zharkova, and Ipson, 2005), and power-law for the small areas and log-normal for the larger areas (Jiang *et al.*, 2011a). Muñoz-Jaramillo *et al.* (2015) carried out a statistical test to find the best fitting distributions for sunspots, sunspot groups, and bipolar magnetic regions. They reported that sunspot group areas (umbrae+penumbrae) and sunspot umbral areas are best fitted by Weibull distributions, whereas whole sunspot areas (umbrae+penumbrae) and areas of bipolar magnetic regions are fitted best by log-normal distributions. They also reported that larger structures are better fitted by log-normal, while the Weibull distribution is suitable for data with an increased number of small structures. Since different data sets seem to represent different parts of a composite flux-area distribution, they conclude that the data sets can be related by an appropriate proportionality constant.

1.3.3 Solar irradiance

The Total Solar Irradiance (TSI) is the amount of solar radiative power per unit area incident on the Earth's upper atmosphere. The variances in irradiance at all wavelengths rely on the changes in the amount, amplitude, and distribution of magnetic activity driven by the interior dynamo. The magnetic activity changes the temperature and density of the solar surface; hence, the energy distribution of the photons emerging from that region varies and is modulated by the solar activity. Detailed information on features causing variation at different wavelengths and on multiple time-scales are given by Schrijver and Siscoe (2010). The integral of all emissions emanating from all features on the visible hemisphere is the total solar irradiance. The passage of each sunspot group decreases the TSI, which can be seen as many downward spikes, however, the TSI is enhanced during maxima, even in the presence of many groups, mainly with the emissions from frequent small, bright faculae/plages (Haigh *et al.*, 2005). Hence, it is a mutual competition between dark sunspots and bright faculae.

The link between solar irradiance and Earth's climate was first proposed by William Herschel (Herschel, 1801). Solar cycle variability is seen in TSI and variations on the time-scales of $10\text{--}10^3$ years are important for Earth's climate. The TSI comprises predominantly visible and infrared radiation with small amounts of UV, X-rays, microwaves, and radio waves. Particularly, the near-UV and extreme UV bands, which exhibit larger amplitude of variations than total irradiance, are important for climate studies and space weather (Haigh, 1994; Pap *et al.*, 1999; Schrijver and Siscoe, 2010). However, the effects of solar irradiance variability on the climate are not yet clearly understood (Solanki and Krivova, 2003; Wang, Lean, and Sheeley, 2005; Gray *et al.*, 2010).

Accurate and precise measurements of TSI are possible only from space since small changes in atmospheric properties, such as ionization of the atmosphere by the cosmic ray flux (Usoskin and Kovaltsov, 2006), the global terrestrial current system (Tinsley and Zhou, 2006), cloud cover, moisture content, and anthropogenic effects, can affect it even without an actual change in solar irradiance. Space measurements of TSI are available from 1978, but the measurements from various data sources show variabilities because of various reasons (e.g. Lean *et al.*, 2003; Fröhlich, 2016). It also need instruments with high absolute precision over long time scales.

The open magnetic field lines carried along with the solar wind into interplanetary space constitute the open flux. The solar irradiance is correlated with the open flux (Lockwood and Stamper, 1999; Lockwood, 2002), but the physical mechanism behind the correlation is not understood yet (Lockwood, 2002). The similarities between these two suggest that they may be modulated by the same magnetic features in the photosphere even though there is no direct physical link between them (Lockwood, 2002).

The solar irradiance before 1978 can be reconstructed from the reconstructed open flux as they are correlated. With the availability of records of sunspot positions and areas, the open flux can be simulated (Wang, Lean, and Sheeley, 2005). Jiang *et al.* (2011a) invented a statistical procedure to calculate the distribution of magnetic flux from just the sunspot numbers so that the open flux, and hence the total irradiance can be reconstructed even for the period with just the sunspot numbers. However, the relation between the sunspot number and the solar irradiance is not linear. The dark sunspots and bright faculae are the principal contributors to TSI, yet discrepancy exist between modeled (with sunspots and faculae) and observed TSI (e.g. Steinhilber, 2010). Reconstructing the solar irradiances with a simple scaling of sunspot number has the disadvantage of returning to the same value during every cycle minimum (Schatten and Orosz, 1990). The peaks of sunspot numbers decrease from cycle 21 to 24, but the peaks of the TSI were not varying largely until solar cycle 23 and then it drops (Schrijver and Siscoe, 2010; Kopp, 2016). Hence, reconstruction of solar irradiance is cumbersome. For earlier periods without sunspot number records, i.e., before 1600, the reconstruction is only possible using cosmogenic isotopes, e.g., ^{14}C and ^{10}Be , which show that the solar activities vary above a background component, which is not seen in sunspot numbers. The varying background is due to variations in the open flux, which modulates the cosmic rays and hence the cosmogenic isotopes (Wang, Lean, and Sheeley, 2005). The open flux constitutes only a few percent of the surface flux, so the dominant variation in the irradiance is caused by sunspots and faculae which constitute “closed flux”.

The variation of solar irradiance caused by different features needs to be studied to make more reliable forecasts. Forecasts of solar irradiance have a wide range of applications from space weather (Henney *et al.*, 2015, and references therein), which changes the ionization of upper atmosphere, and consequently affects the communication and navigation signals, to climate change. In any case, they are very challenging. They need to be approached by numerical models, statistical tools, and a physical understanding of the different features emitting in different wavelength bands (Hathaway, 2009). Understanding the causes of solar irradiance variability are also beneficial in reducing the “noise” related to stellar activity, and, therefore enhances the ability to detect exoplanets (Dumusque *et al.*, 2015).

1.4 Indirect solar indices

Solar activity and related phenomena cause a variability in some properties of the terrestrial environment like the Earth’s surface magnetic field and the heliospheric magnetic field which modulates cosmic rays. These are the indirect proxies of solar activity and hence indirect indices are very helpful in reconstructing solar activity of the pre-telescopic era and to validate the reconstructed solar activity from other methods.

1.4.1 Geomagnetic activity

The geomagnetic field exhibits a dipolar configuration, which varies over time because of its internal changes and externally by solar events. The regular and irregular variations in the geomagnetic field are due to the daily variation in the solar radiation and due to the solar wind and its consequent changes in the magnetosphere and ionosphere, respectively. The solar wind compresses and flattens the outer boundaries of the magnetosphere on the dayside, and stretches them on the night side forming a magnetotail. The magnetosphere is not stable but fluctuates depending on the solar wind pressure which causes the geomagnetic variations. A semi-annual variation of geomagnetic activity with stronger and more frequent storms in spring/fall than in summer/winter is also seen.

The positive correlation of geomagnetic disturbances with the 11-year solar cycle was discovered independently by Sabine (1852), Wolf (1852), and Gautier (1852). The long-term time-series

of geomagnetic declination and inclination measurements made in European cities are available since the 16th century (Malin and Bullard, 1981; Cafarella, De Santis, and Meloni, 1992; Baraclough, 1994; Alexandrescu, Courtillot, and Le Mouél, 1996). From the second half of the 19th century, geomagnetic variations are recorded using magnetographs as geomagnetic indices. Geomagnetic indices are related to irregular variations in the geomagnetic field excluding the smoothly varying regular daily variation.

There are about 30 geomagnetic indices containing series of discrete numbers denoting the local or global magnetic field variations. They can serve as proxies for the long-term evolution of the solar activity. The most commonly used index is Bartels' K-index, but it is available only since 1938. It is derived from the maximum fluctuations of horizontal components of Earth's magnetic field, caused by solar wind particles, observed on a magnetometer in a 3-hour interval (Bartels, Heck, and Johnston, 1939). The aa-index is a 3-hourly geomagnetic activity index calculated from the two antipodal magnetic observatories in England and Australia (Mayaud, 1973), and it is available since 1868. It is widely used as a proxy for solar activity in solar-terrestrial studies because of its homogeneous long duration availability, and it also belongs to the K-index family (Rangarajan, 1989). Nevanlinna and Kataja (1993) calculated the Helsinki Ak-index, similar to the aa-index, from the magnetic declination D . The correlation of monthly means of the aa- and Ak-indices is 0.96 for the overlapping period, and thus the combined data would be the longest series. A summary of all other indices are available in Vaquero and Vázquez (2009).

1.4.2 Aurorae

Auroral observations are another proxy for solar activity related to geomagnetic variations. Aurorae are formed when the solar wind particles penetrate the Earth's magnetic field, collide with atoms and molecules in the atmosphere, and emit photons at visible wavelength. They are abundant at higher latitudes of Earth, but they are scarce at low latitudes, as only strong geomagnetic storms can produce them. Some low-latitude aurorae have been observed during weak-to-moderate geomagnetic activity which are called as "sporadic aurorae" (Vaquero and Vázquez, 2009, and references therein). As aurorae are the most spectacular phenomena, they have fascinated many civilizations and have deep roots in mythology. The Babylonian astronomical text on a sun-dried clay tablet might be the oldest recorded aurora according to Stephenson, Willis, and Hallinan (2004). There are many historical reports about the aurorae from Asia, Europe, America, and Arab countries, which contain many interesting information on past solar activity. From the well-documented auroral observations in the period of 223–91 BCE, Stothers (1979) found that the solar activity was similar to the present with a mean period of 11.5 years and a secondary cycle of 80–100 years. The first indication of a connection between sunspots and aurorae is presented by Mairan (1754). A strong correlation exists between the variations of sunspot numbers and the frequency and latitudinal extent of aurora occurrences (Usoskin, 2017). A homogeneous data set of aurorae is difficult to assemble as observations are not systematic in early times (before the 18th century). Owing to the migration of the geomagnetic axis, the geomagnetic latitude changes over centuries which also affects the observation of aurorae (Vaquero and Vázquez, 2009, and references therein). The probability of seeing the aurora also depends on its duration, brightness, weather (sky overcast, heat lightnings), etc.

1.4.3 Cosmogenic radionuclides

The intensity of Galactic Cosmic Ray (GCR) flux is modulated by the magnetic activity of Sun on the way through the heliosphere, and it is inversely related to the solar activity. The high-energy, high-speed GCR collides with the molecules in the atmosphere and forms an atmospheric cascade in which cosmogenic isotopes are the by-product. The rate of production of cosmogenic radionuclides in the Earth's atmosphere depends on the incoming GCR, and then they are stored in "natural archives" such as trees, polar ice, marine sediments, etc. As a consequence, it

serves as an inverse proxy for solar activity. But it can only give an indication of the long-term trend and not the accurate details of each cycle. The production and transport of cosmogenic radionuclides also gets affected by the changes in the geomagnetic field and climate, which needs to be considered while using these data (Usoskin, 2017).

The most commonly used isotopes in the past solar activity studies are ^{14}C and ^{10}Be stored in tree rings and ice cores, respectively. The cosmogenic radionuclides are the longest available proxies for solar activity covering the whole Holocene period (since 9,700 BCE). They reveal many interesting results like the number of grand minima and grand maxima, and the types of periodicities seen in the activity data – for example, the 210-year de Vries/Suess cycle and the 2000–2400 year Hallstatt cycle (Usoskin, 2017). Inceoglu *et al.* (2015) suggests that the Sun experienced 32 grand minima and 21 grand maxima during 6600 BCE–1650 CE, while Usoskin, Solanki, and Kovaltsov (2007) and Usoskin *et al.* (2016b) claim 25 grand minima and 23 grand maxima since 9500 BCE. The reconstructed proxy data shows that the grand minima and grand maxima have happened irregularly with clustering near minima and maxima of the Hallstatt cycle, respectively (Usoskin *et al.*, 2016b). The reconstructed proxy data suggests two kinds of grand minima: 50–80 years short minima, referred to as Maunder-type, and longer minima which are referred to as Spörer-like minima (Stuiver and Braziunas, 1989; Stuiver *et al.*, 1991); whereas about 75% of grand minima are not longer than 50 years (Barnard *et al.*, 2011). Hence, during the Holocene, the Sun has spent 70% of the time in normal state, 15–20% in grand minima, and 10–15% in grand maxima (Usoskin, 2017).

1.5 Reconstruction of solar activity

As mentioned above, solar activity can be reconstructed either from direct or indirect data of solar variability. The first reconstruction of solar activity was carried out by Rudolf Wolf. He extended the period for which the sunspot number was available by over a century using sunspot observations of Staudacher from 1749 to 1787, Flaugergues from 1788 to 1825, and Schwabe from 1826 to 1847. At the end of the 20th century, researchers found some problems with the Wolf sunspot number like misplacement and underestimation of the maximum amplitude of solar cycle 7 (Wilson, 1998) and possibly one lost solar cycle during the beginning of Dalton minimum (Usoskin, Mursula, and Kovaltsov, 2001). This indicates the need for extreme caution when dealing with sunspot records, and led to the construction of a new sunspot number by Hoyt and Schatten (1998). These authors discovered many observations that were not used by Wolf, so that the number of observations increased from 81 521 to 147 462 which included observations from 117 observers. This new reconstruction also extended the period of the sunspot number series into the past to 1610 even though with some gaps and some wide interpretation of the sources. Some problems and errors still exist in this reconstructed series which have to be considered (Vaquero and Vázquez, 2009).

Only the sunspot numbers were retrieved from the observations in those reconstructions, and with those we only have a single disk-integrated activity curve. With the sunspot positions and areas, more information about the real properties of the solar cycle like tilt angles of sunspot groups, migration (butterfly diagram) or proper motion of sunspots, differential rotation, time profiles of rising and decaying phases, etc. can be studied. Since each solar cycle is unique, it becomes important to study as many cycles as possible either from observational or reconstructed data. The continuous record of sunspots observations with positions and areas are available only since the 20th century and the record of sunspot groups since 1874. It can be extended in the past till the beginning of the telescopic era through discovering, digitizing, and extracting of data from available historical sunspot drawings. Such work has been carried out by Casas, Vaquero, and Vazquez (2006), Arlt (2009), Cristo, Vaquero, and Sánchez-Bajo (2011), Arlt *et al.* (2013), and Diercke, Arlt, and Denker (2015). With sunspot positions and areas, the solar surface magnetic field can be simulated for the past centuries.

The variability of the Solar Magnetic Field (SMF), over time and latitude, determined by the solar cycle properties influences the coronal field and the open flux. The open flux, which is the magnetic flux dragged out into the heliosphere, regulates the characteristics of solar wind like temperature, flow pressure and speed, density of wind particles, etc. The solar wind governs the intensity and orientation of magnetic field reaching Earth’s magnetosphere which causes the geomagnetic perturbations. The correlations between the Interplanetary Magnetic Field (IMF), also referred to as the heliospheric magnetic field, and the SMF at different latitudes show that the IMF follows the variability of the photospheric magnetic field with an optimal delay of about four days (Gavryuseva, 2006). The planetary geomagnetic activity index behaves in a similar way to the solar wind characteristics (Gavryuseva, 2006).

Hence, the solar surface magnetic field, open flux, and solar irradiance can be simulated into the past with the reconstructed solar activity data, which have many applications in terrestrial climate and geomagnetic studies. Even though there are empirical ways to reconstruct them, based on the known solar cycle properties, it is beneficial to use as much observational data as possible and to include physical processes into their reconstruction as each cycle is unique.

1.6 Solar dynamo

The activity features on the surface of the Sun are driven by the magnetic field, but their origin is not clearly known, yet. A primordial magnetic field would have vanished within a few million years because of Ohmic decay, i.e., without some process to sustain the field. Hence, it is widely assumed that a magnetic dynamo taking place within the Sun is responsible for the long-lasting persistence of the magnetic field. Joseph Larmor (1920) proposed the idea of dynamo fields as a solution but it was questioned by Cowling’s “Anti-Dynamo Theorem” (Cowling, 1933). The first widely accepted theoretical explanation for a dynamo process for the large-scale solar magnetic field was put forward by Parker (1955). He introduced a term in the induction equation for the large-scale field, which was then rigorously derived by Steenbeck, Krause, and Rädler (1966) in the theory of the α -effect.

The dynamo theory explains how a rotating, convective, and electrically conducting fluid can maintain a magnetic field through inductive effects over astronomical time-scales against Ohmic decay. The differential rotation in the convection zone is able to generate toroidal fields from poloidal ones (Ω -effect), but the reverse generation of poloidal fields is likely the result of one of the following effects: a net-effect of the induction by convective motions under the influence of rotation and stratification (α -effect) or the rise of magnetic flux bundles from the toroidal field into poloidal loops, typically associated with active regions (Babcock, 1961; Leighton, 1964).

The first type of dynamo is based on the average induction effect of the convective motions, giving rise to so-called mean-field equations for the magnetic field, and is – in the case of the Sun – usually termed $\alpha\Omega$ -dynamo (Rüdiger, Kitchatinov, and Hollerbach, 2013). The second type of dynamos is more empirical and employs the meridional circulation in the solar convection zone to ensure the equatorward migration of the emerging sunspot groups. The dynamo is termed Babcock-Leighton dynamo or flux-transport dynamo (Babcock, 1961; Leighton, 1964). Figure 1.6 shows a pictorial representation of the above mentioned solar dynamo models.

1.6.1 Babcock-Leighton solar dynamo

The Babcock-Leighton dynamo is based on observations and ideas by H. W. Babcock (1961) and R. B. Leighton (1964). From series of magnetographic observations of Sun, beginning in 1952, H. W. Babcock investigated the nature of Bipolar Magnetic Regions (BMR), studied the 22-year solar magnetic cycle, and proposed a model, which could satisfactorily explain Maunder’s “butterfly diagram” and Hale’s law. Later Leighton proposed a mechanism for the spreading and migration of magnetic regions, which causes the reversal of the polar field.

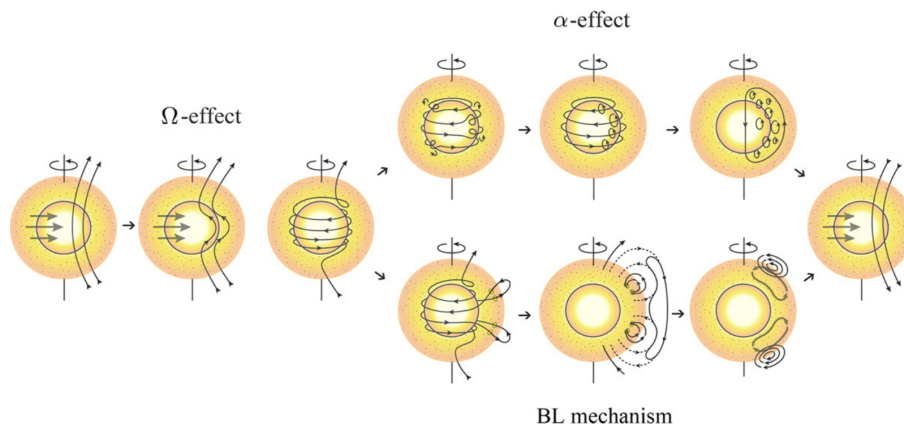


Figure 1.6: Pictorial illustration of two type of solar dynamo models. The Ω - and α - effects depict the process of generating toroidal from poloidal field and the regeneration of poloidal field, respectively. The process of generating toroidal is same in both models but generating of poloidal fields differs. In the α -effect case, the poloidal field is envisioned as cyclonic turbulence producing small-scale poloidal field, which on average form a new, large-scale poloidal field. In the Babcock-Leighton mechanism, the poloidal field depends on the properties of emerging flux and its evolution on the surface (Figure 1 in [Sanchez, Fournier, and Aubert, 2014](#)).

In the mid-to-late 1960s, the Babcock-Leighton dynamo model went unnoticed with the rise of mean-field electrodynamics leading to the $\alpha\Omega$ -dynamo. Early Babcock-Leighton dynamos that were noticed are [Durney \(1995\)](#) and [Choudhuri, Schüssler, and Dikpati \(1995\)](#), the latter being local but already advection-dominated. It received attention again recently when [Dasi-Espuig *et al.* \(2010\)](#) and [Cameron *et al.* \(2010\)](#) discovered the cycle-to-cycle variations in the tilt angle of sunspot groups and positive correlation of polar field at the end of a cycle with the strength of the next cycle, respectively.

In the Babcock model ([Babcock, 1961](#)) of the solar dynamo, the solar cycle process is divided into five stages.

1. In the first stage of the model, the magnetic field is dipolar. The magnetic field lines connect the polar caps by crossing the equatorial plane very far away from the corona.
2. Due to the Sun's latitudinal differential rotation, the field lines are wound up along the azimuth as they are nearly frozen into the plasma. After many solar rotations, the toroidal field is formed (Ω -effect) and with many more rotations the toroidal magnetic field is intensified. After reaching a threshold, the intensified magnetic flux tube forms loop (kinks) (as seen in Fig. 1.6), which results in the arch shape (Ω -shape) for the flux tube.
3. According to the theory by Parker ([1955](#)), magnetic in addition to gas pressure inside the flux tubes makes them (magnetically) buoyant and rise through the convective zone. While rising in the convection zone, flux tubes become twisted because of the Coriolis force and finally emerge as tilted BMRs on the surface. The threshold for the onset of the intensification is attained first at higher latitudes, which is the reason for the high-latitude emergence of BMRs at the beginning of the solar cycle. The time to reach the threshold increases with decreasing distance from the equator, and it is arguably the reason for Spörer's law. The formation of BMRs in a particular latitude band stops, when the condition for emergence is not satisfied.
4. This stage describes how BMRs evolve in the photosphere, vanish, and cause the neutralization and reversal of the poloidal field. The properties of BMRs, like position, area, and tilt, and the surface flows determine predominantly the amount of flux reaching the pole. The neutralization of the polar field and the development of the new reversed dipolar field depends on the amount of flux reaching the poles. These processes are explained in detail in Sect. 1.7. Around 1% of emerging flux appears to be enough to neutralize and reverse the existing polar fields ([Schrijver and Zwaan, 2000](#)).

5. The fifth stage is same as the first stage with reversed polarity which is then followed by (above-mentioned) subsequent stages, thus constituting the second half of the 22 year magnetic activity cycle.

Hence, the dynamo action depends intimately on the properties of sunspot groups in this particular type of dynamos.

1.7 Surface flux transport model

The processes of flux dispersal, after the emergence of flux in the photosphere, are simulated in the Surface Flux Transport Model (SFTM). The buoyant small to large flux tubes take days to weeks to emerge fully in the photosphere. The properties and path of the flux may be altered by the Coriolis force, due to solar rotation, and the convection. The properties of flux tubes upon emergence and their evolution in the presence of surface flows determine the amount of flux reaching the poles as explained (in Sect. 1.6.1) above. The flux bundles/tubes are shredded by convection close to the surface and thus appear as many tiny magnetic fragments with mixed polarities upon emergence at the surface. They subsequently coalesce and form two strong polarities as seen in bipolar sunspots groups. The distances between the polarities, called polarity separations, increase as the flux tubes emerge.

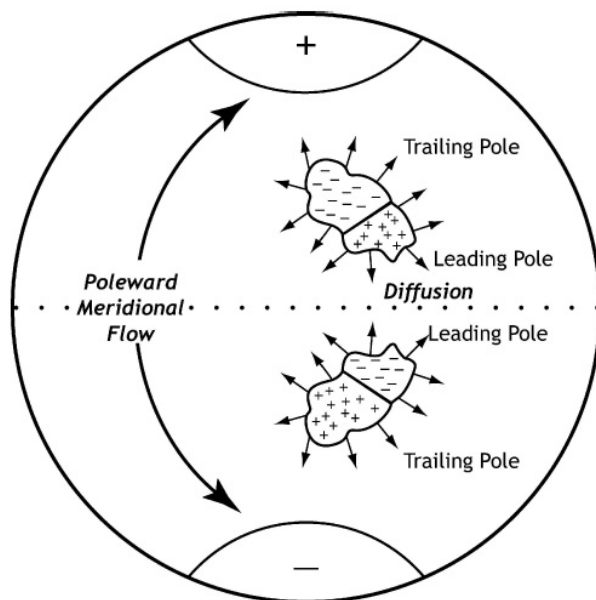


Figure 1.7: Pictorial representation of the SFTM showing the evolution of polarities of tilted BMRs. The leading polarities cross the equator and cancel, whereas the following polarities migrate to the poles assisted by a poleward meridional flow (Figure 5 in Wang, 2004).

The tilt of BMRs, due to Coriolis force and/or convection, is an important property in SFTM. The larger the tilts are, the lesser the opposite flux cancellation within a BMR or with neighboring BMRs as the opposite polarities of the latter are more separated in longitude (Baumann *et al.*, 2004). From BMRs emerging at higher latitude with higher tilt, a larger amount of flux may be transported to the poles. The amount of flux reaching the poles is determined by the flux cancellation within BMRs, with adjacent BMRs and the number of BMRs encountered on the way to the poles. Most likely, the polar fields are also related to the tilt angle (Petrie and Ettinger, 2015), and Dasi-Espuig *et al.* (2010) reported that a reasonable correlation exists between the product of the strength of a cycle and its average tilt angle and the strength of the next cycle.

The survival time of the flux in the photosphere depends on the size of the BMRs. The time in which, a new field pattern can be expected is of the order of a few days for small scales in

the quiet photosphere, while it can be up to about one year for large-scale patterns. [Schrijver and Harvey \(1994\)](#) calculated the flux replacement times, i.e., the ratio of flux present to the flux emergence rate using 978 BMRs larger than ephemeral regions, which were observed during 1975–1986. They are four and ten months for the cycle maximum and minimum, respectively. However locally, the flux removal time varies enormously, i.e., the rate is much higher in active nests than in the quiet network.

The magnetic diffusion (ohmic diffusion) is so low, of the order of only $7000 \text{ m}^2/\text{s}$, that it would take a few hundred years for a typical sunspot to decay based on its own diffusivity. The emerged BMRs diffuse mainly by random walk caused by the evolving convection, a process that is typically described by turbulent diffusion. A fraction of the leading polarity flux in each hemisphere crosses the equator and is canceled, while a fraction of the following polarity flux is transported to the poles mainly by the large-scale flows. A large part of flux is canceled by opposite polarity flux on its way to the poles. Sometimes, flux of both polarities migrates to the poles which ends up in contributing minutely to the polar field. If one of the hemispheres is more active than the other, the leading polarity flux crossing the equator from that hemisphere, with no opposite polarity flux to cancel it in another hemisphere, may get caught in the flow and is transported to that pole. In this way, the two hemispheres may interact ([Schrijver and Zwaan, 2000](#)). A pictorial representation of the surface flux transport model is shown in Fig. 1.7. The large-scale flows, which advect the flux, are mainly characterized by

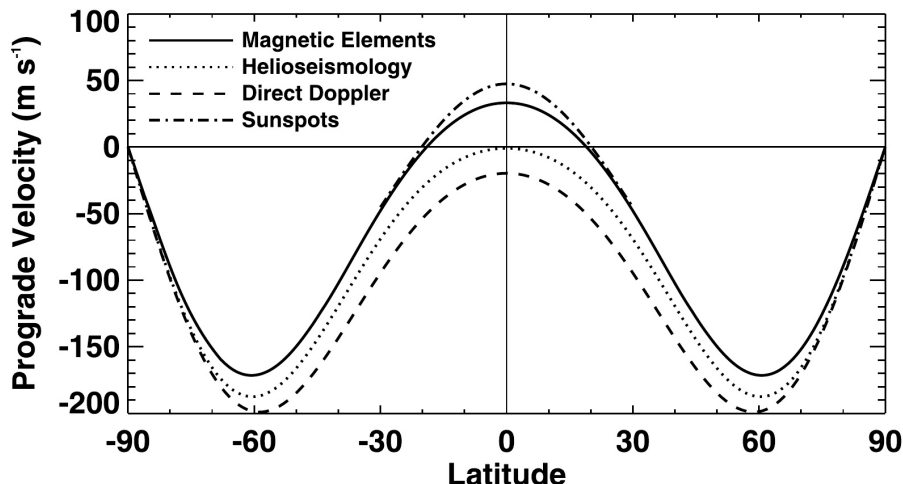


Figure 1.8: Differential rotation from different observational methods. The profile from measurements of small magnetic elements and individual sunspots were taken from [Komm, Howard, and Harvey \(1993b\)](#) and [Howard, Gilman, and Gilman \(1984\)](#), respectively. The profiles from methods of global helioseismology and direct Doppler were taken from [Schou *et al.* \(1998\)](#) and [Ulrich *et al.* \(1988\)](#), respectively (Figure 2 in [Jiang *et al.*, 2014b](#)).

1. **Differential rotation:** In 1630, Christoph Scheiner discovered that the rotational periods of sunspots vary from 25 to 28 days ([Scheiner, 1630](#)). Helioseismology yields a rotational period of Sun of 25.2 days at the equator and 38 days at the poles ([Korzennik and Eff-Darwich, 2011](#)). This dependency of the rate of rotation on latitude is termed differential rotation. The differential rotation as such is a result of the anisotropy in the Reynolds stress of rotating, stratified convection ([Rüdiger, 1989](#)).

The rotation rates for all latitudes, which cannot be derived from tracking sunspot groups, were measured by [Howard and Harvey \(1970\)](#) using magnetograms from the Mt. Wilson Observatory. The authors derived the following profile of the rotation rate $\Omega(\lambda)$:

$$\Omega(\lambda) = A + B \sin^2 \lambda + C \sin^4 \lambda \quad \text{and} \quad (1.3)$$

$$u(\lambda) = [A + B \sin^2 \lambda + C \sin^4 \lambda] R_{\odot} \cos \lambda, \quad (1.4)$$

where λ is the latitude, $u(\lambda)$ is the prograde velocity, R_{\odot} is the radius of the Sun, and A , B , and C are the fit coefficients. Profiles of the differential rotation laws from different

studies are shown in Fig. 1.8. With differential rotation, the f-polarity of a magnetic flux system, being at relatively higher latitude, is lagging behind in the east-west direction. The strongest shear between polarities occurs at the mid-latitudes. The differential rotation is likely the reason for more fragmented of f-polarities as it may twist the polarities of sunspot groups in opposite direction: enhancing the stability of p-polarity and weakening the f-polarity against fragmentation by the convection (Leighton, 1964). That variation of differential rotation with solar cycle is known as torsional oscillations (Howard and Labonte, 1980; Ulrich *et al.*, 1988; Komm, Howard, and Harvey, 1993c; Howe *et al.*, 2000). Even though the torsional oscillations are solar cycle dependent, they are very weak (~ 5 m/s) and may have minor effects on the surface flux transport.

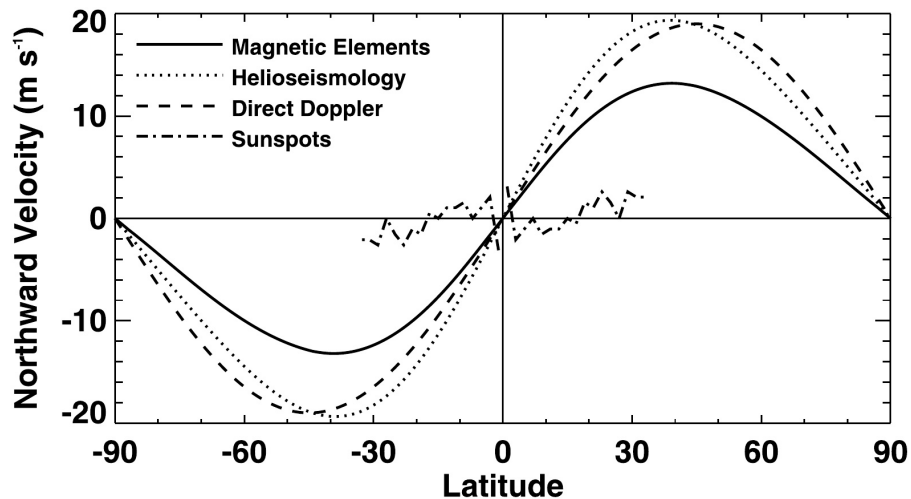


Figure 1.9: Meridional flow profile from different observational methods. The profile from measurements of small magnetic elements and recurrent sunspot groups were taken from Komm, Howard, and Harvey (1993a) and Tuominen and Kyrolainen (1982) respectively. The profiles from methods of local helioseismology and direct Doppler are from Basu and Antia (2010) and Hathaway (1996), respectively (Figure 5 in Jiang *et al.*, 2014b).

2. **Meridional flow:** The poleward flow of plasma at the solar surface and equatorward flow near the base of the convection zone is called meridional circulation. The crucial role played by meridional circulation in solar dynamo theory is studied both observationally and theoretically. The meridional flow governs the duration of the cycle and its shape (rise and fall pattern) in flux-transport dynamos. Despite being weak and very difficult to measure, it plays a vital role in transporting magnetic flux to the poles and in causing the polarity reversal during solar maximum (Dikpati and Charbonneau, 1999; Dikpati *et al.*, 2010). The surface measurements and local helioseismology studies show that meridional circulation is anti-correlated with solar activity, i.e., faster during solar minimum and slower during solar maximum at low- and mid-latitudes (Komm, Howard, and Harvey, 1993a; Komm *et al.*, 2015).

The average meridional flow is mainly directed poleward on the solar surface in each hemisphere with an amplitude of about 20 m/s (Gizon, Birch, and Spruit, 2010). The flow profiles from different studies are shown in Fig. 1.9. The flow direction is poleward till around 70° latitude (Komm *et al.*, 2013). Slightly higher values of up to 75° were observed by Hathaway and Rightmire (2010), and even a reversed flow at higher latitudes has been reported by Ulrich (2010). The latitude at which the direction of flow changes, from poleward to equatorward, varies with the solar cycle, it supposedly regulates the duration of the cycle (Dikpati *et al.*, 2010; Dikpati and Gilman, 2012). Bands of fast meridional flow at mid-latitudes were observed three years before solar cycle 24, and they are presumably precursors of magnetic solar activity (González Hernández *et al.*, 2010; Komm *et al.*, 2015). Further studies can facilitate a better understanding of solar dynamo theory, determining the variation of meridional flows with solar cycle, with depth, and with latitude.

3. **Supergranular random walk:** The differential rotation and meridional circulation are essential components of the solar dynamo, but only the large-scale convection maintains the dynamo, and consequently the convection becomes the root of solar activity. The convection produces cells of varying sizes, from granules with about 10^6 m to supergranules with about 30×10^6 m diameter, and lifetimes from about 10 min to many hours, respectively. The evolution of these convective cells (supposedly) causes a random-walk dispersal of the flux in active regions. It diffuses the magnetic flux over relatively large distances, which then either decays through the interaction of opposite polarity flux or is carried away to the poles by surface flows. Leighton (1964) needed a turbulent diffusivity $\eta_H = 770\text{--}1540 \times 10^6$ m²/s to obtain the 11-year polarity reversal without the inclusion of meridional flow. It was then reduced to $200\text{--}600 \times 10^6$ m²/s when DeVore, Boris, and Sheeley (1984) included the meridional flow, which is similar to the range of $200\text{--}400 \times 10^6$ m²/s as derived from magnetic field observations by Mosher (1977). Schrijver and Martin (1990) obtained a diffusivity of $\eta_H \simeq 250 \times 10^6$ m²/s for a quiet-Sun region around magnetic plage.

For the advection of flux toward the poles by flows, as seen in the magnetic butterfly diagram, the magnetic field has to be “frozen” into the plasma and needs a high magnetic Reynolds number ($R_m \gg 1$) according to Alfvén’s theorem. The magnetic Reynolds number is defined as

$$R_m = \frac{UL}{\eta_m} \sim \frac{\text{induction}}{\text{diffusion}} , \quad (1.5)$$

where U is a typical flow velocity on the surface, L is the length scale of the flow, and η_m is the molecular magnetic diffusivity. In the Sun, the length scale of convection cells is $L \approx 10^6$ m, and the cells have a velocity $v \approx 10^3$ m/s. The molecular magnetic diffusivity is $\eta_m \approx 10^3$ m²/s at the photosphere. The value of R_m is of the order of 10^6 , so the magnetic field is frozen into the plasma and hence the advection term (induction) dominates diffusion. The advection of the magnetic flux depends on its strength, the velocity of the flow, and anchoring of the magnetic flux. A critical quantity determining the advection is equipartition field strength

$$B_{\text{eq}} = \sqrt{4\pi\rho v} , \quad (1.6)$$

where ρ is the gas density and v is the magnitude of the velocity (convective flow). While magnetic fields with a strength below B_{eq} are always dragged by the flows, the stronger fields, which are supposedly anchored at greater depth, may even influence the flows (Jiang *et al.*, 2014b). Schüssler and Rempel (2005) claim that even the stronger flux loses the connection with the root at some point of its lifetime, and a relation between the anchoring depth and the lifetime of a sunspot is also noticed in the simulations of Rempel (2011).

The surface flux transport model is concerned with the advection of flux to the poles and the reversal of the polar field. It is the visible and directly measurable part of the solar dynamo. The predicted origin of the poleward migration of flux, predominantly of the following polarity of an active region, and the predominantly equatorward migration of the leading flux by Babcock (1961) is the meridional flow. According to Leighton (1964), a random motion of flux by supergranular flows together with Joy’s law could diffuse the leading flux towards the equator and the following flux towards the pole without the need for any other large-scale flows. Their models used only those mechanisms to reverse the magnetic polarity at the poles during the maximum phases of solar activity. Later Mosher’s (1977) result regarding the observed turbulent diffusivity rate prompted researchers to include solar-like differential rotation and meridional circulation profiles in the Babcock-Leighton dynamo model (DeVore, Boris, and Sheeley, 1984; Sheeley, Nash, and Wang, 1987; van Ballegoijen, Cartledge, and Priest, 1998). This significantly improved the simulated patterns of flux dispersal so that they became more similar to the ones observed on the Sun. The “streaks” of flux extending poleward from active regions in the magnetic butterfly diagram remained after the inclusion of the above profiles (DeRosa, 2006).

The dispersal of magnetic field by convection is commonly modeled as a Fickian diffusion process (Leighton, 1964). In Fickian diffusion, the diffusion flux \mathbf{F} is proportional to the gradient of the concentration C , i.e., $\mathbf{F} = -D\nabla C$. The diffusion coefficient D as given by Leighton (1964) is

$$D = \frac{1}{4} \frac{(\Delta l)^2}{\Delta t} = \frac{1}{4} \Delta l \Delta v, \quad (1.7)$$

where Δl , Δt , and Δv are the step size, unit time, and velocity of the random walk, respectively. Martin-Belda and Cameron (2016) reported that the dispersal of magnetic flux by convective flows on the solar surface can be represented by a diffusion approximation with a step size corresponding to the size of granules. For a supergranule, which is similar to the length scale of a BMR, some discrepancy appears but that also reduces with time (see Fig. 3 in Martin-Belda and Cameron, 2016). Hence, the description of flux dispersal by diffusion is appropriate for the mid- and long-term evolution of the magnetic field. A good agreement with the central-limit theorem – the average distribution of a number of independent variables tends toward a Gaussian distribution, even if the original variables are not normally distributed – was also evident in their simulations.

Such models successfully simulate the evolution of individual active regions over months to the global scale of the Sun over many solar cycles, even if only the radial component of the magnetic field is considered. The weakening of the subsurface fields and the subsurface reconnection, which disconnects the flux from its roots, are possible explanations (Schrijver and Title, 1999, and references therein). For a detailed review of the development of models, refer to Sheeley (2005).

The process of active region emergence in the photosphere is not simple, and so it is not included in the SFTM or flux-transport dynamos. They consider them to occur instantaneously. The emergence of magnetic bipoles needs to be fed in as an input, which is a function of the area, latitude, longitude, and time of a sunspot group/BMR. Each BMR is considered as a pair of flux concentrations around the centroid of their respective polarities with equal amounts of flux but opposite polarity. Initially, point-like bipoles were considered as developed by the U.S. Naval Research Laboratory group (Sheeley, DeVore, and Boris, 1985; DeVore, 1987; Wang, Nash, and Sheeley, 1989a), but later, finite-sized Gaussian-like polarity patches were introduced by van Ballegooijen, Cartledge, and Priest (1998). The source flux distribution is then determined by the area, latitude, longitude, and latitudinal separation, which is determined by the tilt angle. Equal amounts of flux cancel, when magnetic patches of opposite polarities are brought together by the flow, and only less than 1% of the following polarity flux is sufficient to reverse the polar field.

The evolution of the flux on the surface along with other flows/features is simulated according to the magnetohydrodynamic (MHD) induction equation. The theory of MHD is concerned with fluid dynamics of conducting fluids combined with Maxwell's equations. Faraday's and Ampere's laws in terms of Maxwell's equations are

$$\nabla \times \mathbf{E} = -\frac{\partial \mathbf{B}}{\partial t} \quad \text{and} \quad (1.8)$$

$$\nabla \times \mathbf{B} = \mu_0 \mathbf{j} + \frac{1}{c^2} \frac{\partial \mathbf{E}}{\partial t}, \quad (1.9)$$

where \mathbf{E} and \mathbf{B} are the electric and magnetic fields, respectively, and \mathbf{j} is the electric current, which according to Ohm's law is

$$\mathbf{j} = \sigma(\mathbf{E} + \mathbf{u} \times \mathbf{B}). \quad (1.10)$$

In a non-relativistic environment and with sufficiently high conductivity of the fluid, the second term of Eq. (1.9) is negligible. Hence, Eq. (1.9) becomes

$$\nabla \times \mathbf{B} = \mu_0 \mathbf{j} . \quad (1.11)$$

Substituting Eq. (1.10) in Eq. (1.11) yields

$$\eta \nabla \times \mathbf{B} = \mathbf{E} + \mathbf{u} \times \mathbf{B} , \quad (1.12)$$

where, $\eta = 1/\mu_0\sigma$ is the magnetic diffusivity. Taking the curl of Eq. (1.12) and substituting Eq. (1.8) leads to the *induction equation*:

$$\frac{\partial \mathbf{B}}{\partial t} = \nabla \times (\mathbf{u} \times \mathbf{B}) - \nabla \times (\eta \nabla \times \mathbf{B}) . \quad (1.13)$$

If $\eta = \text{constant}$, and since $\nabla \times \nabla \times \mathbf{B} = \nabla(\nabla \cdot \mathbf{B}) - \nabla^2 \mathbf{B}$ and $\nabla \cdot \mathbf{B} = 0$, Eq. (1.13) can be written as

$$\frac{\partial \mathbf{B}}{\partial t} = \nabla \times (\mathbf{u} \times \mathbf{B}) + \eta \nabla^2 \mathbf{B} . \quad (1.14)$$

The first term on the right-hand side describes the magnetic field advected by plasma flows, and the second term describes the diffusion of magnetic field (ohmic decay) because of the finite conductivity in the plasma. The magnetic field in the photosphere is assumed to be radial as the observed magnetic field is only weakly inclined relative to the vertical (Wang and Sheeley, 1992; Solanki, 1993; Martínez Pillet, Lites, and Skumanich, 1997). It is assumed that there is no flux exchange between different layers, which constrains the radial component to evolve in the photosphere and the horizontal field components are decoupled from the radial field component (Mackay and Yeates, 2012).

The evolution of the radial magnetic field $B_r(\theta, \phi, t)$ in the photosphere is simulated in SFTM by

$$\begin{aligned} \frac{\partial B_r}{\partial t} = & -\Omega(\theta) \frac{\partial B_r}{\partial \phi} - \frac{1}{R_\odot \sin \theta} \frac{\partial}{\partial \theta} \left[v(\theta) B_r \sin \theta \right] \\ & + \eta_H \left[\frac{1}{R_\odot^2 \sin \theta} \frac{\partial}{\partial \theta} \left(\sin \theta \frac{\partial B_r}{\partial \theta} \right) + \frac{1}{R_\odot^2 \sin^2 \theta} \frac{\partial^2 B_r}{\partial \phi^2} \right] + S(\theta, \phi, t) - D(\eta_r) , \end{aligned} \quad (1.15)$$

where η_H is the surface magnetic diffusivity, $\Omega(\theta)$ is the differential rotation, $v(\theta)$ is the meridional flow, and R_\odot is the photospheric radius of the Sun. $D(\eta_r)$ is a linear operator to include decay caused by the radial diffusion with radial diffusivity η_r . It mimics the radial diffusion of the poloidal magnetic field into the convection zone, and it was introduced in some SFT models (e.g., Schrijver, DeRosa, and Title (2002); Baumann, Schmitt, and Schüssler (2006)) to obtain a realistic implementation of solar activity, for example, the evolution of the polar field. $S(\theta, \phi, t)$ is the source term in the SFTM through which the emergence of flux, with positive and negative polarities separated, is fed into the surface magnetic field treating the photospheric magnetic flux density as an equivalent surface magnetic charge density. The variables θ , ϕ , and t are the colatitude, longitude, and time at which a BMR is injected into the simulation.

The axisymmetric component of a BMR's magnetic field contributes to the axial dipole moment of a BMR. The axial dipole moment of a BMR gives the amount of flux, which may get transported to the poles and facilitates the cancellation and reversal of the polar fields. It is proportional to flux, tilt angle, and polarity separation.

The initial contribution of an individual BMR to the solar axial dipole field is defined as

$$D_{\text{BMR}} \propto d F \sin \theta \sin \alpha , \quad (1.16)$$

where d is the distance between the polarities, F is the total flux, θ is the colatitude, and α is the tilt angle. For the large-scale field, the strength of axial dipole component is given by

$$D_{\text{Axial}(t)} = \frac{3}{4\pi} \int_0^{\pi/2} \int_0^{2\pi} B_r(\theta, \phi, t) \cos \theta \sin \theta \, d\theta \, d\phi . \quad (1.17)$$

The decay time of the axial dipole field is about 30 years, when diffusion (for a diffusivity of $250 \times 10^6 \text{ m}^2/\text{s}$) alone is considered, and it is about 11 years for a pure advection scenario. In the presence of both diffusion and advection by flows, a fraction of magnetic flux crossing the equator and getting caught by the corresponding hemispheric meridional flow, which keeps them apart, occurs in simulations. [Jiang, Cameron, and Schüssler \(2014a\)](#) found that the contribution of BMRs to the axial dipole moment decreases with increasing latitude locations of BMRs (see Fig. 6 in [Jiang, Cameron, and Schüssler, 2014a](#)). The differential rotation has no effect on the axial dipole component, but the diffusion and meridional flows show different effects depending on the latitudinal locations of BMRs and on high/low diffusivity and the meridional flow ([Jiang, Cameron, and Schüssler, 2014a](#)).

With the surface flux transport model, we can simulate the magnetic field evolution on the far side of the Sun. The distribution of open and closed flux in the corona, which depends on the large-scale evolution of the solar surface flux, determines the strength and geometry of the interplanetary and heliospheric magnetic field. The amount of open flux from the Sun is correlated with the flux emergence in the photosphere ([Wang, Lean, and Sheeley, 2000](#)) and the sunspot number ([Solanki, Schüssler, and Fligge, 2000, 2002](#)). Simulation of the surface magnetic field for the earlier centuries can be applied to past-climate studies, and they can also be cross-calibrated with such studies. Hence, they are not only important in dynamo studies but also in space weather and climate research. Further details about models and applications can be found in [Mackay and Yeates \(2012\)](#).

Chapter 2

Sunspot areas and tilt angles for solar cycles 7–10

V. Senthamizh Pavai, R. Arlt, M. Dasi-Espuig, N. A. Krivova, and S. K. Solanki

Astron. Astrophys. 584, A73. Accepted 21 August 2015

Solar activity is apparently driven by internal magnetic fields, which are roughly oscillatory in time. Sunspots are the most obvious manifestations of solar activity in visible light, and it was Samuel Heinrich Schwabe (1844) who first published a paper on the abundance of sunspots as a cyclic phenomenon.

Apart from the number of sunspots and various indices that can be defined from their appearance, there are other properties that contain information about the underlying process of generating variable magnetic fields in the solar interior. The most prominent feature is the distribution of spots in latitude versus time (butterfly diagram; Carrington, 1863). The latitudes of the spots give us an idea of the location of the underlying magnetic fields. In the majority of attempts to explain the dynamo process of the Sun, it is assumed that strong azimuthal magnetic fields emerge as sunspots at the solar surface (for a review, see Charbonneau, 2010). These internal horizontal (i.e. parallel to the solar surface) fields become locally unstable and form loops eventually penetrating the surface of the Sun. At this stage, two polarities are formed, which are actually measured and often accompanied by sunspot groups (for a review, see Fan, 2004). Alternatively, sunspots may form as a consequence of a large-scale magnetic field suppressing the convective motions and thereby reducing the turbulent pressure. The lower pressure at the field location compresses the flux even further leading to further turbulence suppression, and an instability can occur (Kleerorin, Rogachevskii, and Ruzmaikin, 1989; Warnecke *et al.*, 2013).

The radial magnetic field within active regions provides poloidal fields to the dynamo system. The production of poloidal magnetic flux is an essential ingredient in the sustainability of the Sun's large-scale magnetic field. The angle the group polarities form with the solar equator is called the tilt angle and was first measured by Hale *et al.* (1919). On average, the leading polarity of the group is slightly closer to the solar equator than the following one. The dependence of the average tilt angle on the emergence latitude of the sunspot groups is often referred to as Joy's law, according to the paper mentioned above.

Tilt angles from sunspots in white-light images were computed by Howard (1991) from Mt. Wilson images and by Sivaraman, Gupta, and Howard (1999) from Kodaikanal images. From those data, average tilt angles were obtained by Dasi-Espuig *et al.* (2010, 2013) for the solar cycles 15–21. An anti-correlation between the average tilt angle and the amplitude of the corresponding cycle was found. Additionally, the product of this average and the cycle amplitude correlates significantly with the strength of the next cycle. We come back to more recent tilt angle determinations in Sects. 2.3.3 and 2.4.

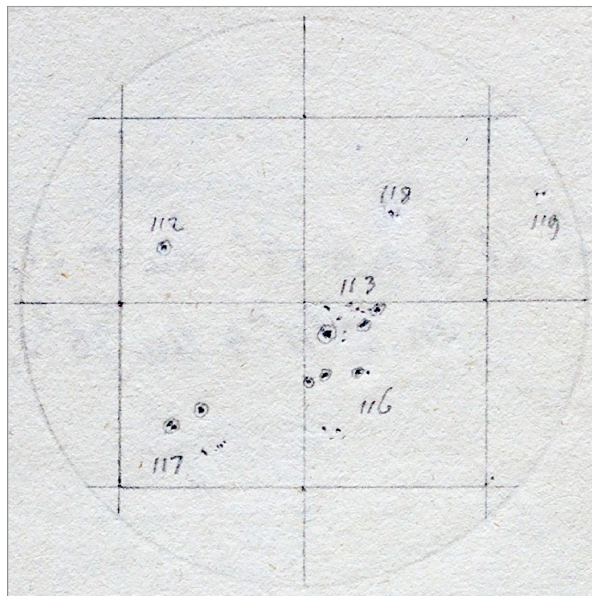


Figure 2.1: Example of the drawing style in the main period of 1831–1867. This full-disk drawing of 1847 July 22 shows spots with and without penumbrae. The drawing also shows two group designations (116 and 117) which actually refer to two individual groups each (see Sect. 2.2, also for the treatment of more difficult cases such as group 113).

Based on magnetograms from Kitt Peak, Wang and Sheeley (1989) determined tilt angles for cycle 21 and obtained a large average value of 10° , a result confirmed by Stenflo and Kosovichev (2012) from MDI data. Recently, Wang *et al.* (2015) compared tilt angles from white-light images of the Debrecen Photoheliographic Database and from Mt. Wilson magnetograms for cycles 21–23. They found that magnetogram tilt angles tend to be larger than those from sunspot groups in white-light images, both because a substantial fraction of the white-light tilt angles refer to sunspots of the same polarity, and because the magnetograms include magnetic flux from plage regions typically showing higher tilts than the sunspots of the same active region. We address the first issue in this paper.

This paper is based on the digitized observations by Samuel Heinrich Schwabe¹ (Arlt, 2011) of cycles 7–10 and extends the subsequent measurements of all positions and estimates of the sizes of the sunspots drawn in these manuscripts (Arlt *et al.*, 2013). The initial sizes were in arbitrary units corresponding to pixel areas in the digital images and may not be to scale. We describe the method of converting these sunspot size estimates into physical areas in Sect. 2.1, an attempt at defining proper sunspot groups in Sect. 2.2, the computations of the tilt angles in Sect. 2.3 and summarise the results in Sect. 2.4.

2.1 Calibration of sunspot areas

Apart from the importance of having reliable sunspot area information for the Schwabe period, we also need to know the individual sunspot areas for reasonable estimates of the two polarities

¹Schwabe carried out sunspot observations from Dessau in Germany from 1825 October 1 to 1867 December 31 using several telescopes. He recorded his observations in 39 books, which are preserved in the Royal Astronomical Society in London. His notes do not contain the information about the orientation of his telescope(s), however, most of the drawings have grid lines. The tests with a superimposed heliographic grid, with horizontal diameter aligned to celestial equator, provided an acceptable spot distributions. Hence for all drawings with grid, a coordinate system with horizontal diameter aligned to the celestial equator was assumed. For drawings without grid, which mostly belong to the initial period of his observations, either coordinate systems from rotational matching or horizontal coordinate systems were assumed. In rotational matching method, displacements of spots over the days are used to identify the orientation of the drawings (For a detailed description, refer Arlt *et al.*, 2013).

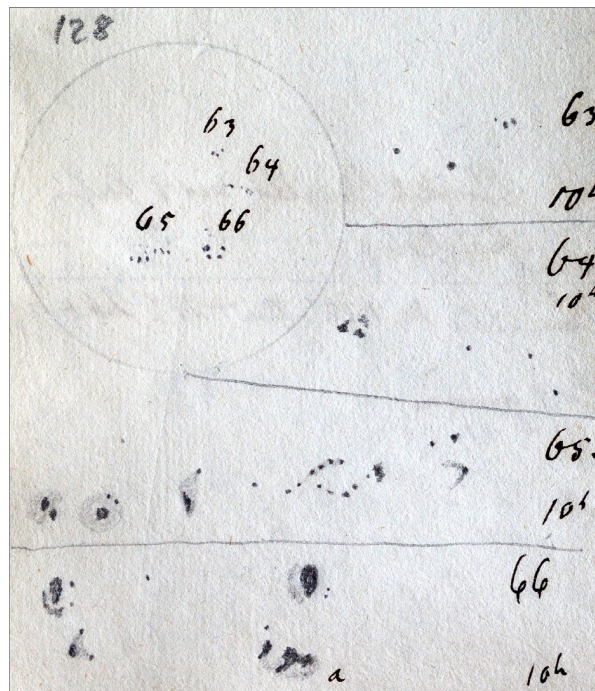


Figure 2.2: Example of the drawing style in the initial period of 1825–1830. This full-disk drawing of 1827 June 13 shows large spots which combine several umbrae and at least part of the penumbral area, as is revealed by the detailed drawings.

and their locations in sunspot groups when determining the tilt angles of sunspot groups. The sunspot areas may be seen as proxies for the magnetic flux (e.g. [Houtgast and van Sluiter, 1948](#); [Ringnes and Jensen, 1960](#), for early studies), although the relation of the two may be complex, as emphasised recently by [Tlatov and Pevtsov \(2014\)](#).

Schwabe plotted the sunspots into relatively small circles of about 5 cm diameter, representing the solar disk. Given the finite width of a pencil tip, at least small spots must have been plotted with an area larger than a corresponding structure on the Sun would have at that scale. Pores, if plotted to scale, would need to have diameters of 0.04–0.1 mm in this kind of drawing. The umbral areas measured in the drawings, therefore, need to be converted into physical areas on the Sun.

There are two ways of obtaining physical sizes of the sunspots drawn by Schwabe. The one requires the existence of high-resolution drawings by other observers within the observing period of Schwabe for calibration. The other is a statistical approach using data sets of the 20th century to calibrate the sizes. We first describe the latter method, since the number of high-resolution drawings by other observers that can be employed for the first method is very limited. The statistical approach also required a splitting of the data into two sets: 1825–1830 and 1831–1867. This is due to a change in the drawing style after 1831 Jan 1, as demonstrated in Figs. 2.1 and 2.2. In the initial period, Schwabe plotted spots without distinction of umbrae and penumbrae. In the second period starting in 1831, Schwabe distinguished umbrae from penumbrae. In those cases, umbral sizes were measured. We begin with the second period when areas are clearly umbral and afterwards describe a work-around for the conversion of sunspot sizes to umbral areas in the initial period until 1830.

2.1.1 Indirect umbral areas for 1831–1867

One approach to obtaining physical areas of the sunspot sizes is of a statistical nature. Sunspots were divided into 12 classes by size, as introduced by [Arlt *et al.* \(2013\)](#). The measurements were actually carried out with 12 different circular cursor shapes with areas from 5 to 364 square

pixels. Their shapes and screen areas are shown in Fig. 2.3. The classes increase monotonously in area, but were chosen relatively arbitrarily. Any more precise individual pixel counts of umbral areas are unlikely to yield more accurate data, since the drawings are meant to be sketches of the sunspot distributions and sizes rather than exact copies. More details are given by [Arlt et al. \(2013\)](#).

The division into 12 size classes is done both for Schwabe’s data set and for a modern data set (see below), whereby for the modern data set the classes are chosen such that each class has the same relative number of sunspots as the corresponding class in Schwabe’s data. In other words, the relative abundances of the 12 size classes of the Schwabe spots are compared and calibrated with 20th century data by building histograms of 12 artificial size classes constructed to contain the identical abundances. The average umbral area in this kind of artificial class gives us the umbral area corresponding to a Schwabe size class. Finally, a function for the area depending on the heliocentric angle of a spot from the centre of the solar disk is fitted for each size class. We refer to this angle as ‘disk-centre distance’ δ in the following.

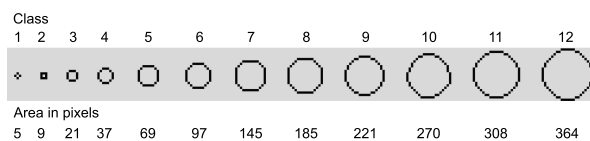


Figure 2.3: Twelve cursor shapes (size classes) used for the size estimates of the sunspots drawn by Schwabe. The bottom line gives the area in square pixels on the screen, including the black border pixels.

The reference data sets used to obtain a statistical mapping of sunspot umbral areas are from photoheliographic data of the observatories of Debrecen, Mt. Wilson, Kodaikanal, and the Michelson Doppler Imager (MDI) instrument of the Solar and Heliospheric Observatory (SOHO). As described by [Györi \(1998\)](#), an improved automatic analysis method was used for the Debrecen data starting in 1988. Before that, from 1974 to 1987, the areas were measured by video techniques ([Dezső, Kovács, and Gerlei, 1987](#)). In the 1974–1987 data, the area values of larger sunspots at disk-centre distances $\delta > 60^\circ$ increase very rapidly with δ . This effect is not seen in the area values measured from 1988 onward, therefore, we used only the Debrecen data from 1988–2013. The Mt. Wilson data were analysed by [Howard, Gilman, and Gilman \(1984\)](#) and contain spot properties from 1917–1985. The Kodaikanal data, covering 1906–1987, were obtained in almost the same way as the Mt. Wilson data ([Sivaraman, Gupta, and Howard, 1993](#)). The MDI data for 1996–2010 were obtained using a telescope of 4 arc seconds resolution ([Watson, Fletcher, and Marshall, 2011](#)) which is similar to or perhaps a bit worse than the resolving capabilities of Schwabe’s set-up. The data from the Greenwich Photoheliographic Database were not used because it contains group area totals instead of areas of individual spots.

Typical diameters of solar pores in white light are between 1×10^6 m and 4×10^6 m ([Keppens and Martínez Pillet, 1996](#)), which converts to $0.8\text{--}13 \times 10^{12}$ m² or 0.26–4.1 MSH. We are using a lower limit of 1 MSH for the construction of the histogram as argued below. In the Debrecen data, integer values of the projected area in millionths of the solar disk (MSD) are given (0, 1, 2, ...), while the corrected areas are given in MSH, also as integer values. Since the projection correction increases the area, whereas the conversion to MSH reduces the value by half, the lower limits of 1 in both quantities are therefore statistically compatible. We discarded all spots smaller than 1 MSH from the other data sets before the analysis. Ideally, one would want to define a minimum spot size plotted by Schwabe, but in reality, his drawing style was not that straightforward. Whenever he detected a small group on the Sun, he indicated its location with small dots. In more complex groups, however, he did not indicate all the small spots because of their abundance. There is apparently no clear lower limit for the spot size. We therefore use a compromise at this point, excluding the smallest pores, and start from 1 MSH, which is also the lower limit in the Debrecen data.

The relative abundances of the 12 cursor size classes, denoted by $i = 1, 2, \dots, 12$, are determined for three different ranges of disk-centre distances, which were $\delta < 30^\circ$, $30^\circ\text{--}60^\circ$, and $60^\circ\text{--}70^\circ$. These distance classes are numbered as $d = 1, 2, 3$. The upper limit of 70° is because not all reference data sets contain spots beyond that distance. The four reference data sets (this number is denoted by N in the following) are now also divided into 12 classes fulfilling the same relative abundances as obtained for the Schwabe classes, again split into the three selected ranges of distances. The histograms are based on the umbral areas, which are corrected for foreshortening. We therefore expect a mapping of size classes with a fairly small dependence on δ .

Then the area for each cursor size is calculated by the unweighted average of all spots

$$\bar{A}_{id} = \sum_{n=1}^N \sum_{j=1}^{S_{nid}} A_{njid} \bigg/ \sum_{n=1}^N S_{nid}, \quad (2.1)$$

where \bar{A}_{id} is the area for a cursor of i -th size class in the d -th disk-centre distance class, A_{njid} is the umbral area (corrected for projection by $\cos^{-1} \delta$) of the j -th spot in the n -th data source, i -th size class and d -th distance class, and S_{nid} is the total number of spots present in n -th data source, i -th size class in d -th distance class. These averages consist of different histogram bins for different n . For example, the equivalent class-5 bin in the Debrecen data has other area limits than the equivalent class-5 bin of the MDI data. The averaging helps smooth possible systematic over- or underestimations of areas in the 20th century data sources. The averages \bar{A}_{id} are not immediately areas corrected for foreshortening, since the histogram classes are constructed using Schwabe's raw sunspot sizes. We capture any possibly remaining disk-centre distance dependence in Sect. 2.1.4, where functions through the three distance classes for each i are derived, i.e. 12 functions for the 12 size classes.

2.1.2 Indirect umbral areas for 1825–1830

The sunspots in the early full-disk drawings from 1825 to 1830 were not drawn at a good resolution. Instead, Schwabe plotted high-resolution magnifications at unknown scale beside the full-disk drawings. The magnifications show that nearby spots were combined in the full-disk drawings. The spots in these drawings are therefore often ‘blobs’ made out of very close spots and including the penumbrae between those spots. Hence, the pencil dots used to measure the sizes of those spots do not represent their umbral area. To estimate the area for these spots, we need to compare the size statistics with grouped spots including penumbrae. To do that, we combined the spots inside a single penumbra in a modern data set and used these for the statistical estimation of the area.

Among the data used here, the Debrecen data is the only source that contains umbral and penumbral areas broken down into individual spots. Recently, Tlatov *et al.* (2014) published detailed measurements of the Kislovodsk Mountain Astronomical Station. Since those only cover the somewhat peculiar cycle 24, we prefer not to use them for the area calibration of Schwabe's drawings. The conversion of the 1825–1830 data is therefore based on the Debrecen data (1988–2013) as a mixture of different cycles. From that source, we prepared a data set in which all the umbrae inside a continuous penumbra are added and considered as a single spot of which we store the whole-spot area and the total umbral area in each spot. Now we divide the whole-spot areas into 12 classes with the same relative abundances as we obtained from Schwabe's 1825–1830 data, but use the corresponding umbral areas for an average, according to Eq. (2.1), for each size class in each distance class. The results for the distance classes are again combined into a function of the disk-centre distance in Sect. 2.1.4.

There are still differences between these combined spots from the Debrecen data and the pre-1831 Schwabe spots. (1) A penumbra with a single umbra would look similar to a penumbra

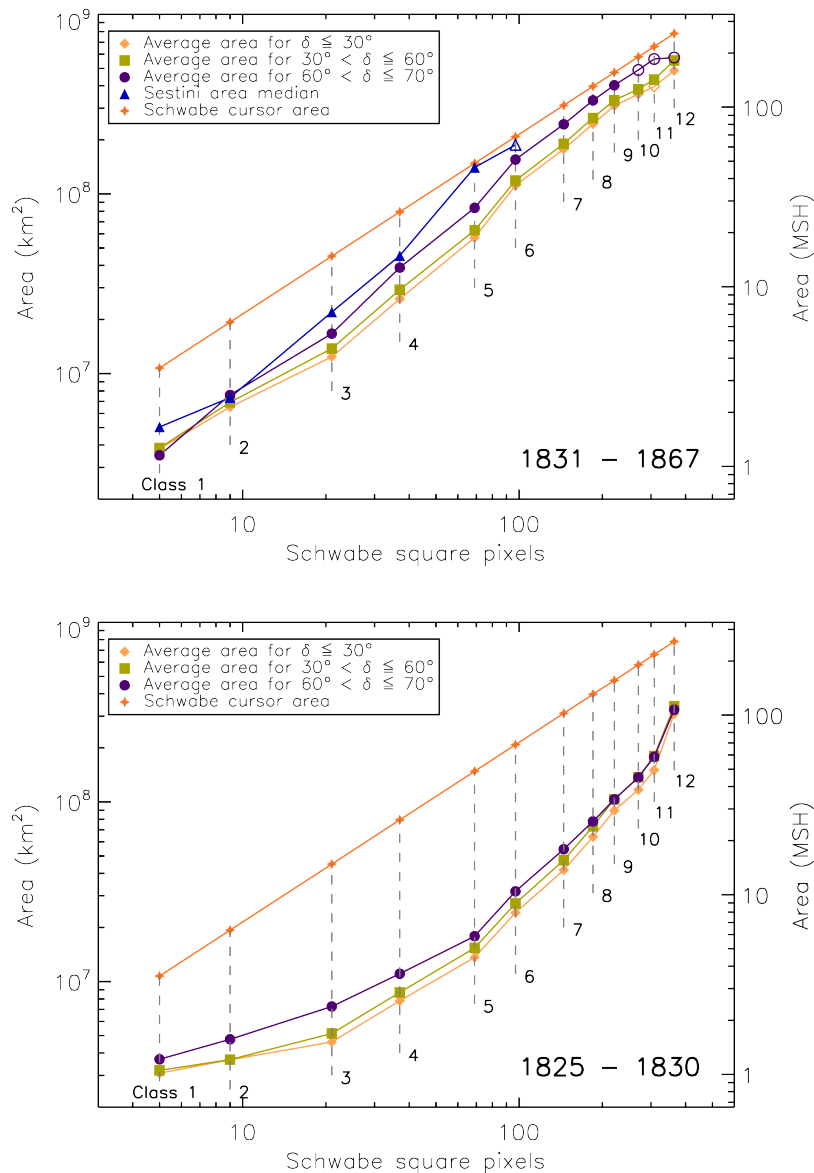


Figure 2.4: Average areas in km^2 (left ordinate) and MSH (right ordinate) for each of the 12 size classes (abscissa), and for three different centre-distance ranges: $< 30^\circ$ (diamonds), 30° – 60° (squares), and 60° – 70° (circles). The areas corresponding to the simple pixel areas of the size classes without any calibration are indicated with plus signs. The direct calibration of size classes by observations from Sestini in 1850 are shown as triangles. *Top:* average areas for the data from 1831–1867. *Bottom:* average areas for the data from 1825–1830. An open symbol means that the number of spots used in the calculation of the average area is less than 20. The lower curves in the bottom panel do not imply smaller areas, but they rather mean that any spot of a given true area was drawn as a spot of larger class in 1825–1830 than in 1831–1867.

with two umbrae in Schwabe’s drawings. The penumbral area between the two umbrae in the latter case, however, leads to different total umbral areas when derived from the Debrecen data. (2) Schwabe did not always plot the entire penumbra in a ‘blob’. (3) All the umbrae inside a penumbra are added in the Debrecen data, even for very extended penumbrae. Schwabe, however, did not club together all the umbrae inside a connected penumbra when it was very large, but plotted ‘sub-penumbrae’ in that case.

There are 38 spots apparently drawn without the inclusion of a penumbra which were found from the visual comparison of disk drawings with magnifications. These spots were not used in the procedure described here; their areas were calculated using the method discussed in Sect. 2.1.1.

2.1.3 Umbral areas from parallel observations

For a short period from 1850 September 19 to November 4, large-scale drawings are also available from Sestini who observed from Washington, D.C., comprising a total of 42 full-disk graphs (Sestini, 1853). We compiled spots seen by both Schwabe and Sestini and measured the umbral areas of the corresponding spots in Sestini’s drawings. There were not enough observations to cover the whole range of size classes – we could only cover classes 1–6. We come back to the results in the following section. We need to bear in mind that the time difference between the observations from Dessau and those from Washington implies changes in the evolution of the spots either leading to wrong areas or to wrong spot associations between the two observers.

2.1.4 Final mapping of sunspot sizes

Figure 2.4 shows the mappings of Schwabe size classes to physical areas in km^2 and MSH for three different ranges of disk-centre distances for the statistical conversion as well as a mapping for the calibration with concurrent high-resolution observations. One immediate result is that the direct conversion of the pencil spots in Schwabe’s drawings into sunspot areas would lead to overestimated umbral areas in most size classes. One can also see that the areas corresponding to the pixel areas do not form a linear function or power law. The areas from the comparison with the sunspots observed by Sestini in 1850 are in good agreement with the indirect mapping based on size distribution. This shows that the direct conversion of pixel areas into sunspot areas is not a good choice. The only exception is class 5, but it only contains 21 measurements and may be a poor estimate (as is the one for class 6).

The bottom panel of Fig. 2.4 appears to show much smaller areas. This is not true, however. The graph actually shows that a 5-MSH spot which was typically drawn as a class-3 dot in 1831–1867, was represented by a class-5 dot before that period, since it encompassed a considerable fraction of the penumbra at that time. The areas of class 3 in the top panel cannot be compared with the areas of class 3 in the bottom panel. Sunspot sizes corresponding to large size classes were much more often used by Schwabe in the period of 1825–1830 than afterwards (there are no longer open symbols with fewer than 20 spots in the bottom panel).

The dependence of final areas on the disk-centre distance is described by functions of the form

$$\mathcal{A}_i(\delta) = a_i + (b_i / \cos \delta), \quad (2.2)$$

where a_i and b_i are coefficients for the i -th size class and δ is the distance of the spot from the centre of the solar disk. In the end, there are 12 functions for the period 1825–1830 and another 12 functions for the period 1831–1867. They deliver a mapping of the size classes into physical areas.

When computing the areas for the final sunspot data base, the area is not calculated if a spot distance is greater than 85° from the disk centre, since the area values become very uncertain. All spots with $\delta \leq 70^\circ$ are reliable in the sense that they are covered by the statistics leading to the mapping. All spots with $70^\circ < \delta \leq 85^\circ$ are uncertain because they rely on an extrapolation of the mapping, while all spots with $\delta > 85^\circ$ are highly uncertain and are therefore excluded from the data base. The smallest sunspot area occurring in our data after applying Eq. (2.2) is 1 MSH, which is consistent with the initial lower limit for spots in the reference data sets.

2.1.5 Distribution of sunspot area

The data base of Schwabe’s observations contains a total of 135 921 entries comprising 134 386 spots with size estimates (each line corresponds to an individual umbra) as well as 1535 spotless days (each line corresponds to a day with zero spot size). Whenever we use the term spots

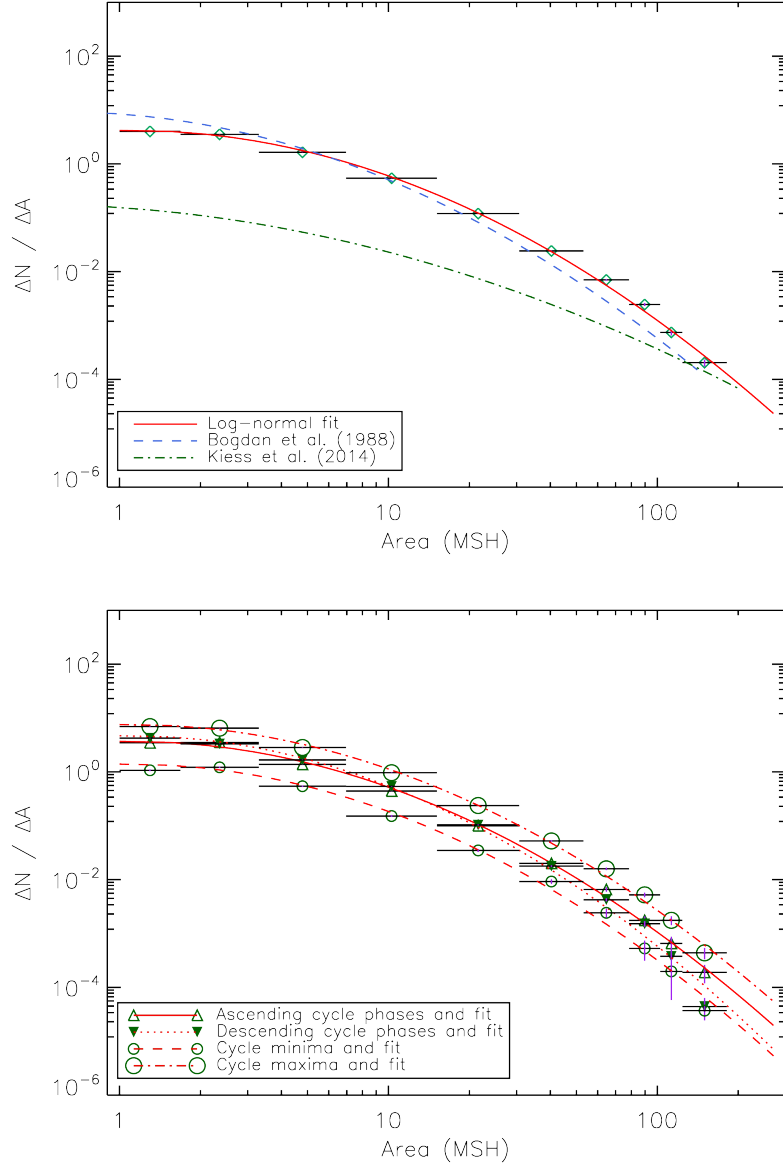


Figure 2.5: Distribution of estimated umbral areas of sunspots. *Top:* the area distribution for 1831–1867. The solid curve shows the log-normal fit. The dashed curve and dash dot curve are the fit curves from [Bogdan *et al.* \(1988\)](#) and [Kiess, Rezaei, and Schmidt \(2014\)](#), respectively. The horizontal bars show the widths of the bins. The error margins on the distribution values are all smaller than the symbols. *Bottom:* the area distribution of spots for ascending phases, descending phases, cycle minima and maxima of all cycles within 1831–1867. The lines show the log-normal fits for the corresponding area distributions.

we refer to individual umbrae as far as Schwabe resolved them. Positions are not available for 849 umbrae because the orientation of the drawing could not be identified. No physical areas are available because δ is missing. There are another 41 umbrae beyond 85° from the centre of the disk for which areas are not calculated because of too large uncertainties. The area values are therefore available for 133 496 umbrae. To study the distribution of areas, we consider the spots within $\pm 50^\circ$ central meridian distance (CMD) and within $\pm 45^\circ$ latitude. The same latitude limit was chosen by [Bogdan *et al.* \(1988\)](#). The central meridian limit, however, was $\pm 7.5^\circ$ in [Bogdan *et al.* \(1988\)](#) in order to avoid duplicate counts of groups (a group typically appears only once in a 15° window because of the solar rotation). Since drawings by Schwabe are not available for all days, we need to widen this window reasonably and found $\pm 50^\circ$ a good compromise between not missing too many groups because of observing gaps, on the one hand, and the contamination by duplicate consideration of groups, on the other hand. The latter does not actually affect the distribution significantly since [Baumann and Solanki \(2005\)](#) and [Kiess, Rezaei, and Schmidt \(2014\)](#) did not see any drastic changes between counting umbrae only once and counting them every day they were visible. The lowest area considered for the distribution is our lowest area, 1 MSH. The above criteria reduce the data to a sample of 104 217 spots in total, and 96 984 spots from 1831 to 1867.

The umbral area spectrum was obtained as described by [Bogdan *et al.* \(1988\)](#) with the exception that they used a lower umbral area limit of 1.5 MSH. Since the distribution is differential, the different lower limit should not affect the shape of the curve. The bins for small areas were selected such that each bin encompasses approximately one size class up to class 9, whereas one additional bin was defined such that it contains the spots from class 10 and about half the spots in class 11. All spots even larger than that (≥ 185 MSH) were outside the above mentioned CMD window. Dividing the area range into 20 bins as in [Bogdan *et al.* \(1988\)](#) would have caused a strong scatter since the Schwabe areas accumulate near 12 typical area values because the dependencies on the disk-centre distance described by (2.2) are all small.

The area distribution of the Schwabe spots also resembles a log-normal distribution and looks similar to the curve by [Bogdan *et al.* \(1988\)](#). The parameters for this kind of distribution over the area A are obtained through a fit by the function

$$\ln \left(\frac{dN}{dA} \right) = -\frac{(\ln A - \ln \langle A \rangle)^2}{2 \ln \sigma_A} + \ln \left(\frac{dN}{dA} \right)_{\max}, \quad (2.3)$$

where $(dN/dA)_{\max}$ is the maximum of the area distribution function, $\langle A \rangle$ is the mean, and σ_A is the geometric standard deviation. Table 2.1 shows the log-normal fit parameters obtained with a Levenberg-Marquardt least-squares method. The cycle minima and maxima were taken from the ‘‘Average’’ column of the cycle timings by [Hathaway \(2010\)](#). Minima periods and maxima periods are defined as ± 1 yr around the minima/maxima, while the ascending and descending phases are the remaining periods.

The top panel of Fig. 2.5 shows the resulting total area distribution of umbrae for 1831–1867. The errors on the ordinate values were estimated by $(\Delta N/\Delta A)/\sqrt{\Delta N}$, where $\Delta N/\Delta A$ is the discrete area distribution value and ΔN is the number of spots in each bin. The errors are all smaller than the symbols. The lower curve from Fig. 1 in [Bogdan *et al.* \(1988\)](#), which is the fit to the full range of umbral areas of 1.5–141 MSH, and the curve from [Kiess, Rezaei, and Schmidt \(2014\)](#) are also plotted in Fig. 2.5 for comparison. While the data of both analyses also influence our size calibration of Schwabe’s sunspots, the distribution only agrees with that by [Bogdan *et al.* \(1988\)](#) based on Mt. Wilson data. Interestingly, the area distributions obtained from group umbral areas ([Baumann and Solanki, 2005](#)) also agree fairly well with our results. The peak position $\langle A \rangle$ of their log-normal distribution from the Greenwich group data is ten times larger than our peak position from individual spot data, in good agreement with the fact that sunspot groups consist of roughly ten spots on average.

The bottom panel of Fig. 2.5 shows four individual area distributions for the ascending and descending phases of the cycles as well as for the cycle minima and maxima. They exhibit

Table 2.1: Log-normal fit parameters for the Schwabe data and various subsets of them.

Data	Umbrae	$\langle A \rangle$ [MSH]	σ_A [MSH]	$\left(\frac{dN}{dA}\right)_{\max}$ [MSH ⁻¹]
All data (1825–1867)	104 217	1.05	3.8	3.8
1825–1830	7 233	0.58	9.9	1.7
1831–1867	96 984	1.10	3.5	4.2
Cycle 7	9 448	1.09	5.3	1.3
Cycle 8	22 382	1.08	3.8	4.0
Cycle 9	36 862	1.08	3.0	5.3
Cycle 10	35 181	1.10	3.4	4.9
Ascending phases	13 613	1.09	3.5	3.7
Descending phases	46 763	1.10	3.1	4.7
Cycle minima	3 507	1.08	3.4	1.4
Cycle maxima	31 131	1.10	3.6	7.6

nearly the same distribution as the whole area distribution. The descending phases of all cycles have larger $(dN/dA)_{\max}$ than the ascending phases, however. The fairly small variation of σ_A is remarkable and confirms the corresponding findings by [Bogdan *et al.* \(1988\)](#) and [Schad and Penn \(2010\)](#).

The umbral area distribution was calculated for the data from 1825–1830 and from 1831–1867 separately, and the fit parameters are listed in [Table 2.1](#). The distribution for the earlier period is much wider, with σ_A similar to that by [Kiess, Rezaei, and Schmidt \(2014\)](#) who derived $\sigma_A = 10.7$ ($\sigma = 1.54$ in their work).

2.2 Group definitions

Tilt angles of groups are sensitive to the actual association of spots into groups. Schwabe’s original drawings contain group names that he started from number one every new year. His perception of a group was often too broad. A fair number of sunspot clusters actually contain two or more groups. This new definition of the groups was made via manual inspection of the drawings. We also used the evolutionary information of the clusters and sub-clusters provided by the images of adjacent days. Very often, a small apparently new bipolar group emerged near an existing bipolar group and showed its individual evolution through the Waldmeier (or Zurich) types. Schwabe included them in the group number of the existing group, while we defined a new group in many of these cases. In other cases, when splitting of the polarities was not obvious and the parts of the group were all in the same evolutionary phase, we kept Schwabe’s definition, despite leading to somewhat large groups of 30° extent or more. Any splitting, however, would have been very arbitrary and would add noise rather than new information to the tilt angle data base. A total of 56 groups with extents $\geq 30^\circ$ size remained.

[Figure 2.6](#) shows the ratio of the number of newly formed groups, i.e. those obtained by splitting Schwabe’s original groups, to the original number of groups. For instance, if there were a total of ten groups which were all split into two, resulting in ten new groups, the ratio would be one (100% splitting). The large fraction of splittings seen after 1850 is partly due to the presence of very many closely located groups, but chiefly due to a wider definition of groups Schwabe adopted during those cycles. In nine cases, Schwabe assigned one group designation each to two spots, while they apparently form one bipolar group. We combined those cases to one group name.

Table 2.2: Statistics of coverage, spot areas, groups, and tilt angles α for Schwabe’s observations in 1825–1867.

Period	Days with Gaps longer than 5 days ^a	Gross groups with areas	Unique groups with areas	Groups with tilt	Group tilts with $ \text{CMD} < 60^\circ$	Group tilts with $ \text{CMD} < 60^\circ$ and $\alpha > 3^\circ$
1825–1830	1187 (63.0%)	32	4401	945	2452	1745
1831–1867	8808 (65.2%)	149	27116	5903	20689	13803
Total	9995 (64.9%)	182 ^b	31517	6848	23141	15548

Notes. CMD is the central meridian distance of the area weighted centre of a group.

^a The gaps are derived only from the days for which we obtained data; if we include the unused drawings, the number of gaps longer than five days is a bit smaller than the number given in this column.

^b One group is missing in the 1825–1830 number because a gap straddles 1830 and 1831.

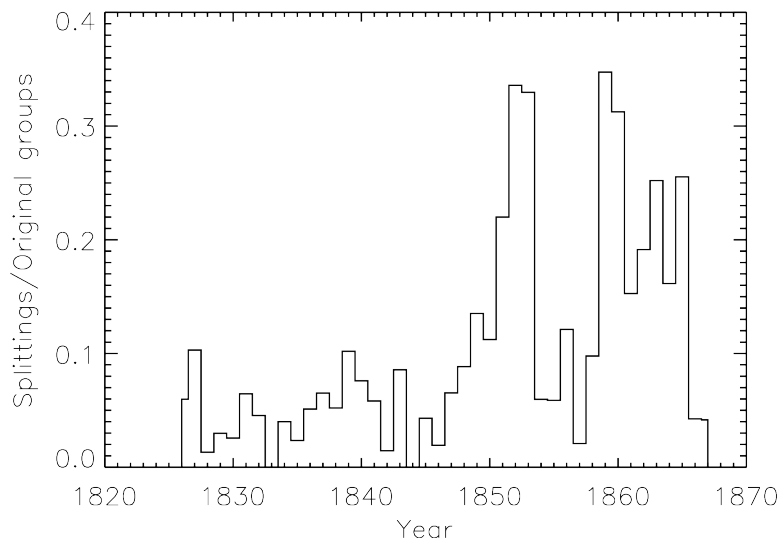


Figure 2.6: The number of new groups obtained by splitting Schwabe’s original groups, normalised to the number of groups before splitting (i.e. Schwabe’s original groups). The criteria for splitting a group are described in the main text.

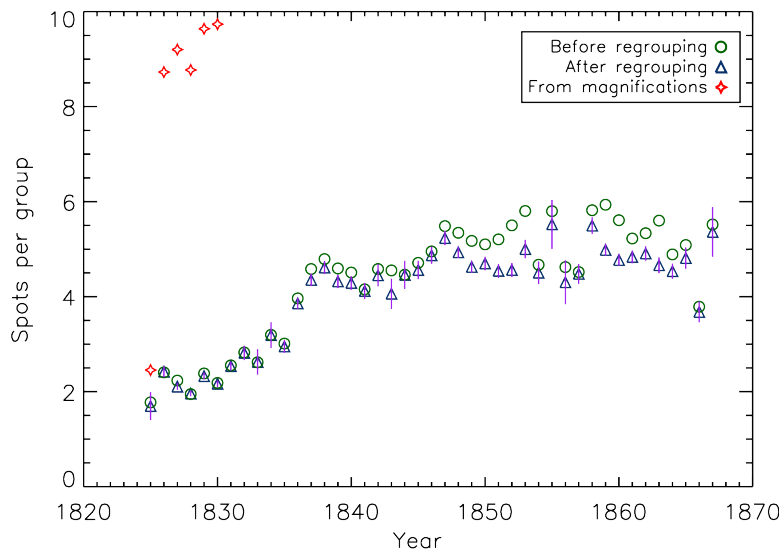


Figure 2.7: Annual averages of the number of spots per group calculated before the regrouping of sunspot groups (circles), after regrouping (triangles), and manually counted number of spots from the magnification drawings of sunspot groups (diamonds). Uncertainties are only given for the values after regrouping and are obtained from the relative Poissonian error $1/\sqrt{n_{\text{counts}}}$, where n_{counts} are the number of all instances of all groups in a given year (groups count several times with different numbers of spots).

The splittings are marked by modified group names in the above mentioned data file. The two groups 116 and 117 in Fig. 2.1 now appear as four groups, 116-0, 116-1, 117-0, and 117-1 in the catalogue. Combined groups are labelled with plus signs in the new group name, e.g. 39+40.

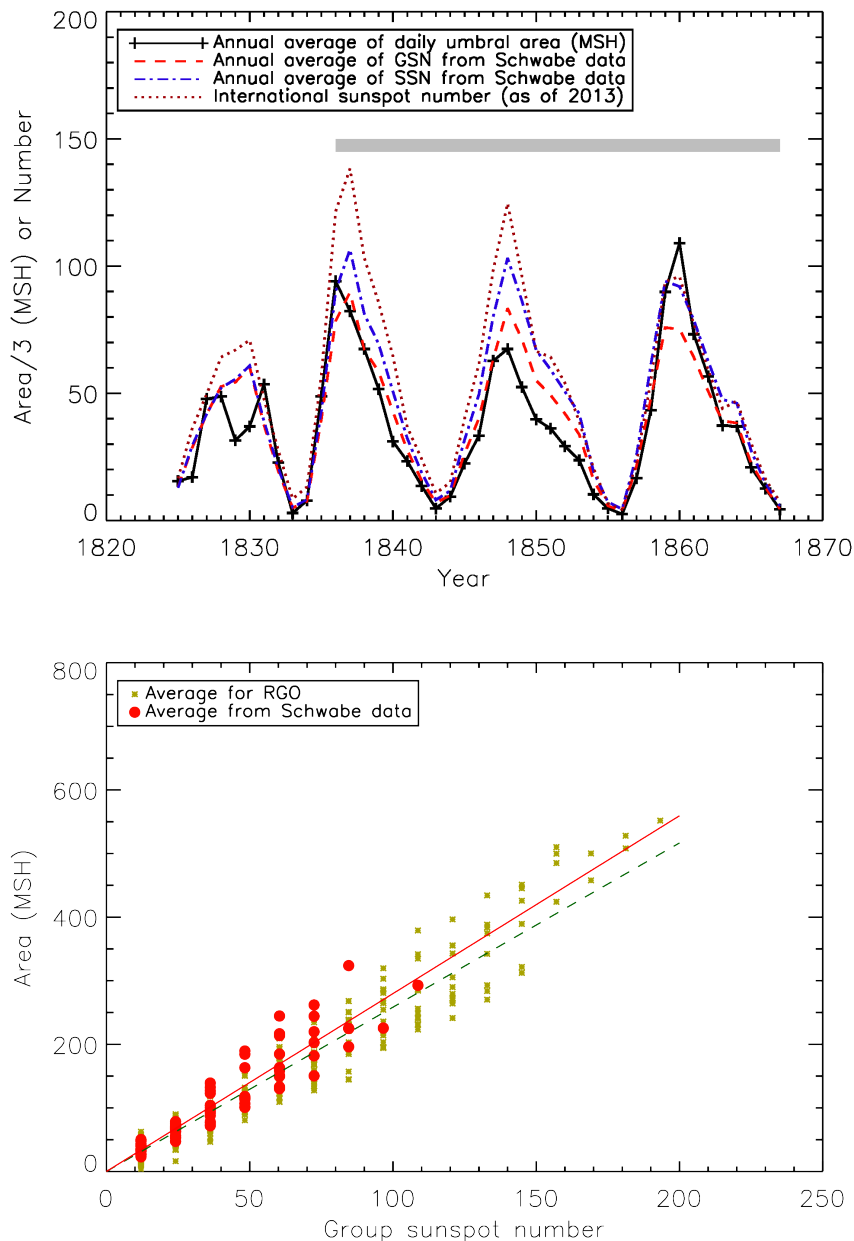


Figure 2.8: *Top:* annual averages of total-disk umbral area of sunspots in MSH and divided by three (solid line), the group sunspot number (GSN) derived from our groupings (dashed line), the sunspot number (SSN; Wolf number) derived from our groupings and the actual number of spots in the full-disk drawings (dash-dotted line), and the official International Sunspot Number (dotted line) of before the revision suggested by [Clette et al. \(2014\)](#) which was not yet available. The grey horizontal bar indicates the period in which the number of spots per group was fairly constant (cf. Fig. 2.7). *Bottom:* daily total umbral areas versus GSN (in case of Schwabe, the GSN is based on our grouping in Schwabe’s drawings, corresponding to the dashed line in the top panel), averaged over 100 values in each group sunspot number bin for the Schwabe data (circles) and the Greenwich data (asterisks). The solid and dashed lines are linear fits through the Schwabe and Greenwich data, respectively, which must go through the origin.

To demonstrate the impact of the regrouping (splitting as well as combining), Fig. 2.7 shows the annual averages of the number of spots per group, derived from Schwabe’s group definitions and derived after regrouping by visual inspection. Additionally, the sunspot group magnifica-

tions drawn by Schwabe (see Fig. 2.2) were used to compute a third set of average spot numbers per group. Since the magnifications are not biased towards exceptionally large groups until 1830, we give only the averages for 1826–1830. These spot numbers per group obtained from detailed drawings of individual groups match modern values very well (Tlatov, 2013; Clette *et al.*, 2014). After 1830, only selected, big groups were magnified, so the values of spots per group are biased.

In the averages derived from the full-disk drawings, there is a significant increase in the number of spots per group from 1830 to 1836. This increase was not flattened after the regrouping of sunspot groups. This may be partly due to initially smaller true numbers of spots per group and partly due to the early, coarser drawing style of Schwabe. The most notable jump from 1835 to 1836 does not coincide, however, with the change in drawing style in 1830/1831. An increase in the number of spots per group can also be seen after the other minima, namely in 1843–1847, 1856–1858, and 1866–1867. Therefore, the change in drawing style and recovery from the activity minimum in 1833 are probably superimposed effects.

By the same token, we may spot small peaks coinciding with the solar cycle maxima 8, 9, and 10 in Fig. 2.7. This effect has also been observed, even more drastically, by Clette *et al.* (2014) in 20th century data, and it may actually be a mixture of a real effect and observational bias (basically because on a crowded Sun, the splitting of groups is difficult).

The top panel of Fig. 2.8 shows the annual averages of umbral areas of sunspots. They are compared to the yearly averages of the group sunspot number (GSN) according to our own group number information and the (Wolf or Zurich) sunspot number (SSN), both derived from Schwabe’s observations, as well as to the International Sunspot Number (ISN).² Good agreement is found between umbral areas and Schwabe’s group sunspot number for cycle 8, while the areas of cycles 7 and 9 fall below the (rescaled) sunspot numbers and cycle 10 has larger areas than the sunspot numbers indicate. Since Schwabe’s observing method, telescope and drawings are very constant after 1835, the difference between the ISN and the Schwabe record may be due to calibration issues of the ISN before 1849 (Leussu *et al.*, 2013).

In an attempt to assess the correlation of the umbral areas with the group sunspot number, we plot averages of 100 daily all-disk umbral areas versus the corresponding group sunspot number of the same days in the bottom panel of Fig. 2.8. The same was done for the Greenwich photoheliographic database which contains umbral areas until 1976. The graph is similar to that by Balmaceda *et al.* (2009) who used the total spot areas instead. There is an intrinsic scatter in the correlation because of a certain randomness if both the sunspot number and sunspot areas are related to an internal magnetic field, rather than to each other. The uncertainty from the randomness has been reduced to about 10% by averaging over 100 days. Although the scatter in total umbral areas is higher than that due to randomness (as seen in the bottom panel of Fig. 2.8), it is comparable to the results from the Greenwich data, except for a slight tendency to larger areas (lines of linear fits through the origin were added for clarity in Fig. 2.8). We therefore conclude that the areas inferred from the Schwabe data are compatible with the Greenwich data, which did not enter our calibration at any step. The Schwabe areas do show, however, cycle-to-cycle variations in the strength of the correlation with the sunspot number indices.

The final total numbers of groups as well as the numbers of groups that have tilt angles (see Sect. 2.3) are listed in Table 2.2.

²The GSN includes a scaling of 12.08 derived from the comparison of the ISN with the groups found in the Greenwich Photoheliographic Database (Hoyt and Schatten, 1998). Since the ISN was scaled down to match Wolf’s observations, who recorded about 60% of the sunspots that would be reported today, the SSN from Schwabe’s data can actually lie above the GSN. This is the case when Schwabe’s drawings are bit more detailed than Wolf’s reports.

2.3 Tilt angles of groups

2.3.1 Determination of tilt and separation

The tilt angle of a given sunspot group is calculated in a plane tangential to the solar surface in an estimated mid-point of that particular group to avoid problems with the curvilinear heliographic coordinates. The mid-point of the group (hereafter box centre as opposed to the area-weighted centre of gravity of the group) is obtained using the easternmost and westernmost spots as well as the northernmost and southernmost spots of a given group. The longitude and latitude of the box centre is set to be the contact point of the tangential plane with the solar surface. The Cartesian coordinates in this plane are x_i and y_i for the i -th spot and x_g and y_g for the box centre and are normalised with respect to the solar diameter.

The algorithm then checks for the number of spots in a group. If this number is equal to two, the algorithm proceeds to calculate the tilt angle and polarity separation directly. If this number is more than two spots, we have to assess the most probable configuration of which spots belong to which polarity, since magnetic information is not available. We look for the most probable division of the group into two clusters by finding the least positional variance within the individual clusters. To accomplish this, we let a division line, running through the box centre, rotate from $\theta = 0$ to $\theta = 180^\circ$ and obtain, for each angle, a cluster of supposedly leading spots and a cluster of supposedly following spots. This is achieved using a vector perpendicular to the division line, $\mathbf{D} = (\cos \theta, \sin \theta)$. The sign of the inner product of this vector with the spot vector, $\mathbf{S}_i = (x_i - x_g, y_i - y_g)$ defines the cluster (‘polarity’) membership of the i -th spot. The sum of the two variances of the spots’ coordinates on either side of the division line is calculated. We denote the angle at which the least positional variance is achieved by θ_{opt} and adopt it as the most probable division of the sunspot group into polarities. The area-weighted centres of the polarities found are then calculated. The eastern and western parts correspond to the following and leading polarities, respectively, and their coordinate pairs are denoted by (x_F, y_F) and (x_L, y_L) . The coordinate pairs convert to heliographic coordinates (ϕ_F, λ_F) and (ϕ_L, λ_L) , respectively.

The tilt angle α is computed by

$$\tan \alpha = \begin{cases} (y_F - y_L) / (x_L - x_F) & \text{if } \lambda_g \geq 0 \\ (y_L - y_F) / (x_L - x_F) & \text{otherwise,} \end{cases} \quad (2.4)$$

where λ_g is the heliographic latitude of the box centre. The tilt angles are positive if the leading polarity is nearer to the equator. We emphasise that these operations are done in a tangential plane through the box centre. Problems with measuring on a spherical surface are thus very small. The tilt angles calculated are called pseudo-tilt-angle as in case of the Mt. Wilson data because magnetic polarity information is not available (Howard, 1991).

The polarity separation is then computed on the great circle (orthodrome) through the two polarities:

$$\cos \Delta\beta = \sin \lambda_F \sin \lambda_L + \cos \lambda_F \cos \lambda_L \cos(\phi_F - \phi_L). \quad (2.5)$$

The tilt angles are calculated for all spot groups with two or more spots.

2.3.2 Sources of errors

Differences between various data sources and tilt angle determinations may have the following origins:

- unipolar groups are assigned a tilt angle erroneously;
- the method of computation may introduce a bias if the division angle through the bipolar group is presumed or prejudiced;

- ambiguity of the tilt angle sign due to the lack of magnetic information;
- or incorrect splittings or combinations of groups lead to spurious tilt angles.

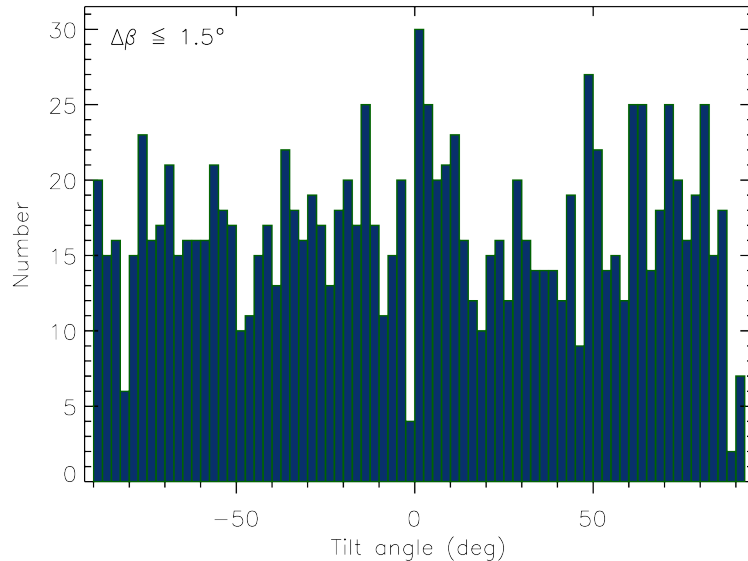


Figure 2.9: Histogram of spurious tilt angles of supposedly unipolar groups in the Schwabe data selected by a maximum polarity separation of $\Delta\beta \leq 1.5^\circ$.

The misidentification of unipolar regions generates a noise component whose distribution is much shallower than the distribution from bipolar groups (Wang *et al.*, 2015; Baranyi, 2015). The peak-to-tail ratio apparent from Fig. 8 in Wang *et al.* (2015) is about six for unipolar groups with $\Delta\beta < 2.5^\circ$, while it is roughly 100 for the groups with $\Delta\beta > 2.5^\circ$. In the Schwabe data, we find a peak-to-tail ratio of a bit more than two for $\Delta\beta < 2.5^\circ$, while it is entirely uniform for $\Delta\beta \leq 1.5^\circ$ (Fig. 2.9). An interesting exercise is the determination of the dependence of the average tilt angle on the level of noise that is typically introduced by unipolar sunspot groups, which are erroneously included when no magnetic information is available. We assume that the true tilt angle distribution is symmetric around its mean and denote it by $S(\alpha, \alpha_0, \sigma_\alpha)$, where α_0 and σ_α are the true average and width of that distribution, respectively. We add the noise as a simple background constant C , which mimics the contamination by unipolar groups or other spurious tilt angles to simplify the analysis, giving an upper limit of the error introduced by those tilt angles. The average tilt angle is then

$$\langle \alpha \rangle = \frac{\int_{-\pi/2}^{\pi/2} \alpha (C + S) d\alpha}{\int_{-\pi/2}^{\pi/2} (C + S) d\alpha}. \quad (2.6)$$

We can replace the constant C by the number of sunspot groups that contribute to C as a fraction of the total number of groups and denote this fraction by f . We find

$$C = \frac{f \int_{-\pi/2}^{\pi/2} S d\alpha}{\pi(1-f)}. \quad (2.7)$$

Inserting this into (2.6) leads to

$$\begin{aligned} \langle \alpha \rangle &= (1-f) \frac{\int_{-\pi/2}^{\pi/2} \alpha S d\alpha}{\int_{-\pi/2}^{\pi/2} S d\alpha} \\ &\approx (1-f) \alpha_0. \end{aligned} \quad (2.8)$$

The approximation coming from the finite-limit integral is better than 0.05° up to $\alpha_0 = 42^\circ$ for $\sigma_\alpha = 20^\circ$ and up to 15° for $\sigma_\alpha = 30^\circ$, which is good enough for any relevant average tilt angles.

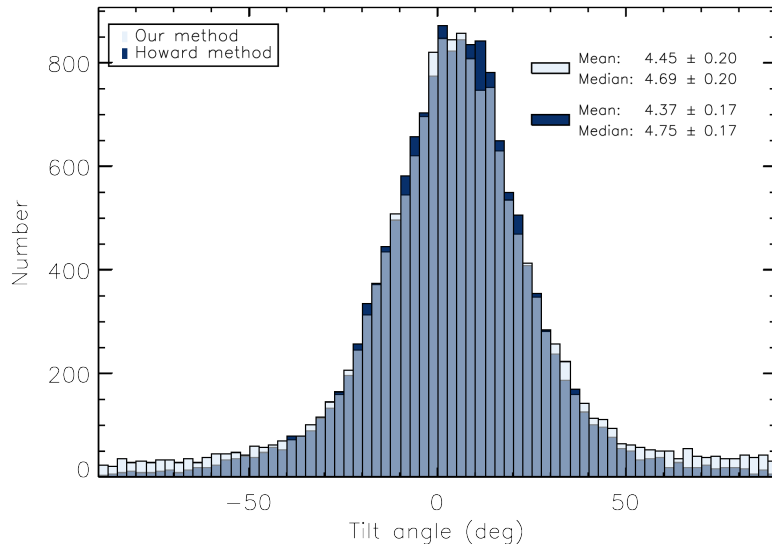


Figure 2.10: Histograms of the tilt angles in the Schwabe data, analysed with two different methods. Light bars show the excess of tilt angles from our isotropic method searching for the optimum polarity division, while dark bars show the excess of tilt angles from the method by Howard (1991). Only groups with area weighted centres within $\pm 60^\circ$ CMD and polarity separations $\Delta\beta > 3^\circ$ are used.

The relation (2.8) tells us that if 10% of the individual tilt angles are spurious, the average tilt angle reduces by 10%, e.g. from a true value of 5° to a measured value of 4.5° . Looking at the cycle-to-cycle variations derived by Wang *et al.* (2015) for individual data sets, we infer cycle-to-cycle scatters (corrected by t -distribution) of 4%, 9%, and 14% for the Debrecen umbral-based tilt angles, the Debrecen whole-spot-based tilt angles, and the tilt angles from the Mt. Wilson white-light images, respectively. Since the cycle-to-cycle variations of the average tilt angles are that small, the possible contamination of the distribution should be assessed, especially when data from different sources are combined. A noise level of 100% naturally leads to an average tilt angle of 0° (without polarity information). The influence of unipolar groups can be reduced significantly by excluding all groups with apparent separations of $\Delta\beta < 2.5^\circ$ or even $\Delta\beta < 3^\circ$ (Baranyi, 2015).

We tried to further reduce the influence of spurious tilt angles by looking at the scatter of tilt angles of a given group during its evolution over several days. We denote the individual appearances of a group over several days as “instances”. A similar procedure was proposed by Li and Ulrich (2012). On the one hand, outliers due to ill-defined groups need to be removed. On the other hand, groups become unipolar at the end of their lifetime, but are still large and accompanied by pores, mimicking $\Delta\beta > 3^\circ$. We therefore determine the median tilt angle $\bar{\alpha}$ from the various instances of a given group and determine the average deviation from it by

$$\Delta\alpha = \sum_{i=1}^I |\alpha_i - \bar{\alpha}|/I, \quad (2.9)$$

where I is the number of instances of the group and α_i are the tilt angles of the individual instances of the group. The tilt angle is fairly reliable if the polarity separation is large. We therefore tested whether the tilt angle at maximum polarity separation, $\alpha_{\max\text{sep}}$, does not deviate from the median significantly, using the criterion $|\alpha_{\max\text{sep}} - \bar{\alpha}| < \Delta\alpha$. The groups fulfilling this criterion are a good guess of the real bipolar groups, while others are omitted entirely. Now, within the accepted groups, all instances with $|\alpha_i - \bar{\alpha}| > 2\Delta\alpha$ are omitted as outliers. A group turning unipolar near the end of its lifetime still exhibits scattered spots and pores around the remaining (large-area) polarity which causes spurious tilt-angles with rapid changes. Those (mostly H-type) groups are not supposed to deliver a tilt angle. We call those cases evolutionary outliers in the following.

The removal of evolutionary outliers also requires the decision on which hemisphere a given group lay, since low-latitude groups may have instances on both sides of the equator, leading to jumps in the tilt angle. We decided upon the hemispheric membership by the average (signed) latitude of the group instances of each group. The signs of the tilt angles of all instances are then computed assuming the single hemisphere obtained from that average latitude, regardless of the actual hemisphere of an individual instance.

With respect to the method of computing tilt angles, we used the Schwabe data set to compare the method by Howard, Gilman, and Gilman (1984) with our method. The former always divides groups with a north–south line leading to a bias with an avoidance of tilt angles near 90° . Our method of trying all possible dividing lines is isotropic with equal prior probabilities for tilt angles of 90° , 0° , and -90° . Figure 2.10 shows a comparison of the two methods based on the Schwabe data of individual spots. The method of Howard (1991) tends to concentrate tilt angles at lower values.

Groups that are reversed dipoles as compared to the typical polarity of a given cycle (anti-Hale groups) cannot be detected in white-light images or sunspot drawings. The anti-Hale fraction of all groups is about 8% (Li and Ulrich, 2012; McClintock, Norton, and Li, 2014) or about 5% (Sokoloff and Khlystova, 2010) or even lower (Sokoloff, Khlystova, and Abramenko, 2015), based on magnetogram data. This fraction holds true for large bipolar regions though, while the fraction may be as high as 50% for ephemeral regions with areas less than 50 MSH (Illarionov, Tlatov, and Sokoloff, 2015), which are not relevant here as they are not accompanied by sunspots. In our cleanest distribution without evolutionary outliers, 95% of the groups are larger than 10 MSH in terms of their umbral group area. This translates to roughly 100 MSH total group area. For this lower limit of group areas, Illarionov, Tlatov, and Sokoloff (2015) give an anti-Hale fraction of about 37%, while for large groups with 500 MSH or more, that fraction is 10% or less. The unsigned tilt angle distribution of anti-Hale groups is broader than that of the Hale groups, but with similar peaks (McClintock, Norton, and Li, 2014). The influence of the missing knowledge of the polarity on the average tilt angle is therefore relatively mild and not as strong as a similar fraction of random noise in the data.

The exact definition of a group yields another source of possible errors. Baranyi (2015) revisited the Mt. Wilson and Kodaikanal data sets and compared them with Debrecen tilt angles. Among other things, she found that the automated routine used in the original analysis of the Mt. Wilson and Kodaikanal data often splits true groups into two smaller groups. While the average tilt angle by Howard (1991) ($4.2^\circ \pm 0.2^\circ$) was reproduced as $4.16^\circ \pm 0.19^\circ$, a higher value of $4.69^\circ \pm 0.20^\circ$ was found for 1917–1976 when these extra splittings were corrected. In terms of Eq. 2.9, this new value indicates a random noise fraction in the original value of 11%. That period of 1917–1976 is the one for which the Greenwich Photoheliographic Database was used as a reference to define proper groups. For 1974–1985, the Debrecen Photoheliographic Database was used to obtain cleaner groups, to give the average of $5.00^\circ \pm 0.47^\circ$. The difference between this value and $4.69^\circ \pm 0.20^\circ$ may actually be real and due to the different cycles covered.

2.3.3 Distribution and averages

Figure 2.11 shows the resulting distribution of tilt angles. While the distribution is quite broad, it has its maximum at small, non-zero α . The open bars may include tilt angles, which are erroneously computed for two or more spots of a single polarity, fragmented spots, and spots inside the same penumbra. The filled histogram therefore shows the distribution of tilt angles with polarity separations $\Delta\beta > 3^\circ$. In this distribution, spots inside a common penumbra are essentially excluded, but, on the one hand, true bipolar groups with very small polarity separations may also be excluded. On the other hand, spurious tilt angles due to a decaying big group with a single polarity may still contribute to this distribution, but are a very minor fraction (Baranyi, 2015). The selection of bipolar groups may perhaps be fine-tuned using an

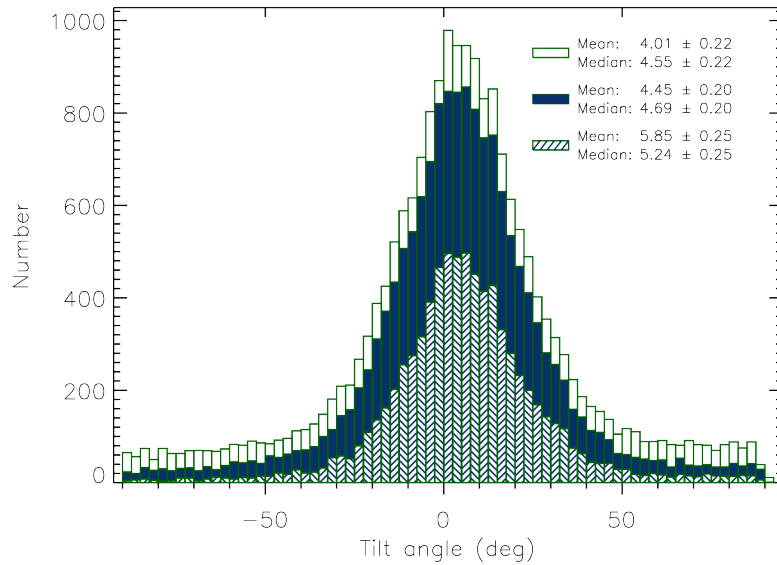


Figure 2.11: Histograms of the tilt angles of groups with area weighted centres within 60° central meridian distance. *Open bars:* entire set, *filled bars:* groups with a minimum polarity separation of $\Delta\beta_{\min} = 3^\circ$, and *hatched bars:* groups with $\Delta\beta_{\min} = 3^\circ$ and a removal of evolutionary outliers that occur in the sequence of tilt angles during the evolution of any given group. This hatched histogram is an attempt to further reduce the influence of occasional unipolar instances of otherwise bipolar groups. See text for the detailed algorithm. The bin width is 2.5° .

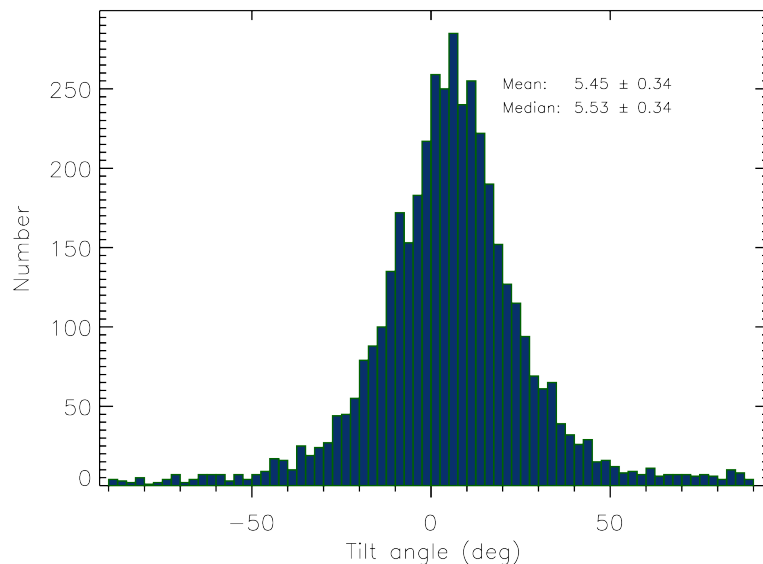


Figure 2.12: Tilt angle histogram of the Schwabe data for group centres within 60° central meridian distance and polarity separations $\Delta\beta > 3^\circ$. In this analysis, only spots with umbral areas of 5 MSH or more were used to compute the weighted positions of the polarities. The selection therefore affects both tilt angles and polarity separations. As compared with the hatched bars in Fig. 2.11, many groups have now turned into unipolar groups, since one of the polarities was represented by a single spot of less than 5 MSH.

Table 2.3: Modified format of the data of individual sunspots observed by Samuel Heinrich Schwabe.

Field	Column	Format	Explanation
YYYY	1–4	I4	Year
MM	6–7	I2	Month
DD	9–10	I2	Day referring to the German civil calendar running from midnight to midnight
HH	12–13	I2	Hour, times are mean local time in Dessau, Germany
MI	15–16	I2	Minute, typically accurate to 15 minutes
T	18	I1	Indicates how accurate the time is. Timeflag = 0 means the time has been inferred by the measurer (in most cases to be 12h local time); Timeflag = 1 means the time is as given by the observer
LO	20–24	F5.1	Heliographic longitude of apparent disk centre seen from Dessau
BO	26–30	F5.1	Heliographic latitude of apparent disk centre seen from Dessau
CMD	32–36	F5.1	Central meridian distance, difference in longitude from disk centre; contains –.– if line indicates spotless day; contains NaN if position of spot could not be measured.
LLL.L	38–42	F5.1	Heliographic longitude in the Carrington rotation frame; contains –.– if line indicates spotless day; contains NaN if position of spot could not be measured.
BBB.B	44–48	F5.1	Heliographic latitude, southern latitudes are negative; contains –.– if line indicates spotless day; contains NaN if position of spot could not be measured.
M	50	C1	Method of determining the orientation. ‘C’: horizontal pencil line parallel to celestial equator; ‘H’: book aligned with azimuth-elevation; ‘Q’: rotational matching with other drawings (spot used for the matching have ModelLong \neq ‘–.–’, ModelLat \neq ‘–.–’, and Sigma \neq ‘–.–’).
Q	52	I1	Subjective quality, all observations with coordinate system drawn by Schwabe get Quality = 1. Positions derived from rotational matching may also obtain Quality = 2 or 3, if the probability distributions fixing the position angle of the drawing were not very sharp, or broad and asymmetric, respectively. Spotless days have Quality = 0; spots for which no position could be derived, but have sizes, get Quality = 4.
SS	54–55	I2	Size estimate in 12 classes running from 1 to 12; a spotless day is indicated with 0
GROUP	57–64	C8	Group designation based on Schwabe, but modified by our regrouping
MEASURER	66–75	C10	Last name of person who obtained position
MOD_L	77–81	F5.1	Model longitude from rotational matching (only spots used for matching have this)
MOD_B	83–87	F5.1	Model latitude from rotational matching (only spots used for matching have this)
SIGMA	89–93	F6.3	Total residual of model positions compared with measurements of reference spots in rotational matching (only spots used for the matching have this). Holds for entire day.
DELTA	96–99	F4.1	Heliocentric angle between the spot and the apparent disk centre in degrees (disk-centre distance); it is –.– for spotless days, while it is NaN if the spot position could not be determined.
UMB	100–103	I3	Inferred umbral area in millionths of the solar hemisphere (MSH); it is 0 for spotless days and NaN if spot position could not be derived or DELTA > 85°
A	105	C1	Flag saying whether area mapping is based on umbral (‘U’) or penumbral (‘!’) areas with the latter being less certain. The actual area given in UMB is always umbral. Spotless days have –.

Notes. The format extends that by [Arlt et al. \(2013\)](#) after Col. 93. In the Format column, I denotes integer fields, C8 is an 8-character text field, and, e.g. F5.1 denotes a 5-character-wide floating point field with one decimal. Areas in UMB are based on the derivation by [\(2.2\)](#).

area-dependent minimum polarity separation, but we did not wish to impose biases that may affect the distribution of polarity separations. A constant minimum separation $\Delta\beta_{\min}$ is therefore used for selecting actual bipolar groups.

The average tilt angle for the distribution with $\Delta\beta_{\min} = 3^\circ$ and with area weighted group centres within $\pm 60^\circ$ CMD is $4.45^\circ \pm 0.20^\circ$ (median $4.69^\circ \pm 0.20^\circ$) where the error of the mean

Table 2.4: Format for the tilt angle data derived from the sunspot groups observed by Schwabe, with format symbols as in Table 2.3.

Field	Column	Format	Explanation
YYYY	1–4	I4	Year
MM	6–7	I2	Month
DD	9–10	I2	Day
HH	12–13	I2	Hour
MI	15–16	I2	Minute; mean local time in Dessau, Germany
GROUP	18–25	C8	Group name based on Schwabe, but modified by our regrouping
SP	27–28	I2	Number of spots in a group
ARA	30–32	I3	Sum of umbral area of all spots in a group, in millionths of the solar hemisphere (MSH)
AWL.L	34–38	F5.1	Area-weighted heliographic longitude of the group
AWB.B	40–44	F5.1	Area-weighted heliographic latitude of the group
TILTAN	46–51	F6.2	Tilt angle of the group; positive sign means leading polarity closer to equator in either hemisphere. This tilt angle was found using an isotropic search for the most likely dividing line between the polarities.
TILTTHO	53–58	F6.2	Tilt angle computed as in Howard (1991) for compatibility reasons. It is based on a fixed vertical dividing line between the polarities and an approximative formula for the tilt angle.
POLSP	60–64	F5.2	Polarity separation of the group in degrees on the solar sphere. This and the following items are based on the polarity definition for TILTAN.
FN	66–67	I2	Number of spots in the following polarity
LN	69–70	I2	Number of spots in the leading polarity
FAR	72–74	I3	Umbral area of the following polarity, in MSH
LAR	76–78	I3	Umbral area of the leading polarity, in MSH
FLL.L	80–84	F5.1	Area-weighted longitude of the following polarity
FBB.B	86–90	F5.1	Area-weighted latitude of the following polarity
LLL.L	92–96	F5.1	Area-weighted longitude of the leading polarity
LBB.B	98–102	F5.1	Area-weighted latitude of the leading polarity
GFC	104–108	F5.1	Heliocentric distance of the group from the disk centre in degrees

Notes. All areas are based on the UMB column in Table 2.3.

is computed by the standard deviation of the distribution divided by the square root of the number of points, $\sigma_{\text{tilt}}/\sqrt{n}$. For comparison, we may also compute the average tilt angle for $\Delta\beta_{\text{min}} = 0$ (again $|\text{CMD}| < 60^\circ$) and obtain $4.01^\circ \pm 0.22^\circ$ (median $4.55^\circ \pm 0.22^\circ$). The lower value is consistent with our earlier supposition that spurious bipolarities add a certain amount of randomness to the data, bringing the average closer to zero. This average agrees relatively well with those found by Howard (1991) ($4.2^\circ \pm 0.2^\circ$) and Dasi-Espuig *et al.* (2010) ($4.25^\circ \pm 0.18^\circ$ for Mt. Wilson and $4.51^\circ \pm 0.18^\circ$ for Kodaikanal) for solar cycles 15–21, which were all computed without a lower limit, i.e. $\Delta\beta_{\text{min}} = 0$.

An analysis of the Debrecen data by Baranyi (2015) with careful extraction of truly bipolar groups delivered $5.12^\circ \pm 0.46^\circ$ for 1974–1985 (end of cycle 20 and cycle 21). Based on a minimum polarity separation of $\Delta\beta_{\text{min}} = 3^\circ$, we recomputed the Mt. Wilson and Kodaikanal averages as well which resulted in values of $5.95^\circ \pm 0.42^\circ$ and $6.91^\circ \pm 0.45^\circ$, respectively, for cycle 21. Ivanov (2012) used the Pulkovo database (Catalogue of Solar Activity; CSA) for tilt angles in the period 1948–1991. We used their database and obtained an average tilt angle of $6.41^\circ \pm 0.14^\circ$ for cycle 21 only. In this sample, the groups were determined manually and contain a fairly clean definition of what a group is, similar to our analysis of the Schwabe drawings. Since the average tilt angle varies from one cycle to the next, we cannot compare Schwabe’s tilt angles with those from the 20th century directly, but we find that averages of clean tilt angle samples are typically 5° or larger.

The resulting histogram of tilt angles with deleted evolutionary outliers (Sect. 2.3.2) is shown in Fig. 2.11 as hatched bars. The average tilt angle has risen to $5.85^\circ \pm 0.25^\circ$, based on 7765 tilt angles. We consider this the cleanest sample of tilt angles for cycles 7–10. The only average this value can be compared with now (as far as different cycles can be compared at all) is that given

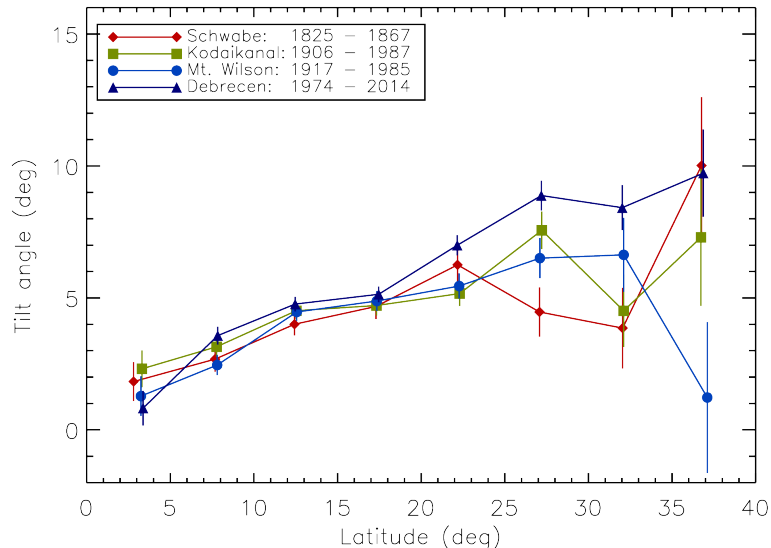


Figure 2.13: Dependence of the average tilt angle on the unsigned latitude for the data from Schwabe, Kodaikanal, Mt. Wilson, and Debrecen. We only use groups with central meridian distances within $\pm 60^\circ$ as the simplest common filter for all data sets. Errors of the means are the standard deviation of the bin sample divided by \sqrt{n} in each bin.

by Baranyi (2015) where bipolar groups have also been selected fairly rigorously. However, that Debrecen tilt angle of 5.12° is different in that spots smaller than 5 MSH are considered pores that do not enter the determination of tilt angles and polarity separations. Figure 2.12 shows the histogram of the tilt angles restricted to spots that have areas ≥ 5 MSH. The average of $5.45^\circ \pm 0.34^\circ$ (based on 4154 tilt angles) is slightly lower than the above value of $5.85^\circ \pm 0.25^\circ$, but not significantly. Even though the pores seem to play a minor role in determining reliable tilt angles, the difference shows that the minimum umbral area needs to be considered when combining several data sets.

The average dependence of the tilt angle on the absolute heliographic latitude (Joy’s law) is shown in Fig. 2.13. Together with the Schwabe data, we also plotted the average tilt angles obtained from the Mt. Wilson, Kodaikanal, and Debrecen data, using only tilt angles from groups within $\pm 60^\circ$ CMD. The latitudinal dependence in the Schwabe data may be a bit shallower than the dependencies determined from the other data sets, especially since it exhibits a non-zero intersection with the ordinate. However, the latitudinal dependence is in agreement with them considering the uncertainty margins.

The format of the database containing the individual umbrae including umbral areas as well as spotless days is given in Table 2.3, which extends the format given by Arlt *et al.* (2013), while the format of the final data set containing the tilt angles and polarity separations of sunspot groups is given in Table 2.4. We give both the tilt angles obtained according to our method described above as well as the tilt angles derived with the method by Howard (1991) in Table 2.4.

2.4 Summary

This study aims to determine physical areas of sunspots from drawings by Samuel Heinrich Schwabe in 1825–1867 as well as ordering these sunspots into (hopefully bipolar) groups and computing tilt angles of these sunspot groups for that period. The fraction of the solar disk covered by the pencil dots in the drawings cannot be directly converted into an area in km² or millionths of a solar hemisphere (MSH). We therefore constructed a mapping of the 12 arbitrary cursor sizes that were used by Arlt *et al.* (2013) to estimate the sizes of sunspots in the Schwabe drawings. For cycles 8–10, we obtain an average umbral area per day of 113. The Debrecen data for cycles 21–23, which were predominantly used for calibration, yield an average of roughly 150. The difference appears to be compatible with the stronger cycles in the second half of the 20th century and because Schwabe may have overlooked (or not plotted) a number of small spots. The umbral areas in the Greenwich Photoheliographic Database lead to an average of about 140 from cycles 12–20 of mixed strengths. Our area conversion is independent of the Greenwich data, but seems to agree with it fairly well, again taking into account that the Schwabe drawings may miss a few smaller spots.

The area distribution of the Schwabe sunspots exhibits a log-normal distribution in agreement with 20th century data (Bogdan *et al.*, 1988) and is essentially independent of the cycle phase. Schwabe’s original sunspot group designations were modified so that the groups comply with the modern understanding of a sunspot group, with the limitation of missing magnetic information. The tilt angles, as well as the polarity separations of the sunspot groups, were calculated using the positions and areas of all individual sunspots. Without the magnetic information, the definition of the polarities may lead to wrong associations affecting both tilt angles and polarity separations. The manual inspection of the groups before computing these quantities reduces these incorrect polarities as compared to fully automatic analysis schemes. Nevertheless, a remaining random component in the tilt angle distribution is likely to be present.

Both an updated sunspot database and a tilt angle database³ are available for further study. In the sunspot database, we find:

1. sunspot areas for spots with $\text{CMD} \leq 70^\circ$ are reliable;
2. sunspot areas for spots with $70^\circ < \text{CMD} \leq 85^\circ$ are uncertain because they are an extrapolation of the statistical method employed;
3. sunspot areas for spots with $\text{CMD} > 85^\circ$ have been omitted; and
4. sunspot areas are calibrated using 20th century data; they do not serve for the purpose of detecting differences in areas between the 19th and the 20th century.

In the tilt angle database, we find:

1. tilt angles for all groups with two or more spots are reported;
2. tilt angles for groups with $\text{CMD} \leq 60^\circ$ are considered reliable as the positions are reliable;
3. tilt angles for polarity separations $\Delta\beta > 3^\circ$ (POLSP) are likely to be bipolar groups and should be selected for further analysis; and
4. the influence of spurious tilt angles from remaining unipolar groups can be further reduced by removing outliers from the sequence of tilt angles provided by the evolution of a given group. In brief, we removed days of appearance of a given group if the obtained tilt angle deviates significantly from the mean tilt angle of all appearances of that single group. The actual procedure is a bit more involved and is described in Sect. 2.3.2.

³Available at <http://www.aip.de/Members/rarlt/sunspots> and at the Centre de Données astronomiques de Strasbourg (CDS).

Joy's law was found to be obeyed by the likely bipolar groups. The latitude dependence averages over all Schwabe cycles is not significantly different from cycles in the 20th century.

The applicability of white-light images for inferring cycle properties was doubted by Wang *et al.* (2015), mostly because of the inevitable contamination by actual unipolar groups. We believe the white-light images and drawings can still be useful because (a) improved algorithms and visual inspection can reduce the impact of unipolar groups significantly, and (b) we are interested in relative variations of tilt angles from one cycle to another, so consistently analysed sunspot data can still provide useful relative information of cycle-to-cycle variability. Care has to be taken that all data used for a particular study are consistent with each other, e.g. tilt angles from white-light images and magnetograms cannot be combined directly into a single record.

We have not studied the tilt angles of the individual cycles⁴. This will be the subject of a future study of tilt angles and strengths of individual cycles as well as correlations thereof, extending earlier works on Mt. Wilson and Kodaikanal data. Cycle 7 is an especially interesting candidate to look for peculiarities, since it occurred shortly after the Dalton minimum (roughly 1795–1820). This paper aims to disseminate the areas and tilt angles as the basis for further studies.

⁴This was carried out later and presented in Chpt. 3.

Chapter 3

Sunspot group tilt angle measurements from historical observations

V. Senthamizh Pawai, R. Arlt, A. Diercke, C. Denker, and J. M. Vaquero

Adv. Space Res. 58, 1468. Accepted 1 March 2016

The long-term study of solar cycle properties using historical observations has provided mainly the sunspot number (Clette *et al.*, 2014). However, we can also access other properties more directly related to the solar dynamo through historical sunspot drawings. The tilt angle of sunspot groups is among those parameters and can be included in certain types of dynamo models. Bipolar sunspot groups exhibit an axis through the two main magnetic polarities. The tilt angle is the angle at which this axis is orientated with respect to the solar equator. It is an important property in flux-transport dynamos (Babcock-Leighton dynamos, see e.g. Charbonneau, 2010, Sect. 4.8) in which it provides the source term for the poloidal magnetic field which in turn correlates with the strength of the next cycle. The tilt angles are widely believed to be the result of buoyantly unstable magnetic flux tubes at the bottom of the convection zone, rising under the influence of rotation, internal twist, and magnetic tension.

According to results of the thin flux tube approximation, tilt angles are either due to writhing of rising flux loops by the Coriolis force or the pitch angle of the subsurface field wound up by the differential rotation (D’Silva and Choudhuri, 1993). The combination of magnetic buoyancy and the Coriolis force generates the correct latitudinal distribution of tilt angles, according to numerical simulations in the thin flux tube framework (e.g. D’Silva and Choudhuri, 1993; Caligari, Moreno-Insertis, and Schüssler, 1995; Fan and Fisher, 1996; Weber, Fan, and Miesch, 2013). These computations can also reproduce the correlation between the magnetic field strength and the tilt angle which is seen in some observational studies (Tian, Liu, and Wang, 2003; Dasi-Espuig *et al.*, 2010). The average tilt angle and the amplitude of the corresponding cycle appears to be anti-correlated, while the product of the average tilt angle with the cycle amplitude is well correlated with the strength of the following cycle (Dasi-Espuig *et al.*, 2010, 2013).

In thin flux tube models, the tilt angles are even useful in constraining the strength of initial magnetic flux. The strength of the toroidal magnetic field at the bottom of the convection zone has to be in the range of 40–50 kG in order to obey the observed Joy’s law (Weber, Fan, and Miesch, 2011).

Observational studies by Kosovichev and Stenflo (2008) show that the tilt angles of sunspot groups change gradually over their lifetime except in the beginning of emergence. While the tilt angles are random in the earliest phase of emergence, they adjust towards Joy’s law during the rest of the emergence phase, i.e. as long as the magnetic flux is growing. It is not straight-forward

to draw a direct link between the tilt angles and the emergence of flux tubes in simulations. The average tilt angles are also fairly independent of the cycle phase within fixed latitudinal zones (Li and Ulrich, 2012).

The study of tilt angles derived for several centuries helps us understand their origin and their relation to the solar cycle. The true tilt angles of sunspot groups are available only from magnetic data of the solar surface for the second half of the 20th century, while pseudo-tilt angles are measured without the polarity information and have a 180° ambiguity. Pseudo-tilt angles can be computed whenever individual spot positions in sunspot groups are available from drawings or images. They have recently been calculated for the period of 1825–1867 using the sunspots observations by Schwabe (Senthamizh Pavai *et al.*, 2015)¹.

In this paper, we present the tilt angle measurements from further historical sunspot observations, namely the observations by Christoph Scheiner (1618, 1621–1622, 1625–1627), Johannes Hevelius (1642–1644), Johann Caspar Staudacher (1749–1796), Ludovico Zucconi (1754–1760), and Gustav Spörer (1861–1894).

The details of different solar observations and the methods used in data extraction from those sunspot drawings are described in Sect. 3.1. The comparison of mean tilt angles and cycle-mean tilt angles from various data are discussed in Sect. 3.2.

3.1 Data set

Christoph Scheiner started his sunspot observations from Ingolstadt, Germany, in the early 17th century. His first known sunspot drawing was made on 21 October 1611. Most of his data, however, were recorded from Rome. He published observations only for a few days during each of the years of 1611, 1612, 1618, 1621, 1622, and 1624. In the period 1625–1627, the observations are fairly continuous (drawings covering 342 days in 1625, 163 days in 1626, and 55 days in January–June 1627)². His drawings show the sunspot groups traversing the solar disk in a single full-disk drawing (Scheiner, 1630). The positions and areas of the sunspots were measured using 13 circular cursor shapes with areas between one and 364 pixels. The data before 1618 were not included in the tilt angle distribution, because they are extremely coarse and show highly exaggerated sizes of sunspot groups.

Johannes Hevelius recorded his observations of the Sun from Gdańsk, Poland, during the period of 1642–1644 (15 days in October–December 1642, 110 days in May–December 1643, and 98 days in January–October 1644). These sunspot drawings were published by Hevelius in an appendix of his book *Selenographia* (Hevelius, 1647). His drawing style is very similar to Scheiner’s style, and the positions and area information were obtained in the same way. It is important to note that these sunspot drawings were made just before the Maunder Minimum, a period of reduced solar activity from 1645 to 1715 approximately (Spörer, 1889b; Usoskin *et al.*, 2015).

During the second half of the 18th century Johann Caspar Staudacher (or Staudach) recorded his observations of the Sun from Nuremberg, Germany, and made drawings in 1749–1796. Detailed information about the drawings and the data extraction methods can be found in Arlt (2008) and Arlt (2009). Various methods of estimating the orientation of the drawings had to be employed to measure the sunspot positions. From the data base derived, we use only the spots with quality flags 1 and 2. This basically excludes drawings for which the orientation was estimated using a typical tilt angle for bipolar regions. Quality-3 observations use the tilt as an input in many cases and are therefore not used.

¹Chpt. 2.

²The sunspot data used in this chapter were extracted from the drawings provided in Scheiner (1630). The data used in Chpt. 4 includes sunspot data also from the drawings available in Scheiner (1651), which was not known to us while writing the paper presented in the current chapter. Hence, the tilt angles differ very slightly in these two chapters.

For a rather short time from April 1754 to May 1758 and a short spell in June 1760, Ludovico Zucconi observed the Sun from Venice, Italy, contemporaneously with Staudacher. The positions and areas of individual sunspots were extracted by [Cristo, Vaquero, and Sánchez-Bajo \(2011\)](#) using the HSUNSPOTS tool. The orientation of these drawings were clearly marked by the observer, and we consider them fairly precise.

The drawings of sunspot observations made by Samuel Heinrich Schwabe from Dessau, Germany, in the period 1825–1867, and the extraction of data from them were explained in detail by [Arlt \(2011\)](#) and [Arlt *et al.* \(2013\)](#). A description of the method that was employed to compute all the tilt angles in the present paper is given by [Senthamizh Pavai *et al.* \(2015\)](#), where it was applied to the Schwabe data.

Friedrich Wilhelm Gustav Spörer observed sunspots from Anklam and Potsdam, Germany, during 1861–1894. He drew the sunspot groups while they crossed the central meridian, so the evolution of sunspot groups is not available. The details of the drawings and the technique used in the extraction of positions and areas of sunspots were given by [Diercke, Arlt, and Denker \(2015\)](#).

3.2 Tilt angle distributions

Based on the positions of the individual spots, a tangential plane is adopted touching the solar surface in the group center in order to minimize curvature effects in determining the tilt angle. The groups are divided into two polarities such that the variance of the spot positions in the individual polarities are lowest. The method is explained in detail in [Senthamizh Pavai *et al.* \(2015\)](#). The sign of the tilt angle is positive when the leading polarity is closer to the equator than the following polarity. There is no sign of the polarities available from the sunspot drawings. Therefore, groups not obeying Hale’s polarity law cannot be detected.

The definition of what forms a sunspot group varies among the various observers. We have therefore inspected all the data sets used here to re-group sunspots where it appeared necessary. We used the spot distributions as well as the evolution of the groups to discriminate them. The following numbers refer to groups through their full life-time as a single group, not to individual appearances of groups in each drawing. While the re-grouping for Schwabe is described in [Senthamizh Pavai *et al.* \(2015\)](#), a number of groups were split or combined in the records of the other observers as well. This procedure led to 13 new groups in Scheiner’s drawings, whereas in seven cases, groups were combined to one. In the drawings by Hevelius, we obtained five new groups and combined groups in three cases. Zucconi’s drawings contained two groups which needed to be split into two new groups each. Finally, 104 new groups were formed in Spörer’s data, while in 90 cases, two groups were combined to a single group. Since Staudacher did not provide any group designations, the association of spots to groups was made from scratch by inspection of the drawings.

Table 3.1: Mean and median tilt angles for various data sets. Full widths at half-maximum (FWHM) were derived from Gaussian fits to the tilt angle distributions.

Data source	Years	Mean tilt	Median tilt	FWHM	Number of groups
Scheiner	1618–1627	$3.92^\circ \pm 0.91^\circ$	$3.63^\circ \pm 0.91^\circ$	33.4°	537
Hevelius	1642–1644	$4.79^\circ \pm 1.43^\circ$	$5.35^\circ \pm 1.43^\circ$	27.1°	130
Staudacher	1749–1796	$2.03^\circ \pm 0.98^\circ$	$1.79^\circ \pm 0.98^\circ$	50.3°	828
Zucconi	1754–1760	$0.62^\circ \pm 2.28^\circ$	$-1.48^\circ \pm 2.28^\circ$	35.8°	131
Schwabe	1825–1867	$4.45^\circ \pm 0.20^\circ$	$4.69^\circ \pm 0.20^\circ$	40.6°	15548
Spörer	1861–1894	$4.86^\circ \pm 0.45^\circ$	$4.04^\circ \pm 0.45^\circ$	31.3°	2834

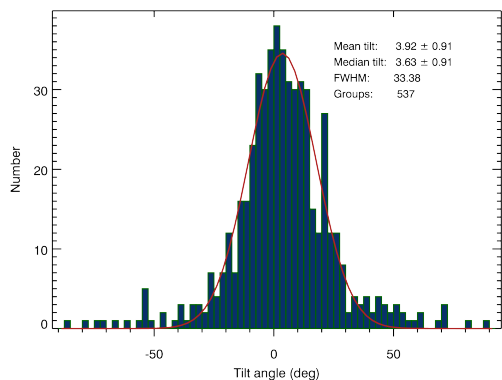


Figure 3.1: Histogram of the tilt angles of sunspot groups from the drawings by Scheiner. Only groups with area weighted centers within $\pm 60^\circ$ CMD are used. The FWHM was derived from a Gaussian fit (solid line).

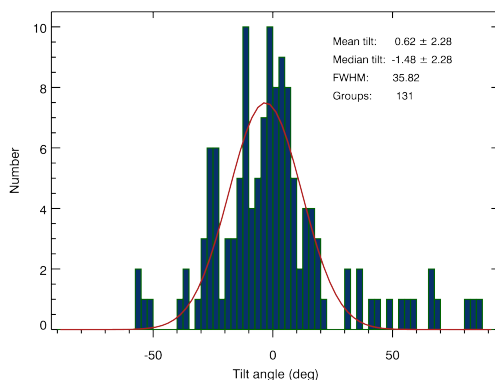


Figure 3.2: Tilt angle histogram for Zucconi. Only groups with area weighted centers within $\pm 60^\circ$ CMD are used.

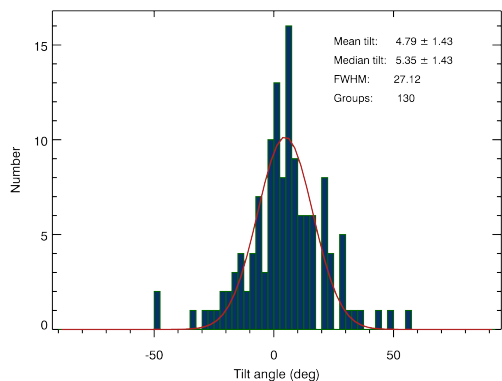


Figure 3.3: Tilt angle histogram for Hevelius. Only groups with area weighted centers within $\pm 60^\circ$ CMD are used.

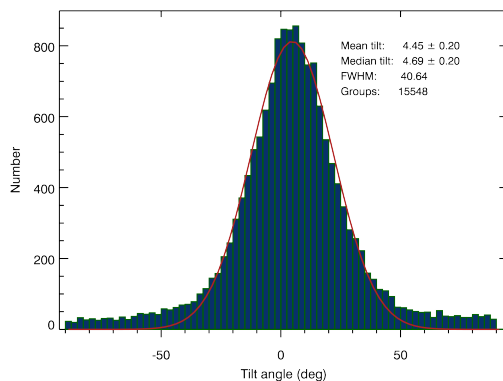


Figure 3.4: Tilt angle histogram for Schwabe. Only groups with area weighted centers within $\pm 60^\circ$ CMD and polarity separations $\Delta\beta > 3^\circ$ are used.

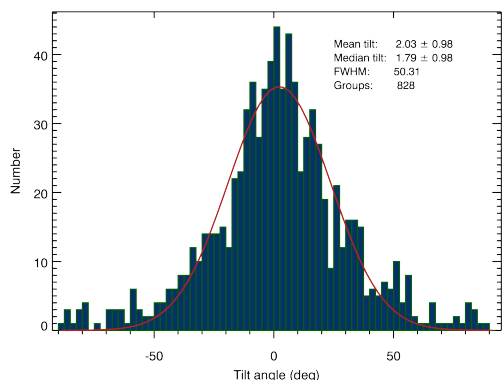


Figure 3.5: Tilt angle histogram for Staudacher. Only groups with area weighted centers within $\pm 60^\circ$ CMD, polarity separations $\Delta\beta > 3^\circ$, and with quality flags 1 and 2 are used.

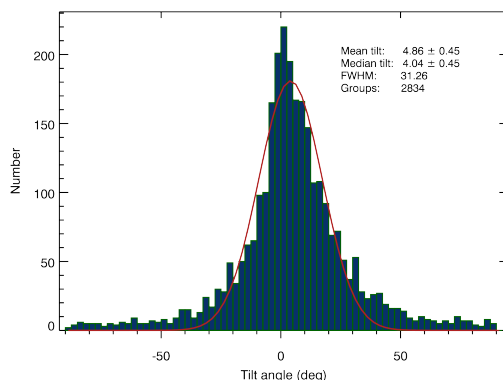


Figure 3.6: Tilt angle histogram for Spörer and groups with polarity separations $\Delta\beta > 3^\circ$. Only spots with areas ≥ 1 MSH were considered while calculating the tilt angle.

From those sunspot groups, the bipolar ones need to be extracted for the computation of tilt angles. The sunspot drawings of Scheiner, Hevelius, and Zucconi were manually inspected to select the bipolar groups, and only those groups are included in the present study. Figures 3.1, 3.3, and 3.2 show the distributions of tilt angles from the drawings of Scheiner, Hevelius, and Zucconi, respectively. In the distributions, only the bipolar groups within $\pm 60^\circ$ central meridian distance (CMD) are included, because the positional accuracy drops significantly beyond these limits. In all the graphs, we fit the discrete distributions with Gaussian functions to obtain estimates for the full widths at half-maximum (FWHM).

In case of Staudacher, Schwabe, and Spörer (Figs. 3.5, 3.4, and 3.6, respectively), the volumes of sunspot drawings were too large to manually pick the bipolar groups. For Staudacher and Schwabe, we complemented the condition of limiting the groups within $\pm 60^\circ$ CMD by a minimum polarity separation ($\Delta\beta$) of 3° (Baranyi, 2015) in order to statistically remove unipolar groups. Figure 3.6 shows the tilt angle distribution of sunspot groups from Spörer’s observations. Since the groups in Spörer’s drawings are already at central meridian, only the condition $\Delta\beta > 3^\circ$ was applied to remove potentially unipolar groups. The averages and medians of all the above tilt angle distributions are given in Table 3.1.

The FWHM for the tilt angle distributions are in the range of 30° – 40° , with one exceptional value of 50° for Staudacher. Wang *et al.* (2015) obtained an FWHM of 30.8° for the distribution of tilt angles from the Debrecen data using umbral data alone, as we do here as well.

The sizes of the sunspots in Staudacher’s drawings are highly exaggerated, so the area values were not used in the tilt angle calculation. Spörer magnified the sizes of sunspots in his drawings to some extent, and we needed to scale down the area values by a factor of 13.3 as inferred by Diercke, Arlt, and Denker (2015). Spörer recorded both pores and umbrae but other drawings only contain umbrae or umbrae and penumbrae. To make it consistent with other data, only umbrae with areas ≥ 1 MSH were considered while calculating the tilt angle.

3.2.1 Comparison of cycle-averaged tilt angles

The cycle-averaged tilt angle is a quantity related to the polar field generated by active regions in the course of a cycle and may be an indication of the activity of the future cycle. These averages are available since solar cycle 15 from modern data (e.g. Dasi-Espuig *et al.*, 2010; McClintock and Norton, 2013; Wang *et al.*, 2015). Since historical data provide tilt angles over a much longer period, we look at cycle-averaged tilt angle values from Staudacher, Schwabe, and Spörer data which cover the cycles 0–4 and 7–13. The data by Scheiner and Hevelius are not covering entire solar cycles. Their average may only be a rough indication of the cycle-average tilt angle and need to be treated with caution.

The Staudacher data covers solar cycles 0–4 without the beginning of cycle 0. Table 3.1 shows that the mean tilt in the Staudacher and Zucconi data are lower than the ones from other data sources. While Staudacher’s drawings are not very precise and could contain a strong random component bringing the average tilt angle close to zero, Zucconi’s data are precise enough and confirm the very low average tilt. The data by Zucconi cover the cycle minimum between solar cycles 0 and 1 (February 1755 according to Hathaway, 2010) showing spots at latitudes from 0° to 30° , apparently including spots from both the ceasing cycle 0 and the growing cycle 1.

The butterfly diagram from the Staudacher data for the solar cycles 0 and 1 also shows a peculiar behaviour with an excess of groups at the equator (Arlt, 2009). We therefore divide the Staudacher data into two parts, such that one part contains the cycles 0 and 1 and the other part contains the remaining data (cycles 2–4), instead of dividing the data into individual cycles. The data do not contain the beginning of the cycle 0 but together with cycle 1, we consider the result sufficiently representative for a two-cycle average. The mean tilt angles were found to be $1.03^\circ \pm 1.32^\circ$ for cycles 0 and 1 and $3.33^\circ \pm 1.47^\circ$ for cycles 2–4. Figure 3.7 shows the tilt

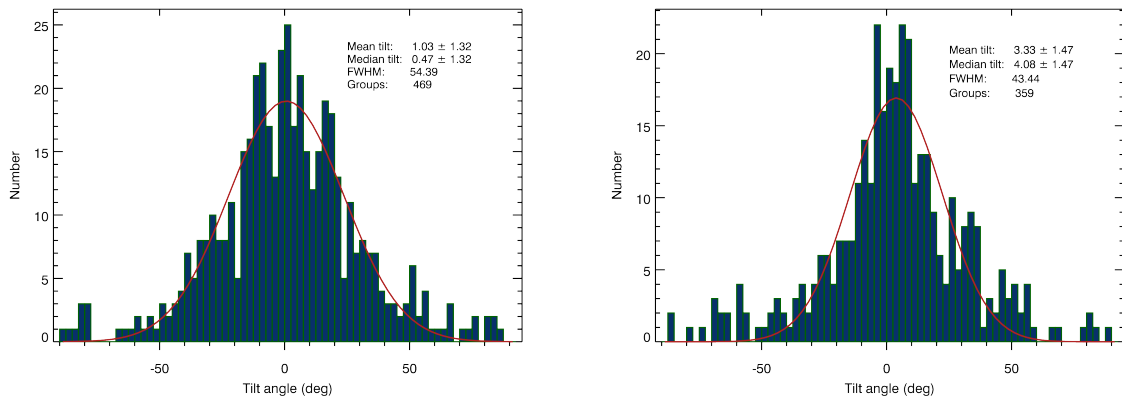


Figure 3.7: Tilt angle histograms for cycles 0 and 1 (left) and cycles 2, 3 and 4 (right) from Staudacher. Only groups with area weighted centers within $\pm 60^\circ$ CMD, polarity separations $\Delta\beta > 3^\circ$ and with quality flags 1 and 2 are used.

Table 3.2: Average and median tilt angles for individual solar cycles or small groups of cycles as well as the FWHM of the individual distributions. We use the cycle number notation of [Zolotova and Ponyavin \(2015\)](#). Parentheses indicate that the cycle was not fully covered by observations.

Data source	Cycle	Mean tilt	Median tilt	FWHM	Groups
Scheiner	-12 (first half)	$(3.92^\circ \pm 0.91^\circ)$	$(3.63^\circ \pm 0.91^\circ)$	(33.4°)	537
Hevelius	-10 (maximum)	$(4.79^\circ \pm 1.43^\circ)$	$(5.35^\circ \pm 1.43^\circ)$	(27.1°)	130
Zuconni	0+1 (min. between 0 and 1)	$(0.62^\circ \pm 2.28^\circ)$	$(-1.48^\circ \pm 2.28^\circ)$	(35.8°)	131
Staudacher	0+1	$1.03^\circ \pm 1.32^\circ$	$0.47^\circ \pm 1.32^\circ$	54.4°	469
	2+3+4	$3.33^\circ \pm 1.47^\circ$	$4.08^\circ \pm 1.47^\circ$	43.4°	359
Schwabe	7 (second half)	$(3.24^\circ \pm 0.55^\circ)$	$(3.12^\circ \pm 0.55^\circ)$	(41.0°)	2243
	8	$4.36^\circ \pm 0.47^\circ$	$5.05^\circ \pm 0.47^\circ$	42.9°	3419
	9	$4.71^\circ \pm 0.34^\circ$	$4.79^\circ \pm 0.34^\circ$	40.3°	4942
	10	$4.74^\circ \pm 0.36^\circ$	$4.94^\circ \pm 0.36^\circ$	39.7°	4898
Spörer	10 (end)	$(2.91^\circ \pm 1.15^\circ)$	$(1.77^\circ \pm 1.15^\circ)$	(19.5°)	465
	11	$4.59^\circ \pm 0.76^\circ$	$4.59^\circ \pm 0.76^\circ$	32.0°	1067
	12	$5.73^\circ \pm 0.80^\circ$	$4.63^\circ \pm 0.80^\circ$	34.3°	833
	13 (beginning)	$(5.85^\circ \pm 1.11^\circ)$	$(5.64^\circ \pm 1.11^\circ)$	(32.6°)	469

angle distributions separately for cycles 0 and 1 and the remaining part of the data. Using only the data with quality flag of 1 (disk orientation obtained from rotational matching of spots on adjacent days), the distinction between the two types of cycles is even clearer: the mean tilt for cycles 0 and 1 is $0.24^\circ \pm 1.61^\circ$, and it is $5.68^\circ \pm 1.83^\circ$ for the cycles 2–4. The mean tilt angle for the cycles 0 and 1 is lower and on par with the mean tilt of Zuconni’s data. The combined mean tilt for cycles 2–4 from the Staudacher data are higher and compatible with values of modern data. While the Staudacher data alone may be too inaccurate, the agreement with Zuconni’s data is an indication for the peculiarity of the cycles 0 and 1.

The Schwabe data comprise cycles 7–10, while the Spörer data cover cycles 10–13. The data for the initial two years of cycle 7 are missing in the Schwabe data, however. Data from Spörer are also not available for the first half of cycle 10 and the second half of cycle 13. The spots being located at predominantly very low latitudes at the end of cycle 10 cause an underestimate of the mean tilt angle, according to Joy’s law. Table 3.2 lists the mean and median tilt values for a number of cycles in the period ~ 1620 –1890. The FWHM were again derived from fits with Gaussian distributions. The average tilt for cycles 0 and 1 are the lowest of all solar cycles for which we have analysed drawings so far.

3.3 Conclusions

The various historical sunspot observations by Scheiner, Hevelius, Staudacher, Zucconi, Schwabe, and Spörer offer white-light sunspot drawings during the 17th, 18th, and 19th centuries. The tilt angles for the supposedly bipolar sunspot groups from those different sunspot observations were calculated. The values from the period before the Maunder minimum (years in the 1620s and 1640s) are comparable to precise 20th-century results. The importance of the tilt angles for the transport of magnetic flux on the surface and the polar field was first noticed by [Leighton \(1964\)](#). Various effects of averaged tilt angles have been studied more recently (cf. e.g. [Baumann et al., 2004](#); [Cameron et al., 2010](#)). The fact that the pre-Maunder minimum average tilt angles are relatively large suggests that it was not particularly low values that initiated a period of very low activity. If flux-transport dynamos are indeed operating in the Sun, more subtle effects such as, e.g., the occurrence of equator-crossing groups ([Cameron et al., 2013](#)) or other group properties need to be studied to find precursors for the very deep minimum following cycle –10.

The cycle-averaged tilt angle values were also calculated for the solar cycles 0–4 and 7–13 from Staudacher, Schwabe and Spörer data. The mean tilt value for the cycles 0 and 1 seems to be the lowest of all cycle-averaged tilt angles, independently shown from sunspot drawings by Staudacher and precise images made by Zucconi. The accuracy of the Staudacher images may be questioned on the one hand, especially their orientation, but the agreement with Zucconi’s data, on the other hand, is striking. The Sun also appeared to have a slightly stronger differential rotation in that period as compared to today ([Arlt and Fröhlich, 2012](#)), but the result was not significant. Since this period is about three to four cycles after the Maunder minimum, it is not clear whether the features still represent the recovery from a grand activity minimum. While that early Staudacher period needs careful future inspection, the cycles before and after the Maunder minimum are clearly very valuable in constraining which kind of dynamo is operating in the Sun.

Chapter 4

Sunspot positions, areas, and group tilt angles for 1611–1631 from observations by Christoph Scheiner

R. Arlt, V. Senthamizh Pavai, C. Schmiel, and F. Spada

Astron. Astrophys. 595, A104. Accepted 5 August 2016

Solar activity is to a large extent characterized by the sunspot number and the latitudinal distribution of spots as functions of time. More information on the activity is, of course, accessible if enough details of the structures at the solar surface are available.

Extending the sunspot record back in time is not only a matter of obtaining reliable sunspot numbers and related indices for as many cycles as possible, but it is also a matter of reconstructing the solar butterfly diagram of the Sun. With the available sources of pre-photographic observations, we may be able to compile an almost complete butterfly diagram for the telescopic era since AD 1610.

Not many publications exist with positional measurements of sunspots observed in the beginning of this era, namely in the first half of the 17th century. Studies of the solar rotation are available for Harriot by Herr (1978) for the period 1611–1613, for Scheiner by Eddy, Gilman, and Trotter (1977) for the period 1625–1626, for Hevelius by Eddy, Gilman, and Trotter (1976) and Abarbanell and Wöhl (1981) for 1642–1644, and for Scheiner as well as Hevelius by Yallop *et al.* (1982), but the sunspot positions were not published. Sunspot positions from Galileo's observations in 1612 were derived and made available by Casas, Vaquero, and Vazquez (2006)¹.

Christoph Scheiner lived from 1573–1650 (Braunmühl, 1891; Hockey *et al.*, 2007)² and was a member of the Jesuit society (Societas Iesu). The present paper is based on the copy of Scheiner (1630) stored in the library of the Leibniz Institute for Astrophysics Potsdam (AIP) and Scheiner (1651) at the library of ETH Zürich, available as a high-resolution digital version through the Swiss platform for digitized content, e-rara³. The observations cover the years of 1611–1631, albeit most of the data comes from 1625 and 1626. Data from the period before the Maunder minimum are interesting since they may tell us details about how the Sun went into a low-activity phase that lasted for about five decades, in particular since Vaquero and Trigo (2015) suggested that the declining phase of the solar cycle had already started around 1618.

¹Historical archive of sunspot observations at <http://haso.unex.es/>

²Some biographies also give 1575 as the year of birth, e.g. Brockhaus (1992).

³<http://www.e-rara.ch/zut/wihibe/content/titleinfo/765922>.

If information on individual sunspots and pores within sunspot groups is preserved, quantities such as the polarity separation and the tilt angle of bipolar groups may be inferred. It will be of particular interest to discover whether these quantities behaved differently in the period before the Maunder minimum as compared to the cycles after it or present cycles. This is not the first attempt to use sunspot positions derived from Scheiner’s observations. An estimate of the differential rotation was, for example, derived from Scheiner’s book by [Eddy, Gilman, and Trotter \(1977\)](#), who concluded that the rotation profile was not significantly different from the one obtained for the 20th century. The authors did not, however, publish the obtained spot positions. Scheiner actually noticed different rotation periods for different spots spanning from 25 to 28 days ([Scheiner, 1630](#), p. 559). He does not, however, say that these periods were attached to specific latitudes of spots.

Scheiner (1573–1650) belongs – together with Johannes Fabricius, Galileo Galilei, Thomas Harriot, Joachim Jungius, Simon Marius, and Adam Tanner ([Neuhäuser and Neuhäuser, 2016](#)) – to the first observers who left records of sunspots seen through a telescope. Scheiner’s first observations were made in early March 1611, together with the student Johann Baptist Cysat (1586–1657). Scheiner was the first observer to start sunspot drawings on a systematic, day-by-day basis in October 1611. A comprehensive investigation of the sunspot observations of the 1610s can be found in [Neuhäuser and Neuhäuser \(2016\)](#).

The following paper describes the drawings and gives details of the drawings in Sect. 4.1, explains the measuring method for 1618–1631 in Sect. 4.2, the methods used to utilize the drawings of 1611–1612 in Sect. 4.3, evaluates the accuracy of the data in Sect. 4.4, gives the data format and the butterfly diagram in Sect. 4.5, and deals with the sunspot group tilt angles in Sect. 4.6. A summary is given in Sect. 4.7.

4.1 Description of the Rosa Ursina and Prodromus drawings

[Scheiner \(1630\)](#) provides 71 main image plates with observations, of which one is unnumbered since it contains only detailed faculae drawings, plus an additional plate with his first observations of 1611. The plates always contain information on more than one day. The number of different days covered varies between four and 54. Early drawings are available from the letters of Scheiner to Marcus Welser in 1611 and 1612. Further sunspot drawings are printed in [Scheiner \(1651\)](#)⁴, where Scheiner defends the geocentric model. There are 12 image plates with spots from 1625, 1626, 1629, and 1631. The drawings are in exactly the same style as the ones in [Scheiner \(1630\)](#), and we used the same analysis procedure as described below. The total number of days for which we have sunspot information is 798, while two additional days show only faculae. Table 4.1 gives the annual numbers of days available.

Five observing locations contributed to this compilation of results on sunspots. Scheiner was located in Rome, Italy, in the years 1624–1633 and we assume geographical coordinates of 12.45° eastern longitude and 41.90° northern latitude for his position. The other locations were Ingolstadt in Germany, Douai (Duacum in Latin) in France, Freiburg im Breisgau, Germany, and Vienna, Austria.

The University of Freiburg and the Jesuit church next to it were located at 7.85° E, 48.00° N. One probable observer was a pupil of Scheiner, Georg Schönberger (or Schomberger) ([Braunmühl, 1891](#)) who later observed with Johann Nikolaus Smogulecz (or Jan Mikołaj Smogulecki). The observations are also available in a separate publication by [Smogulecz and Schönberger \(1626\)](#).

For Ingolstadt, we assumed the position of the original university building, Hohe Schule, at 11.42° E and 48.76° N. Scheiner gave the geographical latitude on top of a page of 1611 obser-

⁴We came to know about this book after finishing the paper presented in Chpt. 3, so the tilt angles vary very slightly in these chapters.

Table 4.1: Numbers of days available for given years as reported by Scheiner (1630), Scheiner (1651), and Reeves and Van Helden (2010).

Year	Days	Year	Days	Year	Days
1611	41 ^a	1622	17	1626	169 ^b
1612	31	1623	9	1627	55
1618	7	1624	40	1629	49 ^c
1621	27	1625	343 ^b	1631	12
Total	800				

Notes.^a Five days were not analysed because of unreliable positional results.^b One day showed only faculae.^c Two days were omitted because groups were not drawn completely.

uations as 48.67° . After Scheiner left Ingolstadt in 1616, the observers could have been Scheiner’s pupils, among them Johann Baptist Cysat, Chrysostomus Gall, and Georg Schönberger (Braunmühl, 1891). Cysat taught in Luzern, Switzerland, from 1624–1627 though (Zinner, 1957). Since the observations from Ingolstadt that were not made by Scheiner cover the period from 1623 March 26 to 1625 September 15, they were most likely not made by Cysat. Scheiner cites Georg Schönberger as the correspondent of the Ingolstadt observations, but Schönberger taught in Freiburg later, and his books of 1622 and 1626 were published in Freiburg. It remains unclear to us who was the observer in Ingolstadt.

For Douai, we assume approximately 3.1° E, 50.4° N. Since the University of Douai was a conglomerate of colleges and the Jesuits erected their own school in the 1620s, it is less obvious from which exact place they observed, but not really relevant for the scope of this paper. The observer in Douai was Karel Malapert (Charles Malapert, Carolus Malapertius) who published his own observations in two books (Malapertius, 1620, 1633). While it was published in Douai, Braunmühl (1891) mentions his observations to be made at Danzig, Poland. This may be a translation error of Duacum, although Malapert did teach in Poland, but at the Jesuit College of Kalisz from 1613–1617 (Birkenmajer, 1967). Scheiner regularly compares the observations of the three sites in his figures. We include all spots visible in these drawings in the data set, but if a spot was observed by Scheiner as well as a colleague on the same day, we give only Scheiner’s spot position.

The location of the Jesuit church in Vienna is about 16.4° E, 48.2° N. Scheiner names Johann Cysat as the observer whose life between 1627 and 1631 is not known in detail. At least, we find an indication that Cysat was in Vienna “occasionally” in that period from Zinner (1957). Scheiner compared the Vienna data with the Rome data, so there is eventually only a total of six spot measurements that complemented the Rome data (recorded on 1629 August 12, 13, and 20).

Typical figures contain a circle for the solar limb, a horizontal line mostly denoting the ecliptic, and a selected number of sunspot groups that are followed on several days. The dates (in many cases together with a precise time and the elevation of the Sun) are given in a small table within the circle.

The next figure gives another set of selected groups for a sequence of days. We note that these sequences of some drawings very often overlap. The figures are made in such a way as to show all appearances of a given group on as many days as necessary.

Times are given in 12-hour format, annotated with “m” = matutinus = morning and “u” = uespera = vespera = evening. The only exception is the first drawing of the 1624–1631 spell. The times are all above 12:00, but since Scheiner also gave the elevations of the Sun, we can guess the most plausible meaning for the times. We find that the time was very likely measured from

Table 4.2: Assumed times specially for Plate I.

Printed time	Assumed time	Printed elevation
Dec 17, a.m. 16:48	09:13	14.5°
Dec 19, a.m. 17:30	09:55	17.7°
Dec 16, a.m. 18:48	11:13	24.5°
Dec 16, p.m. 21:00	13:25	21.7°
Dec 14, p.m. 21:45	14:10	22.5°

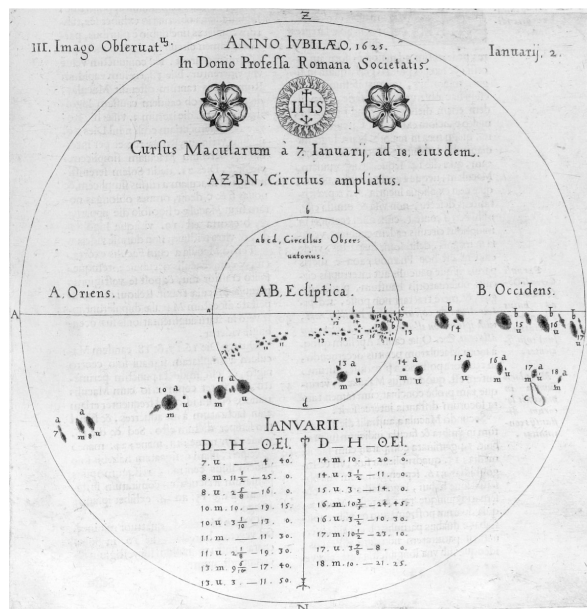


Figure 4.1: Example of an early drawing, indicating the directions and an inner circle annotated as the observed circle. All spots appear twice: once in the inner circle and once in the full circle.

the last sunset, which is at about 16:25 local time in Rome in mid-December. The corresponding local times in today’s reading are given in Table 4.2, sorted by local time instead of date. All other plates give local times apparently measured from midnight.

The printed versions of the drawings were digitized with a book scanner at a resolution of 200 dpi. One pixel corresponds to 0.13×10^{-3} m converting to an angular distance of a bit less than 0.1° in heliographic coordinates in the solar disk centre. The observations of 1611 December 14 to 1612 April 7 were not shown by Scheiner (1630); these were digitized from Reeves and Van Helden (2010). Their diameter is about 22.7×10^{-3} m. A distance of 0.1×10^{-3} m on those disks corresponds to an angle of 0.5° in heliographic coordinates in the disk centre.

The images I to V, IX, X, XVI, XVII contain a smaller circle which is annotated as the “circellus observatorius” = “observed circle”, while the large circle covering almost the entire page is entitled the “circulus ampliatus ex observatorio” = “circle expanded by observatory”. Figure 4.1 shows the example of Plate III. Spots are plotted twice in these drawings, once at the scale of the inner circle and once at the scale of the outer circle. We use the large version of the drawing for position and area measurements. As shown in Sect. 4.4, the accuracy of the positions is remarkable, even though the large images may be the result of post-observational magnifications.

Another peculiarity is shown in Fig. 4.2 covering the period of 1625 March 20 to April 6. The southern hemisphere of the Sun was so crowded with spots that some sunspot groups were plotted into a rotated coordinate system to avoid overlap with groups of other days. A few spots were actually plotted twice: once within the crowd of spots and once at another location. These

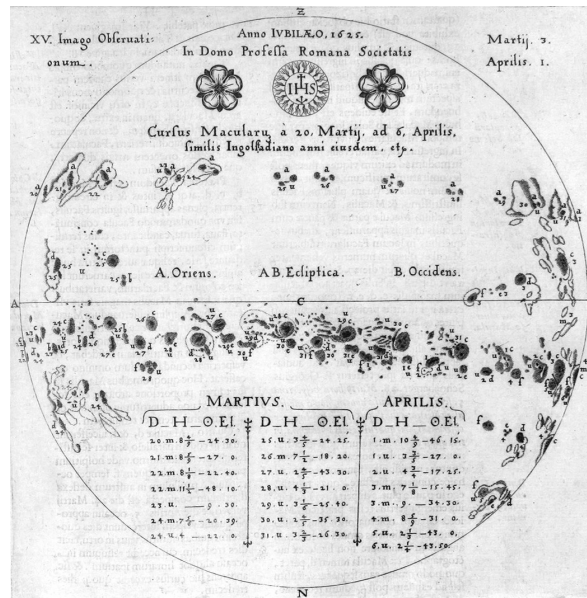


Figure 4.2: Example of a variable ecliptic line to avoid crowdedness. Spots near the eastern and western limbs of the southern-hemisphere groups are rotated above and below their actual position for better visibility. Group a in the northern hemisphere is unaffected.

Class	1	2	3	4	5	6	7	8	9	10	11	12	13
	-	◇	◻	◻	○	○	○	○	○	○	○	○	○
Area in pixels	2	5	9	21	37	69	97	145	185	221	270	308	364

Figure 4.3: Cursor shapes used to estimate the sizes of the spot umbrae and pores.

spots indicate that it is indeed a rotation of the disk by multiples of roughly 15° that led to the secondary positions, and not a linear shift upward or downward.

Image XX contains a large number of faculae crossing the solar disk, while there is only a small group on the southern hemisphere for which we actually determined positions and sizes.

Image XXII shows extended faculae at the eastern limb and sunspots for the period 1625 May 2–14. The faculae of May 3 are drawn in a rather dark colour, possibly indicating very bright faculae, keeping in mind that faculae needed to be plotted with an inverse greyscale. There is a large c-shaped black area surrounding a blank-paper region which appears bright in contrast to the dark surrounding faculae. [Rek \(2010\)](#) seem to argue in a footnote that this region may have been a white-light flare. The textual description of 1625 May 2–4 by [Scheiner \(1630, p. 208\)](#) says the following:

On the second day of May, two spots appeared which were preceded by a facula. On the third day, they showed up with a much more luminous retinue of faculae and a more pompous armament of shadows blending into spots. Just as the faculae extended on the fourth day and the shadows dissipated, many more spots appeared.

(While Scheiner uses the word “umbra”, we translated it into shadow, since the conception of an umbra may have been different to today’s definition.) Since there is no mention of a phenomenon being variable during the course of the day, there is no clear evidence for a white-light flare, despite the presence of a peculiar sunspot group.

There is an unnumbered image plate between images XXVI and XXVII that contains only faculae and covers days that were already shown in images XXIII and XXIV, and has therefore not been used in our measurements.

4.2 The coordinate system of the drawings of 1618–1631

Scheiner describes his observing method as a projection behind the telescope(s). This would mean that the appearance of the Sun was mirrored. There are several indications, however, that he made the actual images in a non-mirrored way, and the orientation of the drawings is roughly upright.

More precisely, the drawings always show a nearly horizontal line representing the ecliptic. Since the plane of the ecliptic is not easily accessible when observing under the sky, it has apparently been computed by Scheiner from the direction to the local zenith. The direction to the local zenith is marked on a few drawings by little dots at the solar limb.

We need to find the angle between the direction of the solar rotation axis and the pole of the ecliptic. As already performed by Arlt *et al.* (2013), we use the output of the angle of the solar rotation axis with the direction to the true-of-date celestial north pole, as provided by the JPL Horizons ephemeris webpage⁵. The ecliptic pole is assumed to be at $\alpha_E = 18^h$, $\delta_E = 66.56^\circ$, which is true-of-date by definition (neglecting orbital precession and nutation). We then use a spherical transformation to obtain the missing angle between the celestial north pole and the ecliptic pole for a given date and location. When transforming the celestial coordinates of the ecliptic pole into a system with its pole in the centre of the Sun, the new longitudinal angle is the desired angle. Let α_\odot , δ_\odot be the celestial coordinates of the Sun and α_E and δ_E the celestial coordinates of the ecliptic pole, then

$$\begin{aligned}\sin \delta' &= \cos \delta_E \cos \alpha_E \cos \delta_\odot + \sin \delta_E \sin \delta_\odot \\ \cos \hat{\alpha} &= (\cos \delta_E \cos \alpha_E \sin \delta_\odot - \sin \delta_E \cos \delta_\odot) / \cos \delta' \\ y &= \sin \alpha_E \cos \delta_E \\ \alpha' &= \begin{cases} \pi - \hat{\alpha} & \text{if } y \geq 0 \\ \hat{\alpha} - \pi & \text{otherwise} \end{cases}\end{aligned}\tag{4.1}$$

(4.2)

Looking at the Sun, α' is also now an angle running counter-clockwise.

We can now cross-check the accuracy of Scheiner's determinations of the ecliptic by computing the angle between the zenith and the pole of the ecliptic. This angle can be measured in a few drawings where the zenith is indicated at the solar limb. We are again using the spherical transformation and replace the celestial coordinates of the ecliptic pole by the celestial coordinates of the local zenith at the time of observation. Within the Interactive Data Language (IDL), this position is provided by the `zenpos` routine of the Astronomy User's Library of November 2006 (Landsman, 1993). Table 4.3 gives a comparison of angles between the zenith and the north pole of the ecliptic, one value being measured on the drawing directly, and the other values being computed from the solar ephemeris. The differences are typically a fraction of a degree, but reach 1.9° on 1625 November 14.

Since neither the printing of the drawings nor the digitization process ensure that the ecliptic is an exactly horizontal line in the image, we also need to add the angle of the printed line, which is obtained by clicking on two points on the line in the image and computing the angle (typically below 1°).

The actual process of measuring the sunspots consists of the following steps: (i) cutting out the solar disk from the full image by clicking on the left-most, right-most, lowest and uppermost limbs of the Sun; this also allows for a certain degree of ellipticity of the solar disk to be measured correctly), (ii) determining the exact angle of the ecliptic line by two clicks, left and right, (iii) setting up the spherical coordinate system as supported by IDL, (iv) clicking on the relevant spots with 13 different cursor sizes (Fig. 4.3), for which the best fit in position and size to the umbrae and pores are sought visually.

⁵<http://ssd.jpl.nasa.gov/horizons.cgi>

Table 4.3: Angle between the direction to the pole of the ecliptic and the zenith as indicated in the drawings and theoretically determined.

Date and time	Drawing	Ephemeris	Diff.
1626-05-19 08 ^h 00 ^m	−38.5	−38.9	0.4°
1625-05-20 16 ^h 10 ^m	64.2	65.0	0.8°
1625-05-28 08 ^h 35 ^m	−41.2	−42.1	0.9°
1625-05-31 08 ^h 10 ^m	−43.2	−44.4	1.2°
1625-11-03 08 ^h 22 ^m	−54.7	−55.1	0.4°
1625-11-12 09 ^h 00 ^m	−47.6	−47.0	0.6°
1625-11-14 14 ^h 30 ^m	14.3	16.2	1.9°

Notes. The last column is the absolute difference between drawing and ephemeris.

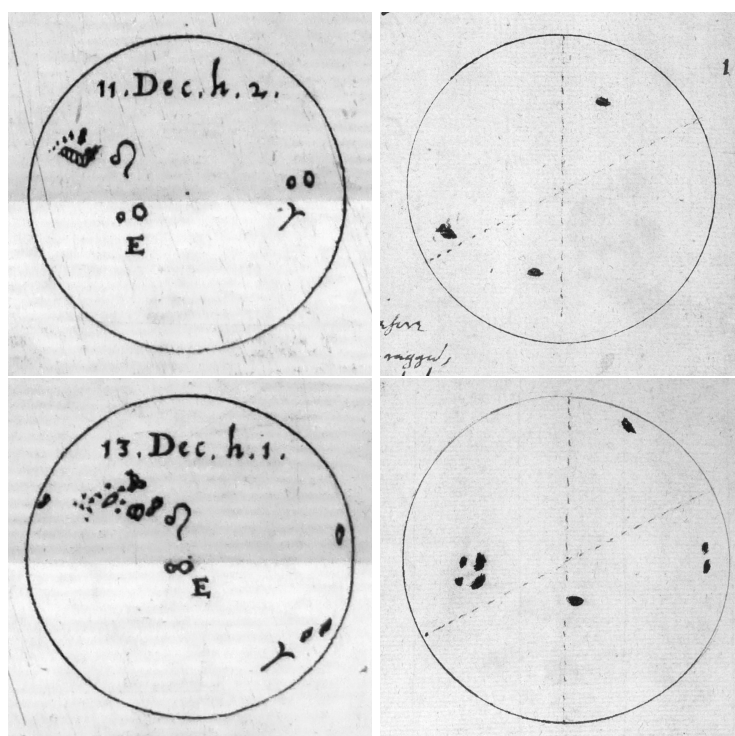


Figure 4.4: Comparison of the drawings by Scheiner (left) and Harriot (right) on the two days they have common observations. The top row shows the observations of 1611 December 11, at 14 h (left) and at 10 h (right). The bottom row is of 1611 December 13, at 13 h (left) and at 8:30 h (right). The vertical dashed lines in Harriot's drawings denote the (observed) direction to the zenith, the other dashed lines are the (computed) ecliptic.

In cases where a rotated coordinate system was used to draw spots of crowded regions (see Sect. 4.1), we can determine the positions if at least one spot was plotted twice, once in the standard ecliptical system, and once in the rotated one. The angle with the disk centre gives us the rotation of the coordinate system for the displaced spots. For 15 spots, this type of duplicate spot was not available, and we omit the positions of these spots, but keep corresponding records in the data file.

Physical areas are then derived from the pixel area of the cursor shapes A_{cur} used for the individual spots, as compared with the total pixel area of the solar disk, A_{disk} . The heliocentric distance of the spot from the disk centre δ yields the correction for the geometrical foreshortening, and we express the final area in millionths of the solar hemisphere, i.e.,

$$A = \frac{1}{2 \cos \delta} \frac{A_{\text{cur}}}{A_{\text{disk}}} \times 10^6. \quad (4.3)$$

4.3 The observations of 1611–1612

The observations of 1611 October 21 to 1612 April 7 are Scheiner’s first drawings of sunspot observations and are more difficult to measure. The ones of 1611 October 21–December 14 are compiled on a single page in the *Rosa Ursina*. The page is essentially the same as the one Scheiner sent to the scientific friend Marcus Welser using the pseudonym *Apelles latens post tabulam* (Apelles hiding behind the scaffold) written on 1611 December 26, and published by Welser in January 1612, together with two earlier letters (Braunmühl, 1891). Additional drawings up until 1612 April 7 are available from the letters to Welser of 1612 January 16, April 14, and July 25 (Apelles, 1612). We did not have access to the originals, but used the reproductions of the drawings in Reeves and Van Helden (2010) instead.

Some observations show an approximate orientation: the ones of the morning and afternoon of October 22 show the horizon, the ones from 1611 December 10 to 1612 January 11 show the ecliptic; the other drawings have no information about the orientation of the solar disk. The ecliptic was drawn in connection with the expected Venus transit on 11 December which was actually an upper conjunction of Venus and the Sun. The images of 10–13 December also contain the expected path of Venus. The path is confusing as to whether the images may be upside-down or mirrored, since it lies north of the ecliptic, while the true path was south of it. Since the spots are clearly moving from left to right, there was still the possibility that the images are mirrored vertically (a view on a projection screen behind a Galilean telescope). The description reveals, however, that the path was indeed meant to be north of the ecliptic; the accuracy of the ephemeris of Venus was just not good enough (especially of the ecliptic latitude) to place it right at the time (Reeves and Van Helden, 2010). For all drawings showing the ecliptic, we computed the angle between the solar axis and the direction to the pole of the ecliptic and set up the coordinate system in the same way as for the observations of 1618–1631. There were 29 observations for which the ecliptic was used in 1611–1612.

There are three options for carrying out the analysis of the remainder of the drawings: (i) using two or more drawings to fix their orientation with the spot displacements owing to the solar rotation (rotational matching); (ii) assuming that all the drawings are plotted in a horizontal system, i.e. the vertical on the book page points to the zenith; or (iii) choosing an arbitrary orientation such that the distribution of spots agrees with today’s expectation of sunspot latitudes.

Method (i) for the rotational matching is the same as described in Arlt *et al.* (2013). Two or more spots that can be identified in two or more consecutive drawings are used with their measured Cartesian coordinates for a Bayesian inference of their heliographic central-meridian distances and latitudes and the orientation angles of the drawings. A differential rotation, as derived by Balthasar, Vázquez, and Wöhl (1986), is used for the solar rotation with a fixed

Table 4.4: Comparison of different coordinate systems adopted for a selected set of observations in 1612.

Date	Number of spots	Avg. distance
1612-03-16	5	0.58°
1612-03-17	5	5.80°
1612-03-18	4	0.30°
1612-03-19	5	3.63°
1612-04-02	11	7.34°

dependence $\Omega = (14.551 - 2.87 \sin^2 \lambda) \text{ }^\circ/\text{day}$, where λ is the heliographic latitude. The relation was computed from the sunspot group series of 1874–1976 compiled by the Royal Greenwich Observatory.

A Markov chain Monte Carlo search in the parameter space provides us with full posterior probability density distributions for each of the free parameters. In contrast to a best-fit search, they enable us to judge the quality of the rotational matching by the width of the probability density distribution, its skewness, or possible non-uniqueness of probable solutions. The orientations of a total of 23 observations was fixed with the rotational matching.

Since imposing the differential rotation of the Sun to the solution of the orientation does not allow a subsequent determination of the differential rotation in a possible future study, we try to use method (ii) for as many cases as possible. The celestial position of the Sun is provided by the Horizons ephemeris in a J2000.0 system. Since the angle between the solar axis and the direction to the celestial north pole is given in a true-of-date system, we transform the Sun’s coordinates to a system of 1612 using the `precess` routine from the IDL Astronomy User’s Library. The position of the zenith is computed by the `zenpos.pro` routine in a true-of-date system as well.

The observations of March and April 1612 are the only ones with a reliable alignment of the zenith direction with the vertical of the images. This was shown by a comparison of measurements with the zenith-assumption and measurements using the rotational matching. Table 4.4 shows the average deviations of the spot positions between the two methods. While the zenith-assumption delivered fairly consistent results of spot motion across the solar disk, the rotational matching yielded rather broad probability density distributions for the position angles and we kept its results only for 1612 March 17, 19, and April 1. In total, 27 observations were treated with this assumption of a horizontal coordinate system.

Method (iii) was applied only when the first two methods led to improbable spot distributions. We essentially applied a position angle which minimizes the absolute latitudes of the spots. Only four observations were treated with arbitrarily chosen orientations (1611 November 7, 13, 14, and December 8).

The observations of 1611 November 6, 9, 10, 12, and December 24 were omitted entirely because no reasonable match with adjacent observations was possible and the spot distribution appears to be highly improbable. The resulting heliographic latitudes of the spots measured in the 83 observations used from 67 days in 1611–1612 are between -43° and $+42^\circ$.

The sizes of the spots were greatly enlarged, and groups of smaller spots were combined into one large spot, as described by Scheiner (see [Reeves and Van Helden \(2010\)](#) for a translation). A size estimate can only be arbitrary at this point, and we chose – to be able to use the 13 cursor shapes – to select the size class that matches roughly half the diameter of the plotted spot. This choice still creates too large areas when converting the disk area fraction of the cursor shape directly to MSH. The areas in the data file are shown with “!” to indicate that these need to be used with care (see Table 4.6).

Table 4.5: Comparison of the positions of the same spot in two different image plates.

Date	Plate XLVI			Plate XLVII			
	CMD	λ	S	CMD	λ	S	δ
Nov. 06	-73.9°	-6.0°	3	-74.4°	-5.8°	3	0.54°
Nov. 07	-60.6°	-5.5°	5	-61.6°	-6.2°	5	1.22°
Nov. 08	-47.1°	-5.9°	4	-48.3°	-5.9°	5	1.19°
Nov. 09	-33.9°	-5.0°	5	-34.8°	-5.0°	5	0.89°
Nov. 10	-20.4°	-4.7°	5	-20.9°	-4.8°	4	0.51°
Nov. 11	-7.4°	-4.8°	5	-7.8°	-5.0°	4	0.45°

Notes. CMD is the central-meridian distance, λ is the heliographic latitude, S is the cursor size class according to Fig. 4.3, and δ contains the heliocentric distance between the two measurements.

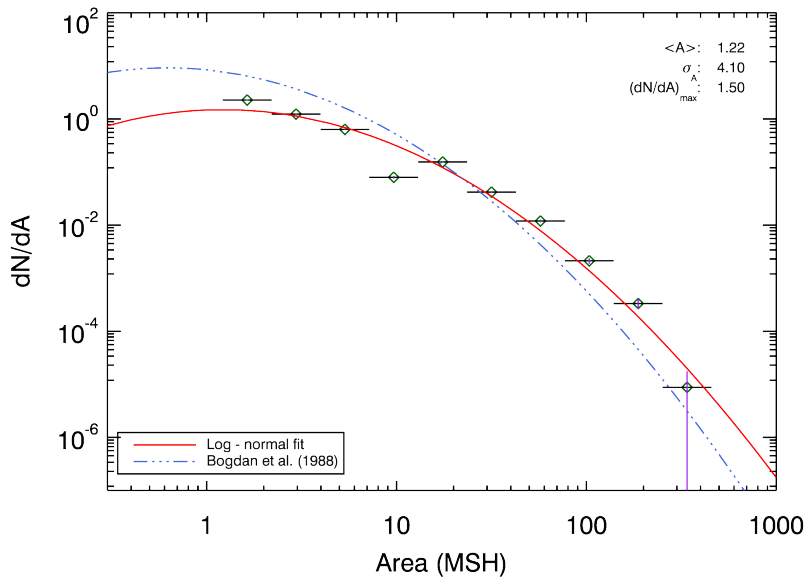


Figure 4.5: Area distribution of 5555 spots drawn by Christoph Scheiner in 1618–1631, all within a central-meridian distance of $|\text{CMD}| \leq 50^\circ$.

4.4 Accuracy of the positions and areas

In the first period of 1611–1612 when Scheiner drew the sunspots with poor quality, there are actually two occasions when Scheiner and Thomas Harriot (1613) observed on the same day (Fig. 4.4). The images are rotated against each other, since Harriot observed in the morning and Scheiner in the afternoon. There is a fair agreement on the distribution of spots, except that Scheiner noticed a spot near the eastern solar limb on 1611 December 13, which Harriot could not yet detect. Scheiner’s drawings are more detailed, whereas the spots are more exaggerated in size than in Harriot’s drawings. While the drawings look qualitatively similar, we find positional differences of up to 20° on those two days (assuming Harriot’s vertical lines are the direction to the local zenith). This underlines the limited use of the spots in 1611.

Accidentally, Scheiner plotted the positions of one spot in two different image plates (XLVI, spot labelled as “k”, and XLVII, spot labelled as “a”) from 1625 November 6–11. The differences provide us with information on how well the positions may have been reproduced in the plates and are listed in Table 4.5. The average distance between the positions of the spot in plate XLVI and the corresponding positions in plate XLVII is 0.8° . The average ‘error’ of the cursor sizes chosen for the various instances of the spot is 0.5 classes. We kept the positions of plate XLVII, since the spot continued to exist for more days after November 11.

Table 4.6: Data format for the positions and areas of individual sunspots observed by Christoph Scheiner and his collaborators.

Field	Column	Format	Explanation
YYYY	1–4	I4	Year
MM	6–7	I2	Month
DD	9–10	I2	Day referring to the civil calendar running from midnight to midnight, Gregorian calendar
HH	12–13	I2	Hour, times are mean local time at the observer’s location
MI	15–16	I2	Minute, typically accurate to 15 minutes
T	18	I1	Indicates how accurate the time is. $T = 0$ means the time has been inferred by the measurer (in most cases to be 12h local time); $T = 1$ means the time is as given by the observer; $T = 2$ means the time was not printed, but inferred from the elevation of the Sun and the morning/afternoon discrimination given by the observer.
L0	20–24	F5.1	Heliographic longitude of apparent disk centre seen from Rome
B0	26–30	F5.1	Heliographic latitude of apparent disk centre seen from Rome
CMD	32–36	F5.1	Central meridian distance, difference in longitude from disk centre; contains NaN (not a number) if position of spot could not be measured.
LLL.L	38–42	F5.1	Heliographic longitude in the Carrington rotation frame; contains NaN if the position of spot could not be measured.
BBB.B	44–48	F5.1	Heliographic latitude, southern latitudes are negative; contains NaN if the position of spot could not be measured.
M	50	C1	Method of determining the orientation. E: ecliptic present in drawing; H: book aligned with azimuth–elevation; A: arbitrarily chosen orientation according to the distribution of groups; Q: rotational matching with other drawings (spots used for the matching have ModelLong \neq ‘-.’, ModelLat \neq ‘-.’, and Sigma \neq ‘-.’).
Q	52	I1	Subjective quality, all directly connected to the ecliptic drawn by Scheiner get $Q = 1$. The rotated sunspot groups (see Fig. 4.2) are probably slightly less accurate and get $Q = 2$. Positions derived from rotational matching may also obtain $Q = 2$ or 3, if the probability distributions fixing the position angle of the drawing were not very sharp, or broad and asymmetric, respectively. Methods H and A always obtain $Q = 3$, because of the assumptions made. Spots for which no position could be derived, but have sizes, get $Q = 4$.
SS	54–55	I2	Size estimate in 13 classes running from 1 to 13. The classes are different from the ones used in Arlt <i>et al.</i> (2013) and (Senthamizh Pavai <i>et al.</i> , 2015) ^a by the fact that we introduced a smaller size at the low end and named it “1”. The classes are arbitrary anyway.
GROUP	57–64	C8	Arbitrary group name; the order of numbers has no meaning
MEASURER	66–75	C10	Last name of person who obtained position
MOD_L	77–81	F5.1	Model longitude from rotational matching (only spots used for matching have this)
MOD_B	83–87	F5.1	Model latitude from rotational matching (only spots used for matching have this)
SIGMA	89–93	F5.3	Total residual of model positions compared with measurements of reference spots in rotational matching (only spots used for the matching have this). Holds for entire day.
DELTA	95–98	F4.1	Heliocentric angle between the spot and the apparent disk centre in degrees (disk-centre distance); it is NaN if the spot position could not be determined.
UMB	100–103	I4	Umbral area in millionths of the solar hemisphere (MSH), corrected for foreshortening; it is NaN if spot position could not be derived.
A	105	C1	Flag (!) indicating areas that are highly uncertain since the spots appear to be drawn at too large a size.

Notes. The Format column uses the following designations: I denotes integer fields with the number behind being the number of characters; similarly, C is a character text field with the corresponding length, and, e.g. F5.1 is a floating point field of five characters length with one decimal.

^aSee Chpt. 2 for details.

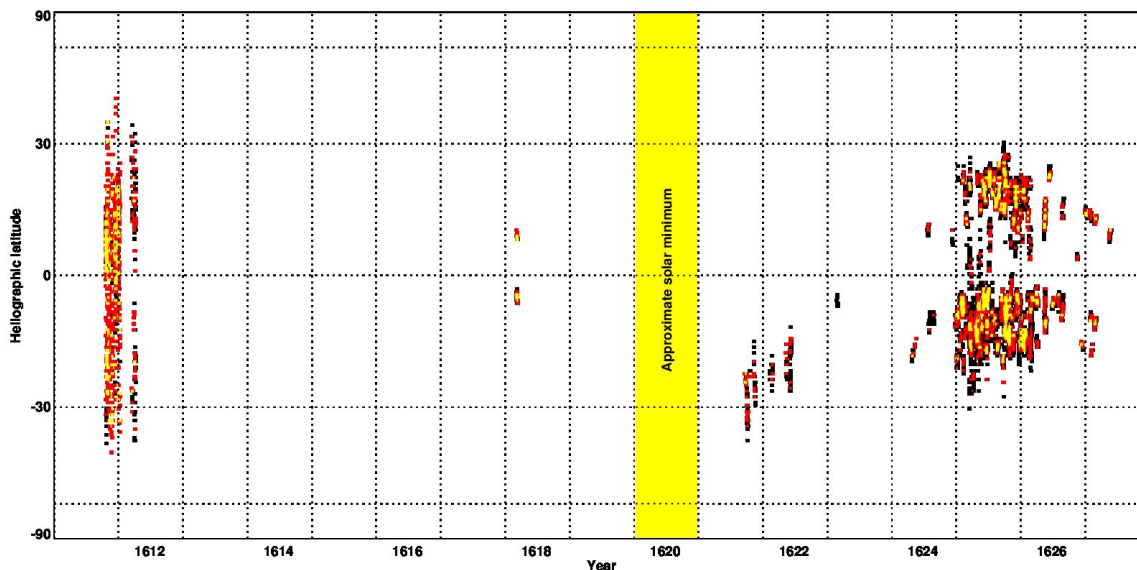


Figure 4.6: Butterfly diagram of the sunspot positions obtained from the observations by Christoph Scheiner and his colleagues. The ordinate is linear in $\sin \lambda$. The umbral areas of the individual spots are used to weight the increments accumulating in each time and latitude bin. The approximate activity minimum is the time recently inferred by Neuhäuser and Neuhäuser (2016).

The areas were taken from pixel counts in the individual cursor shapes and converted into fractions of the solar disk. They are then corrected for foreshortening and given in MSH. We follow the procedure adopted by Bogdan *et al.* (1988) to compute the area distribution of the individual umbrae. The result is shown in Fig. 4.5 and shows a fairly good agreement with their distribution. We interpret the differences from the curve obtained by Bogdan *et al.* (1988) as follows. Firstly, large spots in particular may be slightly exaggerated in size, an effect seen in many other historic sunspot drawings. At the same time, several of the smallest spots were missed as a result of the observational limits (chromatic telescope). These two effects explain the slight overabundance of spots in large areas and the slight under-abundance of spots between 1.2 and 10 MSH. A correction factor of 0.8 may be suitable for the areas, leading to a perfect match with the curve by Bogdan *et al.* (1988) in large areas. However, since this is speculation, we have not used any correction factor for the areas in the resulting data file. It would bring the smallest spots to even smaller areas that were very likely not observable.

The smallest spot measurement delivered an area of only 1.2 MSH. A circular spot of this area has an angular extent of $3''$ in the centre of the solar disk. It is doubtful whether the resolving capabilities of Scheiner’s telescopes were as good as that. While King (1955) reported on Galileo’s largest telescope having an aperture of 5.1×10^{-2} m, but usually being stopped down to 2.6×10^{-2} m. Abetti (1954) reports on a test of one of the first telescopes of Galileo and found a resolving power no better than $10''$. By the 1620s, the telescopes may have improved, and Scheiner also used a Keplerian setup, which provides better image quality. We found only the following remark about the necessary telescope for the precise enough following of the sunspots’ motion in Scheiner (1630, p. 129-2):

We obtain this to an extraordinary degree, if the lens is not only a portion of a large sphere, whose radius spans 20, 30, or more Roman palms, but also if the same [lens] is sufficiently wide, of at least one or two palms; so it will lend itself to do something adequate, as long as it is made of material of good quality and shaped without defects.

The Roman palm measured 74×10^{-3} m (Brockhaus, 1991) leading to impressive suggested lens diameters of 7×10^{-2} – 15×10^{-2} m. We did not find an exact aperture of the actual telescopes

used, but conclude that the resolution in the 1620s was significantly better than that of Galileo's early telescopes. Since the drawings – especially the ones of 1624–1631 contain very small spots, we decided to preserve the size information and leave possible recalibrations of the areas to future applications of sunspot data.

4.5 Data format and butterfly diagram

We use the same table format as the one employed for the spot positions and sizes derived from the observations by Schwabe (Arlt *et al.*, 2013). The format is detailed in Table 4.6. While the measurements deliver central-meridian distances on the Sun, heliographic longitudes are obtained using the solar disk centre provided by the JPL Horizons ephemeris generator seen from the location in Rome (differences to the various other geographical positions in Europe are extremely tiny).

Since Scheiner drew the sunspots – at first glance – to scale in the years of 1618–1631, we computed physical areas in MSH, corrected for the projection effect towards the solar limb. The observations of 1611–1612 do not show realistic areas. We chose cursor sizes of roughly half the diameter of the spot in the image to compensate for the exaggerated spots to some degree subjectively. Nevertheless, these areas should be used with extreme care.

We define sunspot groups based on Scheiner's drawings and assigned group numbers. The order of the group numbers has no meaning; for technical reasons they are not ascending monotonically. The groupings were more difficult for 1611, since the groups may have been drawn too large in size. The remaining group definitions were fairly straightforward, since the drawings have a similar look to modern white-light images (except for faculae). The differences to the group definitions made already by Scheiner are not too large. A total of 16 groups were split into two groups, while 10 groups are the result of combining groups together. These numbers increased slightly as compared to Senthamizh Pavai *et al.* (2016)⁶ after another careful inspection.

A total of about 8152 spot positions were derived for 1611–1631. The exact number may still evolve upon further investigations, since the distinction between spots and faculae is not unambiguous (also drawn by dark ink). The resulting butterfly diagram is shown in Fig. 4.6. A considerable part of a cycle is covered only in the years 1624–1631, where the migration of spot emergences appears to be equatorward. Following Zolotova and Ponyavin (2015), we name this cycle –12. The general migration of sunspot emergence latitude towards the equator is clearly seen. The onset of cycle –12 took place first in the southern hemisphere, while no spot was found in the northern hemisphere. During the second half of cycle –12, the average latitudes of the northern wing are farther away from the equator than in the southern one. The positions are compatible with a time of minimum of fall 1620, as suggested by Neuhäuser and Neuhäuser (2016). Spörer (1889a) gives 1619, while Hoyt and Schatten (1998) obtained very low group sunspot numbers for both 1617 and 1618, which are mainly due to an overabundance of zero-detections inferred from generic statements of Simon Marius and Andrea Argoli (incorrectly reported as seen by Riccioli in Hoyt and Schatten 1998).

Cycle –13 is more poorly covered. The 1612 observations show the presence of the two butterfly wings nicely, while the 1611 positions are too inaccurate to exhibit the hemispheric division. A slight dominance of the northern hemisphere may be detectable in both 1611 and 1612.

The spot positions and areas are publicly available at the astronomical data centre CDS. Since none of the observational sources before the Maunder minimum covers a sufficient period in time to deliver useful information about a full cycle (the latitudinal distribution of spots in the first place), a unified database of the various data sets is very advantageous.

⁶Chpt. 3

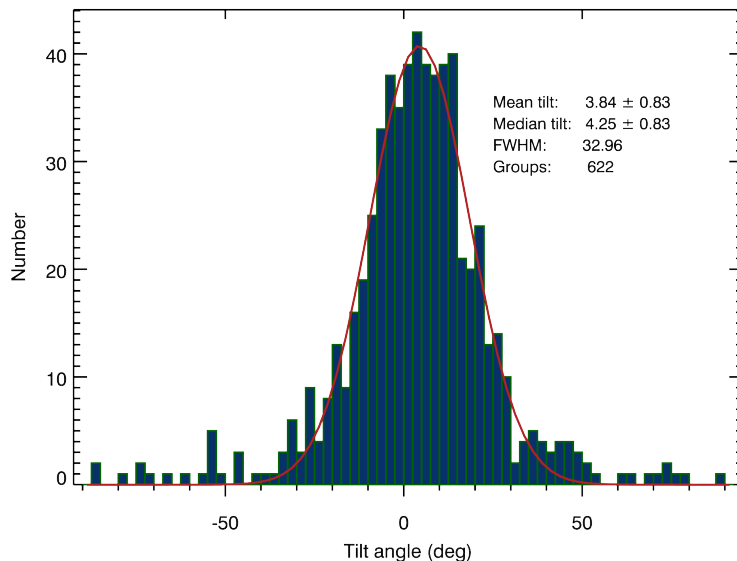


Figure 4.7: Tilt angle distribution for the observations by Scheiner in 1618–1631. The solid line is a Gaussian fit to the distribution and delivers the full width at half-maximum (FWHM). After [Senthamizh Pavai et al. \(2016\)](#).

4.6 Sunspot group tilt angles

The drawings by Scheiner and his colleagues were then manually inspected for potential bipolar sunspot groups. We restricted the analysis to the very realistic drawings of 1618–1631. The relevant groups were flagged in the positional database and tilt angles were computed according to the method described by [Senthamizh Pavai et al. \(2015\)](#)⁷. The data format of the tilt angle data file is exactly the same as in that paper⁸. The total number of tilt angles obtained is 697.

The distribution of the 622 tilt angles within central meridian distances of $|\text{CMD}| < 60^\circ$ is shown in Fig. 4.7. The width of the distribution was derived from a Gaussian fit to the histogram. The average tilt angle of $3.84^\circ \pm 0.83^\circ$ is slightly lower than values of the 20th century. Values by [Wang et al. \(2015\)](#) for cycles 16–23 range from 4.6° to 6.6° , if a minimum polarity separation of 2.5° is used to separate unipolar groups with more than one spot from true bipolar groups. Because of the relatively large error margin of the average for Scheiner, we have to conclude that the value is not significantly lower than in the 20th century (see [Senthamizh Pavai et al. \(2016\)](#) for more average tilt angles in the course of four centuries). Most of the data are from 1625–1627, which is roughly the year of solar maximum and two years of the descending activity.

⁷See Sect. 2.3.1 for details.

⁸Refer to Table 2.4.

4.7 Summary

The solar disk drawings with sunspots made by Christoph Scheiner and colleagues in 1611–1631 were digitized and measured. The three sources for the drawings are [Scheiner \(1630\)](#), [Scheiner \(1651\)](#), and [Reeves and Van Helden \(2010\)](#). A total of 8167 spot areas were obtained of which 8152 are accompanied by heliographic positions. All measurements are provided in a database file. The accuracy of both positions and areas are poor for 1611. The positional accuracy improved in the 1612 observations but the spot areas are still highly exaggerated. High quality drawings of 1618–1631 delivered a positional accuracy of about 1° – 2° in heliographic coordinates in the solar disk centre, thanks to the large scale of the drawings. The database does not contain spotless days. We refer to the detailed tables by [Hoyt and Schatten \(1998\)](#) for estimates of the spotless days that go beyond what [Scheiner \(1630\)](#) reported.

Sunspot numbers may also be incomplete, as indicated by two groups in [Scheiner \(1651, Plate I, belonging to p. 7\)](#) seen on 1625 May 23–29 and 1626 June 30–July 12, respectively, which were not shown in the images of [Scheiner \(1630\)](#). Since this is the only image with an overlap between the two books, it is not possible to estimate the general completeness.

The positional data support the migration of sunspot emergences towards the equator through cycles -13 and -12 . Apart from the very inaccurate 1611 data, there were two groups in 1629 which straddle the equator. On some days, just a few small spots are on the other hemisphere, but on two days (one day for each group), the average polarities sit in opposite hemispheres. Near-equator groups may be interesting for the progress of the activity cycle as recently suggested by [Cameron *et al.* \(2013\)](#). For the accurate period of 1618–1631, we find that 18 bipolar groups have group centre latitudes of $|\lambda| \leq 5^\circ$.

We computed 697 sunspot group tilt angles from a manually selected set of supposedly bipolar group instances (i.e. the same group may be used on more than one day) for 1618–1631 and provide them in a separate data file. The average tilt angle for these observations is $3.84^\circ \pm 0.83^\circ$ and is not significantly different from 20th-century values, albeit on the low side. There were 1341 group instances not selected as being bipolar in 1618–1631.

The data are made available at the astronomical data centre CDS.⁹

⁹Copies of the positional data file and the tilt angle data file are available at <http://www.aip.de/Members/rarlt/sunspots>.

Chapter 5

Wings of the butterfly: Sunspot groups for 1826–2015

R. Leussu, I. G. Usoskin, V. Senthamizh Pavai, A. Diercke, R. Arlt, C. Denker, and

K. Mursula *Astron. Astrophys.* 599, A131. Accepted 9 December 2016

The time-latitude evolution of sunspot occurrence, known as the Maunder butterfly diagram, is one of the most spectacular manifestations of the cyclic variability of solar activity, resulting from the action of solar dynamo in the Sun’s convection zone (Charbonneau, 2010; Hathaway, 2015). With the butterfly diagram, we can study the detailed evolution of the latitude distribution of sunspots and, thus, the dynamo wave propagation (e.g. Newton and Milsom, 1955; Carbonell, Oliver, and Ballester, 1993; Pulkkinen *et al.*, 1999; Li *et al.*, 2002; Ballester, Oliver, and Carbonell, 2005; Berdyugina *et al.*, 2006).

Historically, the butterfly diagram has been studied using the data from the Royal Greenwich Observatory (RGO), which started producing daily photographs of the Sun in 1874. Recently, the butterfly diagram has been studied for earlier times using digitized sunspot drawings of Staudacher (Arlt, 2009), Schwabe (Arlt *et al.*, 2013) and Spörer (Diercke, Arlt, and Denker, 2015). The latter two datasets now enable us to compose a continuous butterfly diagram since 1826, extending the RGO-based diagram by almost 50 years. Here we present the first systematic analysis of the butterfly diagram of sunspot group occurrence in 1826–2015, using the combined dataset. We separate the butterfly wings using a recently developed method (Leussu *et al.*, 2016) and analyze the separate wings for systematic relationships and patterns.

The paper is organized as follows. In Sect. 5.1 we introduce the dataset we used. Sect. 5.2 describes the wing separation process. The latitudinal evolution of the wings is analyzed in Sect. 5.3, their relation with the wing strength is studied in Sect. 5.4, and the synchronization of the wings is studied in Sect. 5.5. Conclusions are given in Sect. 5.6.

5.1 Data

The dataset of sunspot group positions and sizes consists of three subsets: the revised version 1.3 of Schwabe data (Arlt, 2011; Arlt *et al.*, 2013) for the period 1826–1867, the newly digitized Spörer data (Diercke, Arlt, and Denker, 2015) for 1868–1874 (although these data are available from 1861–1894, we use them here only to fill the gap between Schwabe and RGO data), and the RGO/USAF/NOAA/SOON compilation¹ referred to collectively as the RGO data since 1875.

¹<http://solarscience.msfc.nasa.gov/greenwch.shtml>

Since the original RGO series was terminated in 1976, its extension with SOON (Solar Observing Optical Network) data (Neidig *et al.*, 1998) may have a transition inhomogeneity related to the reported group areas (Lockwood, Owens, and Barnard, 2014; Hathaway, 2015). However, this transition does not affect the present analysis where we consider only the number and position of spot groups, not their sizes. However, RGO data quality is known to be rather low before 1880 (Sarychev and Roshchina, 2009; Aparicio *et al.*, 2014) during the incomplete cycle 11. The uneven quality of RGO data may extend, although less dramatically, even until 1900 (Clette *et al.*, 2014), possibly affecting cycles 12 and 13. This uncertainty does not affect definitions of the latitudes, but it may alter the strengths of the cycles. Accordingly, we also considered the “corrected” strengths of cycles 12 (increased by 25%) and 13 (increased by 10%), following the curve in Fig. 24 of Clette *et al.* (2014). The total group area might have been a more robust index than just the number of spots or groups, but it adds a different information about the strength of solar activity: it scales well with the total emerging magnetic flux, but is mostly blind to how this field is fragmented into distinct local magnetic elements (elementary emerging dipoles).

The RGO dataset only includes data of sunspot groups, not of individual sunspots. Although the Schwabe and Spörer data include information on individual spots, we aggregated this information by considering only sunspot groups, in order to be consistent with the RGO data. For each sunspot group we calculated the mean latitude, weighted by the sunspot sizes (umbral area). We used the revised version of Schwabe data with sunspot groups defined according to modern understanding (for detail see Senthamizh Pavai *et al.*, 2015)². This sunspot grouping is somewhat different from that made originally by Schwabe and later used by Wolf, but it ensures consistency with the RGO dataset.

Schwabe and Spörer were good observers, with observational acuity thresholds, as estimated by Usoskin *et al.* (2016a), of 13 ± 5 and 3 ± 2 msd (millionths of the solar disk), respectively. This is comparable to that of RGO, indicating that only very small short-lived groups could have been missed by Schwabe and Spörer with respect to the reference dataset. Accordingly, we did not apply any correction to this possible minor inconsistency. We consider only the high-quality Schwabe data with the quality tag 1, which means the highest possible accuracy for sunspot positions within the data (Arlt *et al.*, 2013). However, in some cases, particularly related to the high-latitude spots, the accuracy of latitude determination may not be very high for Schwabe data, even if the best values were obtained from data with the formal quality tag.

Spörer provided drawings of the Sun in which each observed group was plotted when it was near the central meridian. The spots were identified and measured in an automated search delivering whole-spot areas and locations for individual sunspots (Diercke, Arlt, and Denker, 2015). Very few sunspots were reported in the Spörer data at the beginning of his observing period, as compared to data by Richard Carrington during a small overlapping period in 1861 (Zolotova *et al.*, 2010), but later they reached a higher more normal level. This early inconsistency of the Spörer data has no effect here, since we use these data only beginning in 1868.

To avoid the effect of weighting the results with the lifetime of sunspot groups and group migration, we only took each sunspot group at its first appearance in the record. Subsequent appearances of the same group were ignored. This also emphasizes positions of the groups close to their formation (emergence of the magnetic flux tube), which minimizes their further migration. We note that for the Spörer data the first crossing of the central meridian was considered since he mentioned spots only at these moments.

²See Sect. 2.2 for details

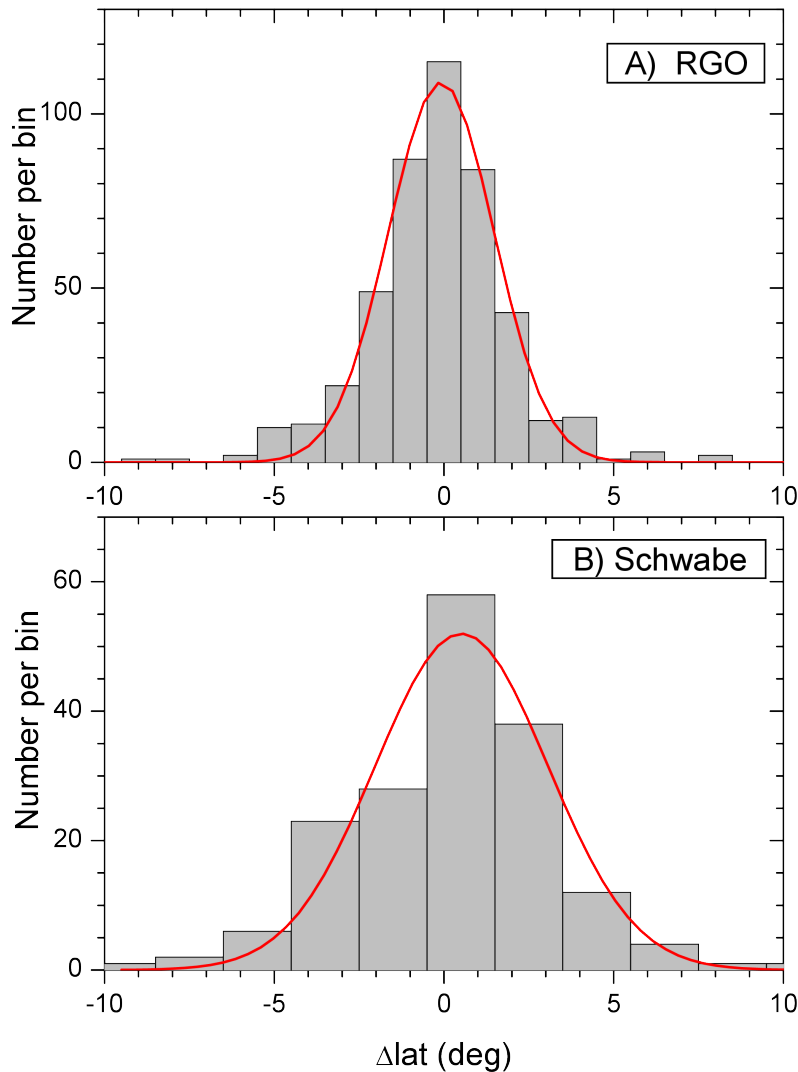


Figure 5.1: Histograms of the occurrence of the difference Δlat between mean latitudes, as defined from Spörer and other observer’s data for Carrington rotations during the period of the data overlap. Panel a: Spörer vs. RGO (the mean of the distribution is -0.2° , the standard deviation $\sigma = 2.2^\circ$). Panel b: Spörer vs. Schwabe (0.25° , $\sigma = 3^\circ$).

5.2 Separation of the butterfly wings

Using the combined RGO, Schwabe and Spörer datasets described in Sect. 5.1 we constructed the butterfly diagram shown in Fig. 5.2. The wings of the diagram were separated using the method described by Leussu *et al.* (2016) for each hemisphere and solar cycle. The method is based on finding long gaps in the appearance of sunspot groups in narrow latitude bands, and ascribes each sunspot group to a certain wing, separating the old and the new cycles during their overlap. Since we consider only the first appearance of each group, in contrast to our previous work (Leussu *et al.*, 2016), where all daily group appearances were used, we renewed the separation of the wings, using the same method, but with the dataset of the first appearance. However, the qualitative difference to the diagram of Leussu *et al.* (2016) is minor. Since the Spörer data overlap with both the Schwabe and RGO datasets, we separated the wings for that dataset separately. The resulting wings for the Spörer dataset are superimposed (in red and blue) on the Schwabe and RGO data wings (shown in green and black) in Fig. 5.2. The Spörer data are clearly well consistent with both Schwabe and RGO-based wings, as shown in Fig. 5.1: the mean latitude difference between Spörer and Schwabe (RGO) sunspot positions was $0.25 \pm 3^\circ$ ($-0.2 \pm 2.2^\circ$) for the periods with overlapping data. The data for the butterfly diagram are available at the CDS.

Table 5.1: Latitude parameters (F, H, and L latitudes) as well as wing strength I , listed separately for the two hemispheres (denoted as N and S) and the whole Sun.

Cycle	F(N)	F(S)	F(combined)	H(N)	H(S)	H(combined)	L(N)	L(S)	L(combined)	I (N)	I (S)
7	N/A	N/A	N/A	40.0 ± 1.8	-37.9 ± 1.1	39.1 ± 1.1	5.50 ± 2.0	-3.14 ± 1.3	4.49 ± 1.3	N/A	N/A
8	26.9 ± 3.0	-25.2 ± 2.8	26.0 ± 1.9	47.8 ± 0.7	-43.4 ± 1.4	46.7 ± 0.6	5.42 ± 0.9	-5.94 ± 1.3	6.08 ± 0.9	236	200
9	22.2 ± 1.8	-21.6 ± 2.1	23.3 ± 1.2	41.2 ± 1.8	-34.4 ± 1.1	38.6 ± 1.3	4.23 ± 0.9	-4.31 ± 1.3	4.35 ± 0.8	272	219
10	26.4 ± 2.2	-25.8 ± 1.8	25.8 ± 1.5	35.4 ± 0.8	-39.2 ± 0.5	38.0 ± 0.4	5.04 ± 0.9	-6.12 ± 1.2	5.84 ± 0.8	≥216	≥231
11	26.0 ± 2.3	-25.4 ± 1.5	25.7 ± 1.3	37.4 ± 0.3	-36.3 ± 0.4	36.8 ± 0.2	7.50 ± 1.5	-6.56 ± 1.4	6.28 ± 0.9	N/A	N/A
12	21.1 ± 3.0	-21.2 ± 1.3	21.6 ± 1.5	31.0 ± 0.7	-31.2 ± 0.6	31.0 ± 0.4	6.94 ± 0.8	-6.73 ± 1.0	5.96 ± 0.6	157 (196)	203 (253)
13	24.2 ± 0.9	-27.1 ± 1.5	25.8 ± 0.9	32.5 ± 0.9	-35.4 ± 0.8	34.3 ± 0.6	6.62 ± 1.0	-5.69 ± 0.7	6.41 ± 0.6	232 (255)	275 (302)
14	27.5 ± 1.6	-23.8 ± 1.7	26.5 ± 1.2	35.0 ± 1.1	-32.1 ± 0.4	33.6 ± 0.7	4.21 ± 1.4	-2.00 ± 0.5	2.78 ± 0.7	200	207
15	24.3 ± 1.6	-23.7 ± 1.7	24.0 ± 1.1	39.9 ± 1.5	-38.8 ± 1.7	39.3 ± 1.1	6.22 ± 0.7	-5.72 ± 0.7	6.06 ± 0.4	288	250
16	27.9 ± 1.3	-25.9 ± 1.6	26.5 ± 1.0	36.1 ± 0.8	-34.4 ± 0.6	35.4 ± 0.5	5.17 ± 0.9	-4.63 ± 1.2	5.66 ± 0.8	262	229
17	26.5 ± 1.5	-28.3 ± 0.8	28.0 ± 0.8	38.2 ± 0.8	-35.9 ± 0.5	37.0 ± 0.5	7.96 ± 1.1	-5.94 ± 0.6	6.42 ± 0.5	318	321
18	24.7 ± 1.4	-26.8 ± 1.1	26.5 ± 0.9	36.9 ± 0.9	-39.2 ± 0.5	38.5 ± 0.5	8.72 ± 1.0	-6.02 ± 0.8	7.37 ± 0.7	359	362
19	28.5 ± 1.0	-27.1 ± 1.3	27.7 ± 0.8	44.0 ± 0.5	-41.0 ± 0.6	42.9 ± 0.4	6.05 ± 0.6	-7.12 ± 0.9	6.54 ± 0.5	504	367
20	27.2 ± 1.3	-25.0 ± 1.3	26.7 ± 0.8	38.7 ± 0.5	-38.4 ± 0.9	38.8 ± 0.5	4.58 ± 0.7	-6.35 ± 0.9	5.24 ± 0.6	405	326
21	23.7 ± 1.6	-27.7 ± 1.4	25.8 ± 1.1	40.0 ± 0.5	-39.9 ± 1.2	41.0 ± 0.7	4.42 ± 0.6	-6.42 ± 0.9	5.26 ± 0.5	287	295
22	25.2 ± 1.7	-26.6 ± 1.1	26.0 ± 1.0	42.0 ± 1.7	-40.3 ± 0.8	41.0 ± 0.8	5.64 ± 0.8	-8.41 ± 1.2	6.71 ± 0.8	245	287
23	28.4 ± 1.7	-27.1 ± 1.4	27.6 ± 1.0	40.0 ± 0.8	-41.2 ± 0.9	40.6 ± 0.6	7.07 ± 1.1	-8.19 ± 0.7	8.0 ± 0.6	214	242
24	27.6 ± 2.1	-25.9 ± 2.0	26.5 ± 1.3	37.2 ± 1.4	-33.8 ± 0.7	34.9 ± 0.7	N/A	N/A	N/A	N/A	N/A

Notes. The values of I in parentheses are corrected for the possible inhomogeneity in the RGO dataset.

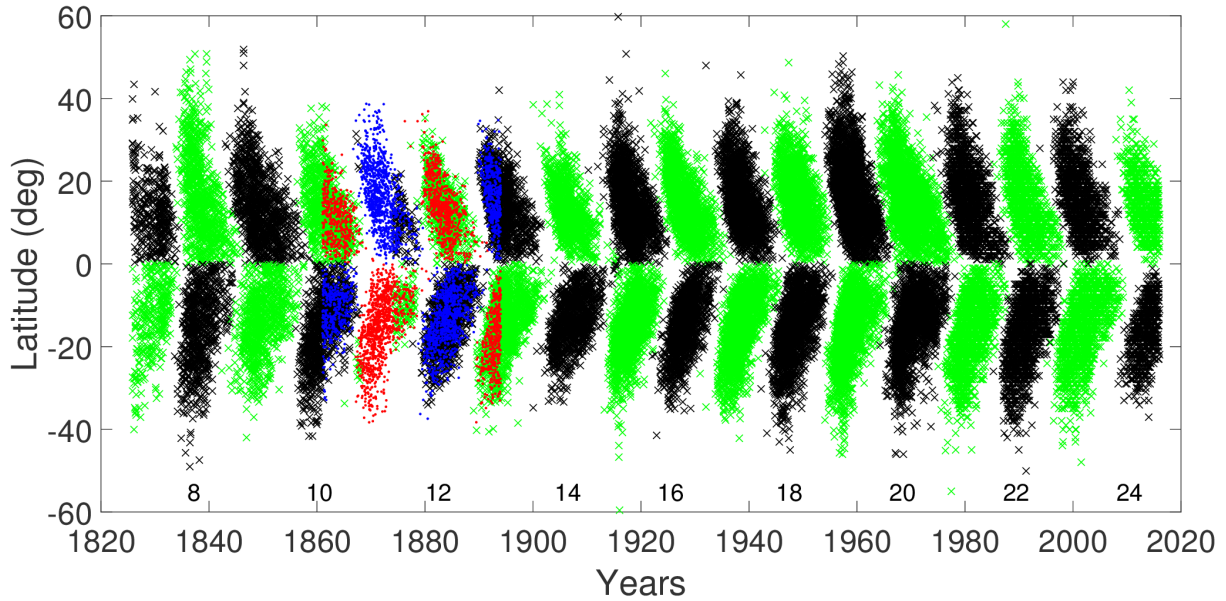


Figure 5.2: Butterfly diagram with individual wings indicated by color, constructed for sunspot groups on their first appearance. The green and black wings are for Schwabe and RGO datasets and the red and blue for Spörer data.

5.3 Evolution of characteristic wing latitudes

Visual inspection of the butterfly wings shown in Fig. 5.2 reveals some typical features of the cycle wings, like Spörer’s law of the decreasing mean latitude of sunspot occurrence during the solar cycle (e.g., Hathaway, 2015). All wings start at mid-latitudes, then quickly spread out, occupying a fairly wide range of latitudes, and finally converge at low latitudes around the equator. Thus, the latitude evolution of each wing can be roughly characterized by three latitudes:

- The latitude at which the first sunspot groups appear, called henceforth the F latitude, defines the latitude where the new wing starts.
- The maximum latitude of sunspot group occurrence in each wing, called the H latitude, defines the greatest latitudinal extent of the wing.
- The latitude at which the last sunspot groups appear, called the L latitude, characterizes the end of the wing. The last groups of the ‘old’ cycle wing may appear later than the first groups of the ‘new’ cycle wing.

Using the individual very first, the highest latitude, or the very last sunspot groups causes the corresponding F, H, and L latitudes (and related times) to be rather arbitrary and prone to large uncertainties. On the other hand, increasing the statistics by considering, for example, the mean latitude of groups during the first year of each wing may dilute some important features. As a compromise between sufficient statistics and exactness of results, we consider the first 1%, the highest-latitude 1% and the last 1% fractions of sunspot groups in each wing to define the F, H and L latitudes, respectively. The 1% percentile typically includes 9–25 sunspot groups per wing, which gives a fairly reliable estimate of the characteristic latitudes. Thus, the F and L latitudes were computed as the mean latitudes and the standard error of the mean (SEM) for the first and last 1% of groups in each wing, and the H latitudes as the mean latitudes of 1% of groups with the highest latitudes (positive for north and negative for south), regardless of the time of their occurrence in the wing. The H latitude groups typically appear within several years after the start of the wing. We checked that varying the percentage of the F, H and L latitude definition using 1.5% or 2% percentiles does not alter the main results.

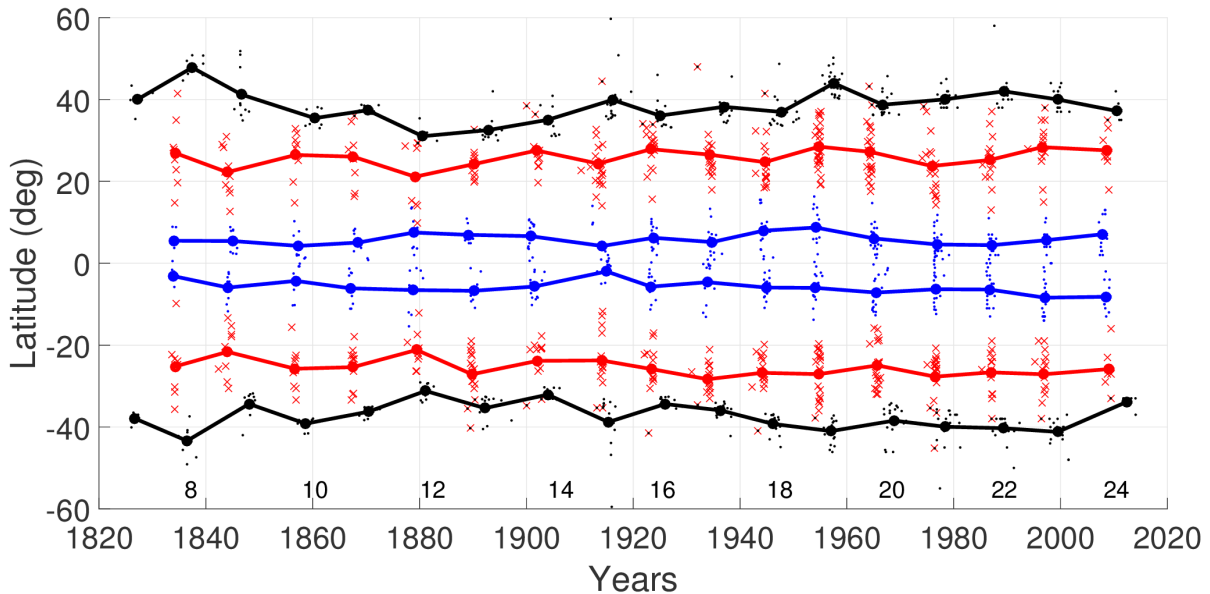


Figure 5.3: Time-latitude diagram of the first 1% (red crosses) and the last 1% groups (blue dots), as well as the highest-latitude 1% of groups (black dots) for each wing separately. The mean F, H and L latitudes are shown by filled circles connected by lines, of the corresponding color.

Figure 5.3 depicts the latitudes and times of the sunspot groups on the first 1% (red), highest latitude 1% (black) and last 1% (blue) along with their mean latitudes (filled circles connected by lines). The so-defined F, H and L latitudes for each wing are shown in Fig. 5.4 along with their SEM errors. The F, H and L latitudes are also collected in Table 5.1 along with their SEM values, separately for each hemisphere and for the whole Sun (the two hemispheres combined). Some parameters for some wings cannot be defined because the dataset is incomplete:

- The very beginning of cycle 7 was not observed by Schwabe, making it impossible to define the F latitudes of this cycle, while we can still define the H and L latitudes.
- Since cycle 24 is not yet completed at the time of writing this paper, the L latitudes of this cycle cannot be defined.

Figure 5.4 shows that the F latitudes appear in a latitudinal band of about 20° – 30° without a significant variation or trend during the centennial evolution. F latitudes during the first half of the period are slightly lower, on average, than those for the latter half, but this difference is not statistically significant. The F latitudes of the two hemispheres are significantly (p -value 0.03) correlated (Pearson’s correlation coefficient is $0.52^{+0.16}_{-0.22}$), including the dips for cycles 9 and 12. The L latitudes are limited to the band of 2° – 10° . They do not depict a clear pattern either, while the variability is fairly well synchronized between the two hemispheres ($c = 0.4^{+0.2}_{-0.24}$, $p = 0.1$).

However, the evolution of the H latitudes depicts a clear centennial oscillation: fairly systematic decrease of H latitudes in both hemispheres from cycle 7 to the all-time minimum in cycle 12, followed by a rise with the maximum during cycles 19–22, turning to a new decrease thereafter. This evolution closely follows the overall trend of solar activity. The two hemispheres depict synchronous variations, with a highly significant ($p < 3 \times 10^{-4}$) correlation ($c = 0.75^{+0.09}_{-0.13}$) between the hemispheres. We note that the values of the H latitudes for the early Schwabe data (cycles 7–8) are probably slightly too high due to enhanced uncertainty in the high-latitude determination at that time (Arlt *et al.*, 2013). The centennial variability of H latitudes during the most credible period (cycles 9–24) is about 15° (30° – 45°). The early Schwabe data remains within this range except for one wing.

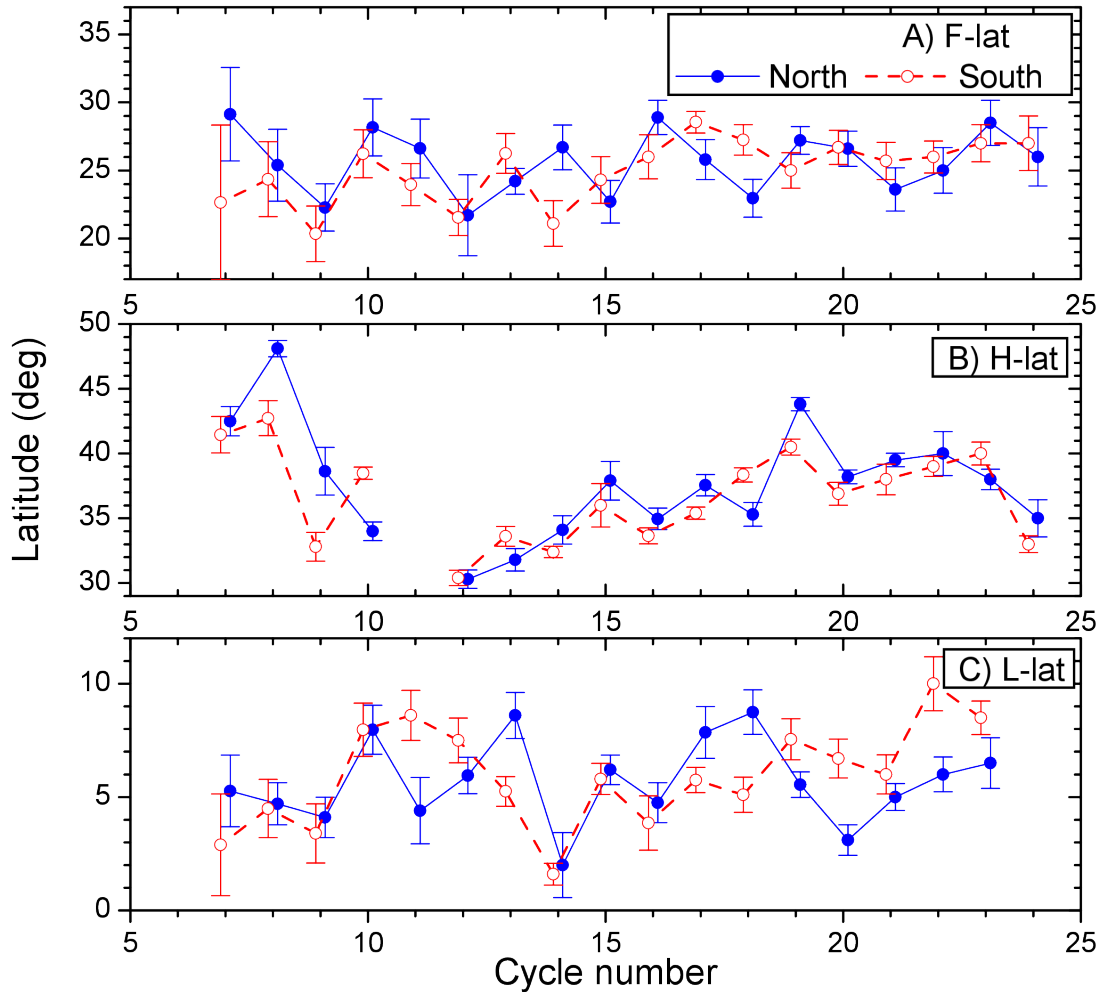


Figure 5.4: Panel (a): Mean latitude and its standard error of the first 1% spots of each wing (F latitudes). Panel (b): Mean latitude and its standard error, of the highest 1% spots of each wing (H latitudes). Panel (c): Mean latitude and its standard error of the last 1% spots of each wing (L latitudes). Data for the North and South hemispheres are shown in blue and red (slightly offset horizontally for better visibility), respectively.

The fact that the two hemispheres depict synchronous variations for all the three characteristic latitudes suggests that these parameters are representative of the latitudinal evolution of the wings, reflect real physical processes of sunspot formation, and are not dominated by noise.

5.4 Relation to wing strength

We have compared the cycle-to-cycle variation of the characteristic wing latitudes with the wing strengths. As the wing strength we considered, similarly to [Leussu *et al.* \(2016\)](#), the total sum I of monthly mean numbers of all the sunspot groups (not only the first occurrence) over that wing, using Schwabe and RGO data. The strengths are given in [Table 5.1](#) and [Fig. 5.5](#). The strength series may be not fully homogeneous since there might be an inhomogeneity in the earlier part of the RGO and Schwabe series in the sense of group numbers, and the intensity cannot be directly computed for Spörer data. For the former, we also present corrected strengths for solar cycles 12 and 13 (see [Sect. 5.1](#) for details).

[Figure 5.6](#) depicts scatter plots for the F, H and L latitudes as function of the wing strength in panels (a) to (c), respectively.

Linear correlation coefficients between the characteristic latitudes and wing strengths are listed in [Table 5.2](#). Only cycles 12 through 23 based on the RGO series were used because of a possible inhomogeneity between Schwabe and RGO data. Including the Schwabe data does

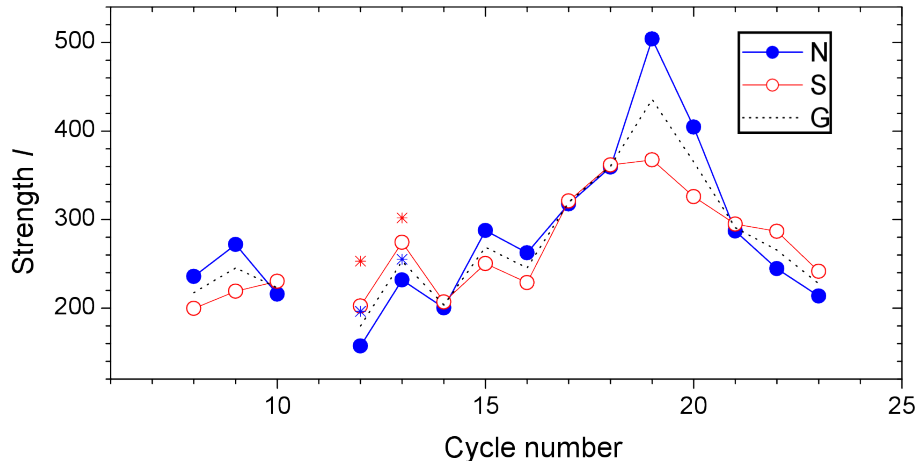


Figure 5.5: Strength of cycle wings separately for N and S hemispheres, as indicated in the legend. The mean of the two hemispheres is shown as the dashed “G” curve. The asterisks depict the strengths of cycles 12 and 13 corrected for a possible inhomogeneity of the RGO data (see Sect. 5.1)

Table 5.2: Linear correlation coefficients between F, H and L latitudes and the wing strength for cycles 12–23, separately for each hemisphere (N and S), and for the combined hemispheres. p -values for the correlation coefficients are given in parentheses (“ins” means insignificant).

Group	N	S	Combined
F lat	$0.42^{+0.23}_{-0.3}$ (ins)	$0.63^{+0.16}_{-0.25}$ (0.03)	$0.54^{+0.19}_{-0.25}$ (0.07)
H lat	$0.7^{+0.14}_{-0.2}$ (0.01)	$0.68^{+0.14}_{-0.2}$ (0.015)	$0.66^{+0.14}_{-0.21}$ (0.02)
L lat	0.1 ± 0.3 (ins)	0.25 ± 0.3 (ins)	0.26 ± 0.3 (ins)

not alter qualitatively the results for F and L latitudes, but weakens the correlation for the H latitudes because of the relatively higher values of the latitudes (see the discussion above).

Figure 5.6 shows a clear tendency that the H latitudes are related to the wing strength with high statistical confidence, better than 0.02. We have checked that this tendency remains robust independently of the exact percentile of the definition of characteristic latitudes: for example, the correlation between the wing strengths and the H latitudes, defined using the 2% percentile of sunspot groups, is $0.66^{+0.14}_{-0.21}$ ($p = 0.02$) for both N and S hemispheres (cf. Table 5.2). This implies that the latitudinal extent of the wings is quite robustly related to the strength of the corresponding hemispheric wing, as shown earlier by Jiang *et al.* (2011b) for full cycles. On the other hand, because of the great scatter of points in Fig. 5.6b, this relation has little predictive power but only indicates a statistical tendency. The L latitudes depict no dependency on the wing strength. The situation is uncertain with the F latitudes. The correlation with the wing strength is statistically significant for the southern hemisphere, but insignificant for the northern hemisphere.

We also calculated the characteristic latitudes for combined N and S wings with unsigned latitudes. While the strength of these combined wings of the cycles is simply the sum of the hemispheric wing strengths, the characteristic latitudes need to be recalculated. We therefore computed the combined F, H and L latitudes in the same way as for the individual wings, but using unsigned latitudes without separating the hemispheres. Figure 5.7 depicts the time evolution of the combined F, H and L latitudes for combined wings. The corresponding latitudes are denoted in Table 5.1 as “combined” and the correlations are shown in the last column of Table 5.2. While the combined correlations for the H and L latitudes are entirely consistent with those for separated wings (highly significant and insignificant, respectively), the correlation is marginally significant for the F latitudes.

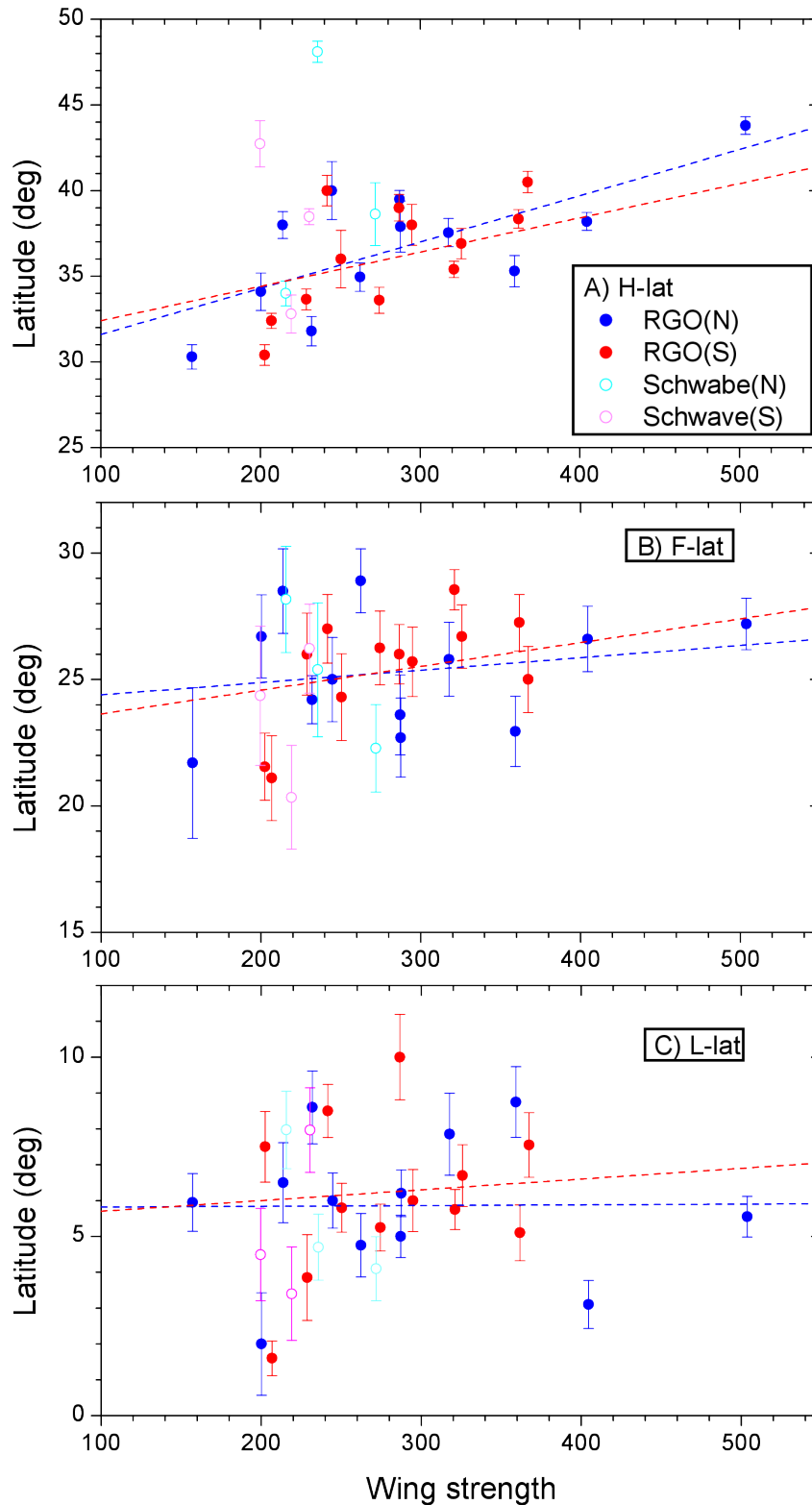


Figure 5.6: Relation between the wing strength (the cumulative sum of the monthly numbers of sunspot groups) and the F, H and L latitudes, in panels (a) to (c) respectively, separately for the two datasets (RGO and Schwabe) and the two hemispheres, as denoted in the legend of panel (a). The blue and red dotted lines depict the best-fit linear trends for the N and S hemispheres, respectively, using the RGO data.

We also repeated the analysis using the corrected strengths for solar cycles 12 and 13. The tendency remains solid with slightly smaller correlation coefficients. The only change is that the correlation for the F latitudes and combined hemispheres becomes insignificant ($0.42^{+0.22}_{-0.31}$, $p = 0.17$), all other relations remain qualitatively the same.

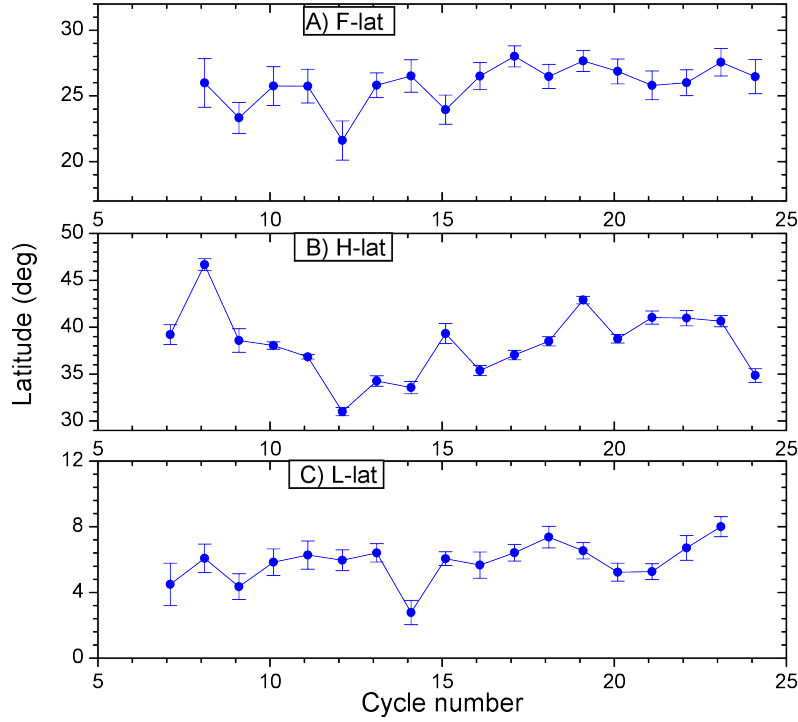


Figure 5.7: F, H and L latitudes for the combined hemispheres, with 1σ standard errors.

Table 5.3: Dates of the start and end of each wing defined as the mean time of the first (last) 1% percentile of sunspot groups in the N and S hemispheres, respectively.

Cycle	start(N)	start(S)	end(N)	end(S)
7	N/A	N/A	1834.01	1833.95
8	1834.35	1834.26	1845.11	1844.17
9	1843.98	1844.05	1857.33	1856.85
10	1856.82	1856.65	1868.50	1867.14
11	1867.57	1867.52	1878.93	1878.83
12	1879.18	1879.46	1889.14	1890.16
13	1890.19	1889.83	1900.78	1901.53
14	1901.93	1902.08	1914.18	1915.01
15	1913.48	1914.12	1923.86	1923.35
16	1923.35	1923.42	1934.77	1933.85
17	1934.27	1933.94	1944.39	1944.96
18	1944.61	1944.10	1954.20	1954.12
19	1954.80	1954.77	1965.10	1965.55
20	1964.35	1965.67	1976.90	1976.64
21	1975.93	1976.50	1987.17	1986.73
22	1986.75	1986.96	1997.39	1997.04
23	1996.53	1996.81	2007.84	2008.57
24	2008.65	2009.02	N/A	N/A

5.5 Wing lengths, overlaps and asymmetries

We define the start and end times of the wings as the mean time of the first and last 1% percentile sunspot group occurrence, respectively. These times are listed in Table 5.3.

From the start and end dates we calculated the time spans of the wings, as shown in Fig. 5.8. We note that our definition is different from the traditional cycle length determination between consecutive cycle minima of (total) sunspot activity. There is a quasi-periodicity with a time

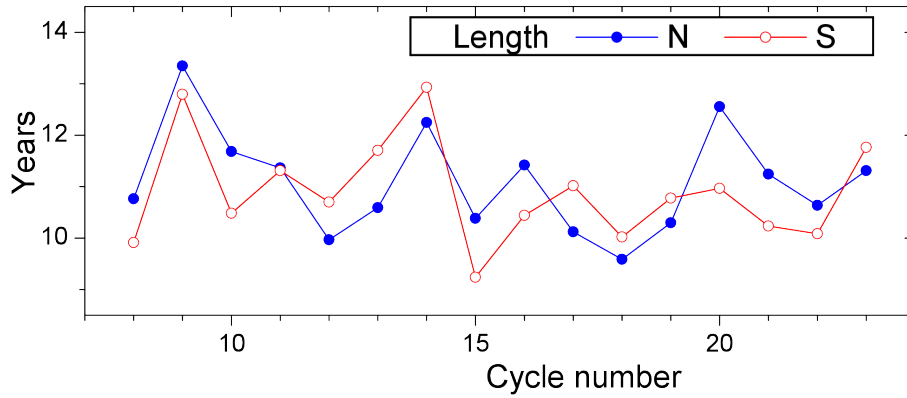


Figure 5.8: Total lengths of hemispheric wings separately for northern (blue) and southern (red) hemispheres. The uncertainties are typically within a few months.

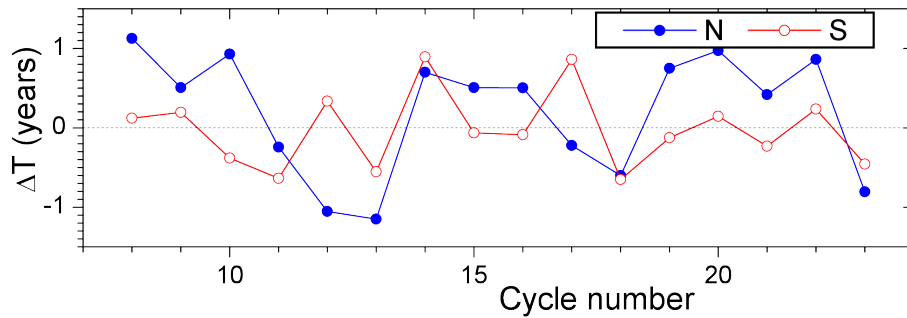


Figure 5.9: Time difference between the end of the wing of one cycle and the start of the next cycle wing. Positive values correspond to overlaps between the wings, negative values to gaps.

scale of about 5–6 cycles, which is more pronounced in the northern hemisphere than in the southern hemisphere.

Figure 5.9 shows the overlaps and gaps between the wings, defined as the difference between the end time of one wing and the start time of the next wing in the same hemisphere. Accordingly, positive difference implies an overlap (sunspot groups of the new cycle appear before the old cycle ends), and negative difference indicates a gap. Figure 5.9 depicts both (negative) time gaps and (positive) overlaps between the wings of typically within about one year, occasionally slightly longer. These time differences in the S hemisphere remain somewhat smaller than in the north, and their overall mean is close to zero. However, in the north, they vary considerably, and on average there is a (2–3)-month overlap. Moreover, the time differences in the N hemisphere depict a clear (5–6)-cycle quasi-periodicity, obviously roughly in phase with the wing length. Thus, longer wings are typically overlapping with each other, while shorter wings are more separated from each other. No distinguishable periodicity is found for the S hemisphere.

Figure 5.10 shows the time difference in the start and end times between the two hemispheres (north minus south). Overall, there is more variability in the hemispheric differences for the end times than for the start times. Both differences are within about 1.5 years. There is an anticorrelation in the start and end times. This implies that a wing that starts earlier tends to end slightly later and has a longer overall length.

Finally, we studied the hemispheric asymmetry of the start and end latitudes. The asymmetry is defined as the difference in the mean F and L latitudes between the N and S wings of the same cycles (see Table 5.1). These asymmetries are shown in Fig. 5.11. Overall, they are clearly quite symmetric (the mean value is about zero), but there is an oscillation with the duration of about ten cycles in the end latitudes (panel b). However, this is only marginally significant (p -value 0.09).

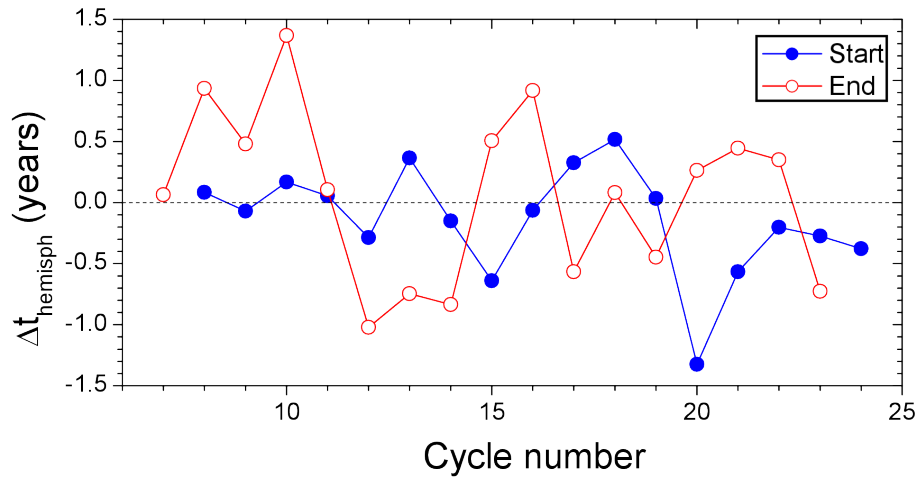


Figure 5.10: Difference between the timing of the start (blue) and end (red) of each wing (see Table 5.3).

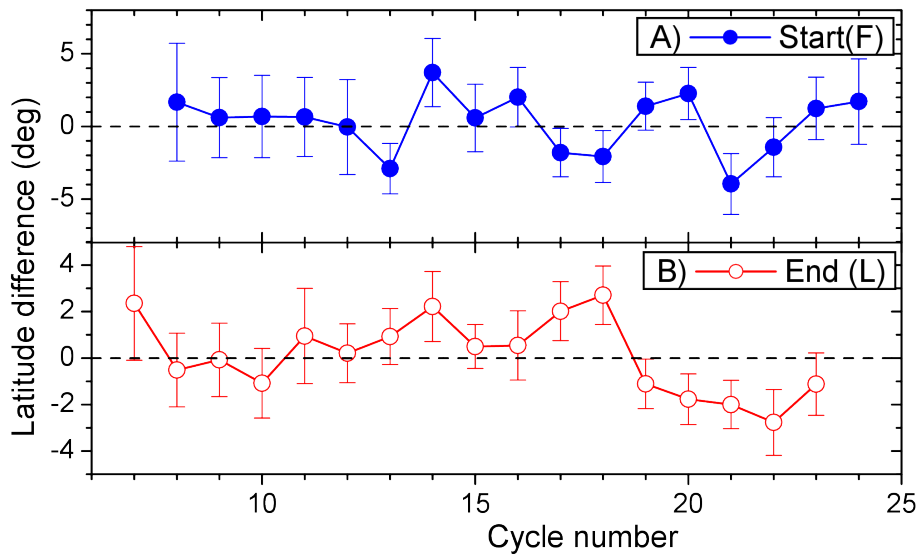


Figure 5.11: Difference between the mean latitudes of the start (F latitudes, blue) and end (L latitudes, red) of each wing (see Table 5.1).

5.6 Summary

We presented a butterfly diagram of sunspot group occurrences for the first time continuously since 1826, using three subsets of sunspot group occurrence: an updated analysis of solar drawings from Schwabe (1826–1867), newly digitized data of solar drawings by Spörer (1866–1880), and data from photographic images of the RGO since 1875, extended by SOON-network data after 1976. Only the first appearance of each sunspot group was considered.

We performed a full separation of the butterfly wings, using the method developed by [Leussu et al. \(2016\)](#), so that each sunspot group was uniquely ascribed to a wing (solar cycle and hemisphere) of the butterfly diagram. A digital database is available in the CDS.

Using the new database, we have analyzed the characteristic latitudes, corresponding to the start, end, and the latitudinal extent of the wings and their times. We found that the two hemispheres depict synchronous variations in all the three latitudes, implying that they are representative of the latitudinal evolution of the wings, reflect real physical processes of sunspot formation and are not dominated by noise. This also implies a fairly strong interconnection between the two solar hemispheres.

We found that the first (1%) sunspot groups occur in each wing (F latitudes) at moderate latitudes of 20° – 30° . The F latitudes depict a marginal tendency, especially in the S hemisphere, to follow the wing strength (quantified by the total sum of the monthly numbers of sunspot groups). The H latitudes (1% of the groups occurring at the highest latitudes) are significantly (about 10°) higher than the F latitudes and vary greatly over 30° – 45° . They are significantly correlated with the wing strength during the period covered by the RGO data (cycles 12–23). Including data from Schwabe weakens the relation because of possibly less reliable identification of high-latitude spots (see Sect. 5.1). The mean latitudes of the last 1% of sunspot groups (L latitudes) vary within 2° – 10° and show no clear relation to the wing strength. Stronger cycle wings tend to start at higher latitudes and to have a greater latitudinal extent. This confirms earlier results from [Jiang et al. \(2011b\)](#), for example, that stronger cycles tend to have a greater latitudinal extent, which has been found previously for solar cycles and is now generalized for the hemispheric wings.

We discussed uncertainties and robustness of the conclusions, in particular with respect to the possible inhomogeneity of the RGO dataset before 1900.

We also performed a first analysis of the timing of the butterfly wings. We found that the longer hemispheric wings always end later and also mostly start earlier than the shorter wings. Although on average there is no gap between two successive wings of the southern hemisphere (the new wing starts at the time that the old wing ends), there is an overall average overlap of 2–3 months between the successive wings in the northern hemisphere. Moreover, we found a (5–6)-cycle oscillation in the overlap or gap of wings in the north. The northern hemisphere also exhibits a (5–6)-cycle oscillation in the wing length. We also noted a marginally significant oscillation with a period of about ten cycles in the hemispheric asymmetry of the L latitudes.

Although we only presented here a basic analysis, the new long database of butterfly wings provides new observational constraints to solar dynamo models that discuss the spatio-temporal distribution of sunspot occurrence over the solar cycle and longer. It opens a possibility for detailed focused studies such as “active latitudes” and their drifts over solar cycles ([Kilcik et al., 2016](#)).

Chapter 6

Conclusions

Historical sunspot drawings and data, which cover the parts of the 17th to 19th centuries, were analyzed to study the properties of earlier solar cycles. The long-term study included tilt angles of sunspot groups and the butterfly diagram. Their relation to solar activity was studied and deciphered yielding several important results are described below.

Sunspot observations recorded by Samuel Heinrich Schwabe during 1825–1867 cover solar cycles 7–10. Sunspot positions and sizes from those drawings were extracted by [Arlt *et al.* \(2013\)](#). As drawings were not made to scale, a direct conversion of sunspot sizes into areas was not carried out. Instead, the area values were calculated in this thesis through a statistical comparison with 20th century data. The umbral areas were calculated only for spots with heliographic positions and located within 85° from the disk center, and they constitute 133 496 umbrae. The distribution of umbral areas is fitted by a log-normal distribution and match contemporary distribution based on 20th century data ([Bogdan *et al.*, 1988](#)). The area distributions for different phases of solar cycles, i.e., maxima, minima, ascending, and descending phases, are proportional to the combined area distribution. Hence, the log-normal distribution of areas is independent of the phases of a solar cycle, which is observed also in 20th century data. The groups defined by Schwabe often contained clusters of sunspot groups, which are different from the current definition of a sunspot group. The regrouping of sunspot groups was implemented through the investigation of the evolution of sunspot groups in clusters. The tilt angles and polarity separations of sunspot groups were then calculated. The tilt angles of unipolar groups add noise to tilt angle studies, and so they should be excluded. The condition of groups with polarity separations greater than 3° ([Baranyi, 2015](#)) was used to select the “supposed” bipolar groups. The mean tilt angle for supposedly bipolar groups is $4.45^\circ \pm 0.20^\circ$. The bipolar groups obey Joy’s law, and their latitudinal dependence is the same as in the 20th century data. A method to exclude misclassified unipolar groups in the Schwabe data with the above condition is discussed in this thesis. It is based on the analysis of changes in the tilt angles of a group at each of their instances across the solar disk. The additional selection of bipolar groups by this method increases the mean tilt angle to $5.85^\circ \pm 0.25^\circ$.

Scrutinizing sunspot drawings by Christoph Scheiner and his colleagues yielded umbral areas of 8167 sunspots during 1611–1631. However, the heliographic positions could be measured for 8152 sunspots. This data covers solar cycle numbers –13 and –12. The data contains almost continuous data for the years 1625, 1626, 1627, and 1629, while they contain only for a few days during the years of 1611, 1612, 1618, 1621, 1622, 1623, 1624, and 1631. The quality of sunspot drawings is very good starting in 1618 and delivers a positional accuracy of about 1°–2°. Before 1618, however, the drawings are extremely coarse and show highly exaggerated sizes of sunspot groups. From the manual investigation of the drawings of the entire period, 697 sunspot groups were classified as bipolar group instances, and tilt angles were calculated for them, which provided a mean tilt of $3.84^\circ \pm 0.83^\circ$.

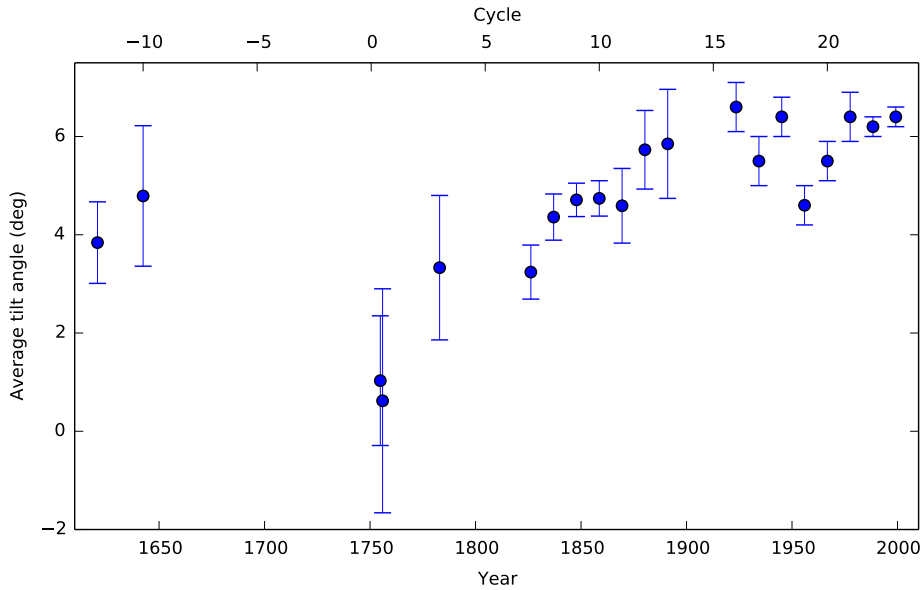


Figure 6.1: The cycle-averaged tilt angles of solar cycles from our analysis of historical sunspot drawings and from modern data. The cycle-averaged tilt angle values for solar cycles 16–23 are taken from Wang *et al.* (2015)

With the Schwabe and Scheiner data, tilt angles of sunspot groups are now available for earlier solar cycles. Sunspot data for some other earlier solar cycles were extracted from drawings of Johann Caspar Staudacher by Arlt (2009), Ludovico Zucconi by Cristo, Vaquero, and Sánchez-Bajo (2011), and Friedrich Wilhelm Gustav Spörer by Diercke, Arlt, and Denker (2015). The calculation of tilt angles for sunspot groups in those data was carried out in this thesis. The sunspot data were also extracted from drawings by Johannes Hevelius, and tilt angles of sunspot groups were calculated as part of this thesis. The manual selection of bipolar groups was carried out for the Zucconi and Hevelius data as it was executed for the Scheiner data. There is an enormous number of sunspot groups in Staudacher and Spörer, so the manual selection of bipolar groups could not be executed. The condition of selecting bipolar groups with polarity separations greater than 3° was used as in the Schwabe data. The Scheiner and Hevelius data belong to the pre-Maunder minimum period, and in particular the Hevelius data are fascinating, as they cover part of a solar cycle just before the Maunder minimum. Hence, the study of cycle-averaged tilt angles over earlier centuries and a comparison with the cycle-averaged tilt angles from the 20th century was carried out. Cycle-averaged tilt angles from earlier solar cycles, except for cycles 0 and 1, are not very different compared to the values from modern data including pre-Maunder minimum values from Hevelius and Scheiner. The decrease of the cycle-averaged tilt angle is one of the hypothesis leading to a weaker activity in the Maunder minimum, but it is not seen in our data. The Hevelius data belong to the maximum phase of the solar cycle -10 , according to the group sunspot number Hoyt and Schatten (1998), but they are located slightly closer to the equator than what would be expected for that phase of a cycle. Figure 6.1 shows that the cycle-averaged tilt angle for cycles 0 and 1 is the lowest of all solar cycles, which covers a period starting about 50 years after the Maunder minimum. The lowest cycle-averaged tilt angle is evident in two independent data sets from Staudacher and Zucconi and as such, it is soundly established.

The extension of the butterfly diagram into the past till 1826 was achieved with the sunspot position data from Schwabe’s and Spörer’s drawings. The systematic grouping of sunspot groups to a certain cycle wing was carried out with the method developed by Leussu *et al.* (2016). In this method, the gaps created by the absence of sunspot groups in latitudinal bands were used to divide between the cycles, instead of using a particular time dividing solar cycles at all latitudes. Finally all individual ‘butterfly wings’ were separated using this cyclic plus hemispheric information. The first 1% of start, highest, and end latitudes of the first occurrences of groups define the F, H, and L latitudes. Those latitudes and their correlation with the strength of the wings

were studied. The F, H, and L latitudes vary over 20° – 30° , 30° – 45° , and 2° – 10° , respectively. The F, H, and L latitudes exhibit a marginal, strong, and no correlation with the wing strength, respectively. The correlations of H and L latitudes with wing strength were the same for the whole Sun and hemispheres separately. However, the F latitude shows a statistically significant correlation with wing strength for the southern hemisphere and an insignificant correlation for the northern hemisphere, which becomes marginally significant for the whole Sun. The strong correlation of the latitudinal extent (H latitudes) of wings with the strength of solar cycle is evident in both hemisphere wings and the whole Sun as noted earlier by [Jiang *et al.* \(2011b\)](#) for the whole Sun. A centennial oscillation of the H latitudes is also clearly seen. The time spans of wings, which are calculated from the difference between the mean F and L latitudes, show a quasi-periodicity of about 5–6 cycles. The gaps/overlaps of successive wings in the northern hemisphere also exhibit a quasi-periodicity of 5–6 cycles. A wing, which starts earlier, tends to end later exhibiting an anticorrelation. The asymmetry between the mean F and L latitudes of wings from two hemispheres were studied and an overall symmetry was detected. However, an oscillation with a period of 10 cycles is seen in the end-latitudes.

The above results show that the long-term study of solar cycle properties is helpful in constraining solar dynamo models and in predicting solar activity. The reliability of the data extracted from the historical sunspot drawings is amazing, so the historical sunspot observations are really a treasure for solar physics research.

Chapter 7

Outlook

Reconstruction of the solar surface magnetic field. The surface magnetic field of the Sun can be reconstructed approximately for earlier centuries if any parameters of solar activity, for example, sunspot number or sunspot positions and areas, are known as a function of time. A reconstruction for the period 1826–1867 was attempted using the Schwabe data with the Surface Flux Transport Model (SFTM) code developed at the Max Planck Institute for Solar System Research (MPS).

The SFTM is a two-dimensional flux transport model, which simulates the evolution of the radial component of the large-scale magnetic field on the solar surface. The simulation is carried out under the influence of differential rotation, meridional flow, a surface diffusivity because of granular and supergranular flows acting as a turbulent diffusion, and a slow radial diffusion due to the same turbulence (DeVore, Boris, and Sheeley, 1984; Sheeley, DeVore, and Boris, 1985; Wang, Nash, and Sheeley, 1989b; Mackay, Gaizauskas, and van Ballegooijen, 2000; Schrijver, DeRosa, and Title, 2002; Baumann *et al.*, 2004; Baumann, Schmitt, and Schüssler, 2006).

The evolution of the radial magnetic field in SFTM is governed by

$$\begin{aligned} \frac{\partial B_r}{\partial t} = & -\Omega(\theta) \frac{\partial B_r}{\partial \phi} - \frac{1}{R_\odot \sin \theta} \frac{\partial}{\partial \theta} \left[v(\theta) B_r \sin \theta \right] \\ & + \eta_H \left[\frac{1}{R_\odot^2 \sin \theta} \frac{\partial}{\partial \theta} \left(\sin \theta \frac{\partial B_r}{\partial \theta} \right) + \frac{1}{R_\odot^2 \sin^2 \theta} \frac{\partial^2 B_r}{\partial \phi^2} \right] + S(\theta, \phi, t, A_R) - D(\eta_r), \end{aligned} \quad (7.1)$$

where A_R is the total area of an active region. A surface turbulent diffusivity of $\eta_H = 250 \times 10^6 \text{ m}^2/\text{s}$, which is in the range of the observed values (Schrijver and Martin, 1990; Jafarzadeh *et al.*, 2014), was used in the simulation. The time-averaged differential rotation profile of $\Omega(\lambda) = 13.38 - 2.30 \sin^2 \lambda - 1.62 \sin^4 \lambda$ (in $^\circ/\text{day}$) given by Snodgrass (1983) was used. The time-averaged meridional flow profile determined by van Ballegooijen, Cartledge, and Priest (1998), which is $11 \sin(2.44\lambda) \text{ m/s}$ for $|\lambda| \leq 75^\circ$ and 0 beyond that latitude, was included in the simulation.

The Greenwich/USAF data were used in the reconstruction of the surface magnetic field for solar cycles 15–21, which contain only locations and areas of sunspot groups but no information about individual sunspots. Tilt angles and polarity separations of sunspot groups are not available in these data. Cameron *et al.* (2010) used Mt. Wilson and Kodaikanal data, which cover part of the earlier data sets, to derive suitable relations for tilt angles and polarity separations as functions of sunspot group locations and areas. Then polarity separations and tilt angles of sunspot groups in Greenwich/USAF data were calculated using the derived relations.

The polarity separations d and active region areas A_R are related by

$$d = 0.45\sqrt{A_R}. \quad (7.2)$$

The tilt angles were calculated as a function of latitudes of sunspot groups and a constant for each cycle, which were derived using group areas, tilt angles and latitudes of groups from Mt. Wilson and Kodaikanal data. Tilt angles of sunspot groups were scaled down to 0.7 to account for their reduction by the near-surface inflows toward active regions (Gizon, Birch, and Spruit, 2010) and for uncertainty in the tilt angle calculation because of the unavailability of magnetic information about polarities (Cameron *et al.*, 2010).

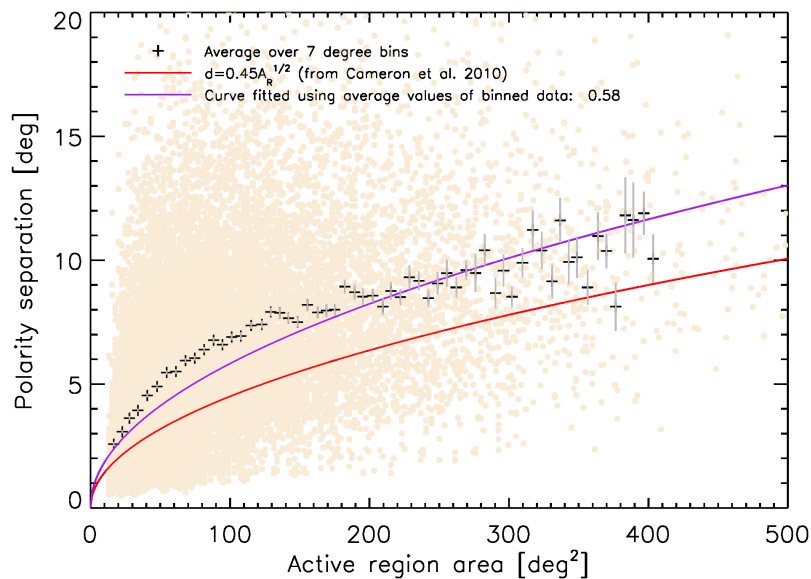


Figure 7.1: Polarity separation as a function of total area of the active region. The red curve is the fit of $d = 0.45\sqrt{A_R}$ from Kodaikanal and Mt. Wilson data (Cameron *et al.*, 2010). The purple curve is the fit over mean values of 7° bins from the Schwabe data. Errors of the means are the standard deviation of the bin sample divided by the square root of number of data in each bin.

Active region areas comprise dark sunspots and bright faculae or plages, so they are larger than sunspot group areas. Mt. Wilson and Kodaikanal data sets contain umbral area of sunspot groups. To convert that into A_R , umbral areas of sunspot groups are converted into whole spot areas ($A_s = \text{umbral} + \text{penumbral area}$) using the results of Brandt, Schmidt, and Steinegger (1990) and then into total areas of active regions using the observed relation by Chapman, Cookson, and Dobias (1997)

$$A_R = A_s + A_p = A_s + 414 + 21A_s - 0.0036A_s^2, \quad (7.3)$$

where A_p is the area covered by plage. Hence, either polarity separations or active region areas can be used as input. In the SFTM code, polarity separations are fed as input.

On the one hand, the radial diffusivity term η_r was introduced by Baumann, Schmitt, and Schüssler (2006) to obtain regular reversals of polar fields for cycles with varying amplitude, without including variations of the meridional flow. On the other hand, while reconstructing the surface magnetic field for solar cycles 15–21, Cameron *et al.* (2010) used tilt angles, which included variations depending on the cycle-averaged properties, instead of the radial diffusivity so $\eta_r = 0$. The authors could reproduce the reversal timings of the polar fields matching the polar reversals derived from $H\alpha$ polar filament observations by Makarov, Tlatov, and Sivaraman (2003).

The magnetic information about the sunspots are not available in the Schwabe data, so the locations of magnetic polarities are calculated using the group properties as explained in [Cameron *et al.* \(2010\)](#). The strength of active regions B_{\max} is a term in the calculation of the initial distribution of the radial field of a BMR. For the reconstruction of solar cycles 15–21, the value of B_{\max} was taken as 374 G, which could simulate magnetic fields comparable to the observed magnetic field (refer to Figure 4 in [Cameron *et al.*, 2010](#)). The same value of $B_{\max} = 374$ G is used in our simulation. However, this value is not an observed value and not certain, so the results using other values need to be compared.

In the reconstruction using the Schwabe data, the observed polarity separations were fed as input and active region areas were calculated using the Equation 7.2. This generated very high polar fields which did not reverse during the cycles. The reason for this behaviour is that is the relation between d and A_R in the Schwabe data differs from that of the Mt. Wilson and Kodaikanal data. The relation curve of d versus A_R from Schwabe data lies above the curve from Mt. Wilson and Kodaikanal data as shown in Fig. 7.1. This could be either due to larger polarity separations or smaller umbral area values.

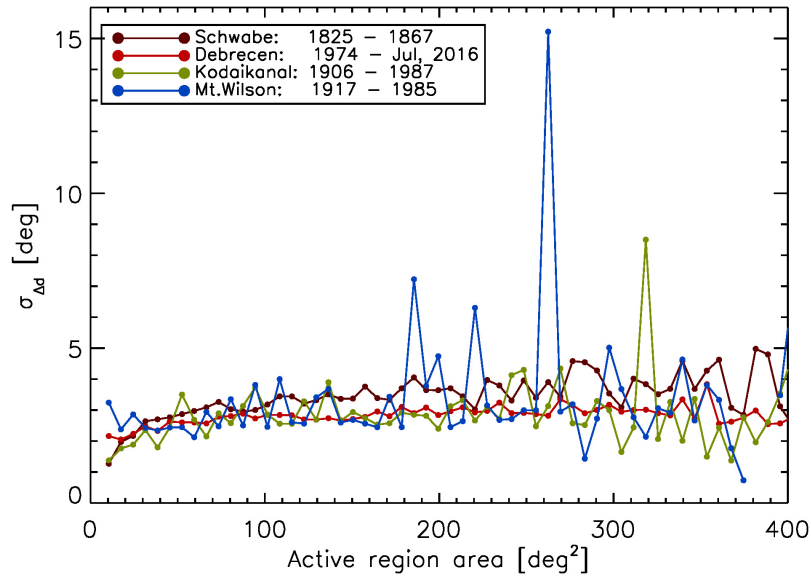


Figure 7.2: The standard deviation of polarity separations of sunspot groups calculated in active region area bins of 7° .

To compare the polarity separations of sunspot groups from the Schwabe data with other data, standard deviations of polarity separations in area bins of 7° were calculated for Schwabe, Debrecen (1974–2016), Kodaikanal (1906–1987), and Mt. Wilson (1917–1985) data. Figure 7.2 shows that the scatters in polarity separations of the Schwabe data do not seem to differ largely compared to other data sets, which indicates that errors in Schwabe data are not much bigger than in other data sets. Alternatively, the group area values may be too small because of: (1) missing of few small spots and pores in groups with many small spots (refer to Sect. 2.4), (2) assignation of relatively smaller values to bigger spots resulted from statistical comparison (refer to Sect. 2.1), and (3) the lowest spot area observed through Schwabe’s telescope may not have been 1 MSH but larger than that. The comparison of one-to-one spot areas from Schwabe and Sestini (refer to Sects. 2.1.3 and 2.1.4) shows that the Schwabe area values are smaller. However, increasing the Schwabe area values leads to a deviation in the area distribution curve from the distribution exhibited by the 20th century data. A simple offset of 10 MSH to each umbral area would in fact produce the Equation 7.2 with a factor of 0.44 instead of 0.45. From Fig. 7.1, it can also be seen that the deviation is more pronounced for the smaller group areas, whereas the bigger group areas converge towards the red line with a factor of 0.45.

The error in grouping of sunspots may also lead to larger polarity separations so an automatic grouping method, which is similar to the method described in Howard, Gilman, and Gilman (1984), was tried. The factor between d and A_R decreases from 0.58, but still higher than 0.45. Perhaps the discrepancy lies in the method, which is yet to be resolved. Hence, several factors seem to contribute to the deviation seen in the relation between d and A_R .

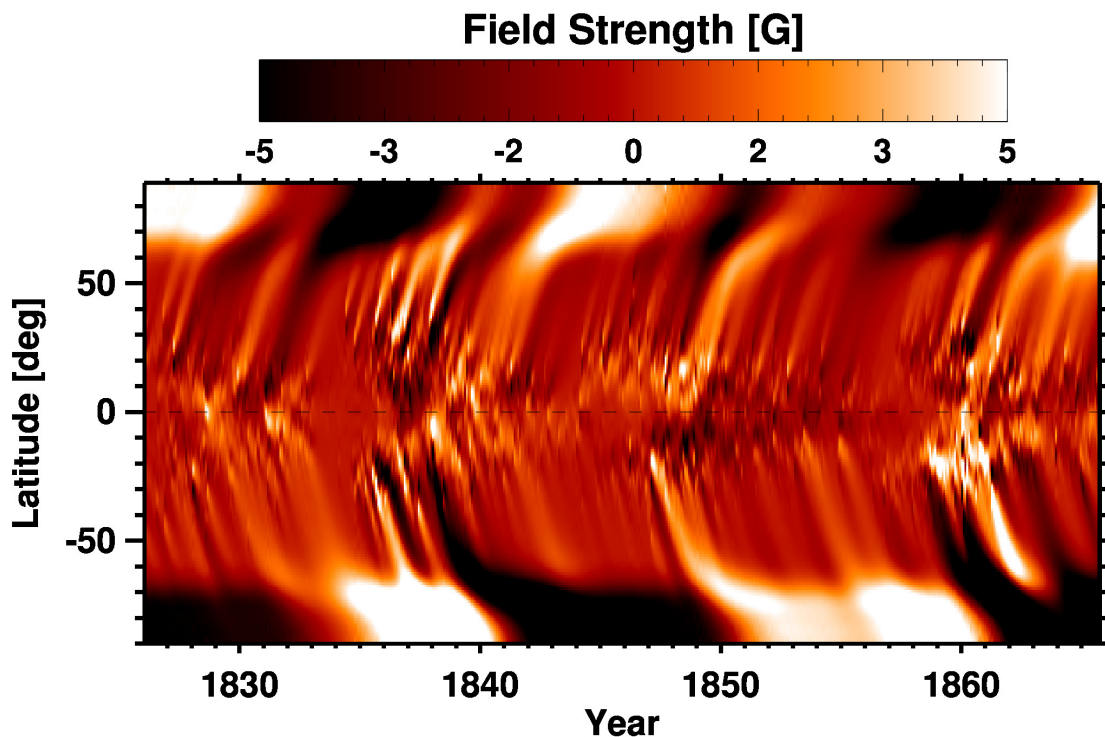


Figure 7.3: Simulated magnetic butterfly diagram for the period 1826–1867 using the Schwabe data. The input for the simulation are tilt angles, polarity separations, and areas of active regions (derived from umbral group areas).

The SFTM was modified to include A_R as the input. Hence, the source term includes the total area of active regions along with the calculated latitudes and longitudes of the polarities, the observed polarity separations, and the times of their maximum area. With the inclusion of A_R , the polar field reversals for the cycles are produced in the simulation as shown in Fig. 7.3. However, the relation between area values and polarity separations needs to be analyzed in detail to sort out the above problem. Once that problem is resolved, the simulation results can be used to study the relation between polar fields and the strength of subsequent solar cycles, which will be interesting. The open flux and solar irradiance for that period can be inferred, which have many applications in solar-terrestrial relation studies. Using the Schwabe and Spörer data, a continuous magnetic butterfly diagram, which is a combination of a simulated one for the past centuries and an observation based one for the recent decades, can be obtained since 1826. A study of the relation between tilt angles and the strengths of subsequent solar cycles for solar cycles 7–13 sets will be very interesting too.

Near-equator sunspot groups before the Maunder minimum. Near-equator sunspot groups are present in the Scheiner and Hevelius data, which belong to the pre-Maunder minimum period. Based on recent magnetogram data, Cameron *et al.* (2013) reported that even a single large group near the equator can affect the net hemispheric flux of the following minimum by up to 60%. He suggested that the presence of such groups before the Maunder minimum may have led to such a grand minimum. Hence, a study of these groups with a SFTM simulation and their effect on the progress of solar activity will be interesting.

Bibliography

- Abarbanell, C., Wöhl, H.: 1981, Solar Rotation Velocity as Determined from Sunspot Drawings of Hevelius, J. in the 17th-Century. *Sol. Phys.* **70**, 197. doi:[10.1007/BF00154400](https://doi.org/10.1007/BF00154400).
- Abetti, G.: 1954, *The History of Astronomy*, Sidgwick and Jackson, London, UK.
- Alexandrescu, M., Courtillot, V., Le Mouél, J.L.: 1996, Geomagnetic Field Direction in Paris Since the Mid-Sixteenth Century. *Phys. Earth Planet. Int.* **98**, 321. doi:[10.1016/S0031-9201\(96\)03194-9](https://doi.org/10.1016/S0031-9201(96)03194-9).
- Aparicio, A.J.P., Vaquero, J.M., Carrasco, V.M.S., Gallego, M.C.: 2014, Sunspot Numbers and Areas from the Madrid Astronomical Observatory (1876–1986). *Sol. Phys.* **289**, 4335. doi:[10.1007/s11207-014-0567-x](https://doi.org/10.1007/s11207-014-0567-x).
- Apelles, C.S.: 1612, *De Maculis Solarib[us] et Stellis Circa Iovem Errantibus, Accuratiores Disquisitio*, Ad insigne pinus, Augsburg, Germany.
- Arlt, R.: 2008, Digitization of Sunspot Drawings by Staudacher in 1749–1796. *Sol. Phys.* **247**, 399. doi:[10.1007/s11207-007-9113-4](https://doi.org/10.1007/s11207-007-9113-4).
- Arlt, R.: 2009, The Butterfly Diagram in the Eighteenth Century. *Sol. Phys.* **255**, 143. doi:[10.1007/s11207-008-9306-5](https://doi.org/10.1007/s11207-008-9306-5).
- Arlt, R.: 2011, The Sunspot Observations by Samuel Heinrich Schwabe. *Astron. Nachr.* **332**, 805. doi:[10.1002/asna.201111601](https://doi.org/10.1002/asna.201111601).
- Arlt, R., Fröhlich, H.E.: 2012, The Solar Differential Rotation in the 18th Century. *Astron. Astrophys.* **543**, A7. doi:[10.1051/0004-6361/201219266](https://doi.org/10.1051/0004-6361/201219266).
- Arlt, R., Leussu, R., Giese, N., Mursula, K., Usoskin, I.G.: 2013, Sunspot Positions and Sizes for 1825–1867 from the Observations by Samuel Heinrich Schwabe. *Mon. Not. R. Astron. Soc.* **433**, 3165. doi:[10.1093/mnras/stt961](https://doi.org/10.1093/mnras/stt961).
- Babcock, H.W.: 1961, The Topology of the Sun's Magnetic Field and the 22-Year Cycle. *Astrophys. J.* **133**, 572. doi:[10.1086/147060](https://doi.org/10.1086/147060).
- Ballester, J.L., Oliver, R., Carbonell, M.: 2005, The Periodic Behaviour of the North-South Asymmetry of Sunspot Areas Revisited. *Astron. Astrophys.* **431**, L5. doi:[10.1051/0004-6361:200400135](https://doi.org/10.1051/0004-6361:200400135).
- Balmaceda, L.A., Solanki, S.K., Krivova, N.A., Foster, S.: 2009, A Homogeneous Database of Sunspot Areas Covering More Than 130 Years. *J. Geophys. Res.* **114**, A07104. doi:[10.1029/2009JA014299](https://doi.org/10.1029/2009JA014299).
- Balthasar, H., Vázquez, M., Wöhl, H.: 1986, Differential Rotation of Sunspot Groups in the Period from 1874 Through 1976 and Changes of the Rotation Velocity Within the Solar Cycle. *Astron. Astrophys.* **155**, 87.

- Baranyi, T.: 2015, Comparison of Debrecen and Mount Wilson/Kodaikanal Sunspot Group Tilt Angles and the Joy's Law. *Mon. Not. R. Astron. Soc.* **447**, 1857. doi:[10.1093/mnras/stu2572](https://doi.org/10.1093/mnras/stu2572).
- Barnard, L., Lockwood, M., Hapgood, M.A., Owens, M.J., Davis, C.J., Steinhilber, F.: 2011, Predicting Space Climate Change. *Geophys. Res. Lett.* **38**, L16103. doi:[10.1029/2011GL048489](https://doi.org/10.1029/2011GL048489).
- Barraclough, D.R.: 1994, Observations of the Earth's Magnetic Field in Edinburgh from 1670 to the Present Day. *Trans. R. Soc. Edinburgh Earth Sci.* **85**, 239. doi:[10.1017/S0263593300002029](https://doi.org/10.1017/S0263593300002029).
- Bartels, J., Heck, N.H., Johnston, H.F.: 1939, The Three-Hour-Range Index Measuring Geomagnetic Activity. *J. Geophys. Res.* **44**, 411. doi:[10.1029/TE044i004p00411](https://doi.org/10.1029/TE044i004p00411).
- Basu, S., Antia, H.M.: 2010, Characteristics of Solar Meridional Flows During Solar Cycle 23. *Astrophys. J.* **717**, 488. doi:[10.1088/0004-637X/717/1/488](https://doi.org/10.1088/0004-637X/717/1/488).
- Baumann, I., Solanki, S.K.: 2005, On the Size Distribution of Sunspot Groups in the Greenwich Sunspot Record 1874–1976. *Astron. Astrophys.* **443**, 1061. doi:[10.1051/0004-6361:20053415](https://doi.org/10.1051/0004-6361:20053415).
- Baumann, I., Schmitt, D., Schüssler, M.: 2006, A Necessary Extension of the Surface Flux Transport Model. *Astron. Astrophys.* **446**, 307. doi:[10.1051/0004-6361:20053488](https://doi.org/10.1051/0004-6361:20053488).
- Baumann, I., Schmitt, D., Schüssler, M., Solanki, S.K.: 2004, Evolution of the Large-Scale Magnetic Field on the Solar Surface: A Parameter Study. *Astron. Astrophys.* **426**, 1075. doi:[10.1051/0004-6361:20048024](https://doi.org/10.1051/0004-6361:20048024).
- Berdyugina, S.V., Moss, D., Sokoloff, D., Usoskin, I.G.: 2006, Active Longitudes, Nonaxisymmetric Dynamos and Phase Mixing. *Astron. Astrophys.* **445**, 703. doi:[10.1051/0004-6361:20053454](https://doi.org/10.1051/0004-6361:20053454).
- Bertello, L., Pevtsov, A.A., Pietarila, A.: 2012, Signature of Differential Rotation in Sun-as-a-star Ca IJK Measurements. *Astrophys. J.* **761**, 11. doi:[10.1088/0004-637X/761/1/11](https://doi.org/10.1088/0004-637X/761/1/11).
- Biermann, L.: 1941, Der Gegenwärtige Stand der Theorie Konvektiver Sonnenmodelle. *Vierteljahresschr. Astron. Gesellsch.* **76**, 194.
- Birkenmajer, A.: 1967, Alexius Sylvius Polonus (1593–ca. 1653), a Little-Known Maker of Astronomical Instruments. *Vistas Astron.* **9**, 11. doi:[10.1016/0083-6656\(67\)90007-4](https://doi.org/10.1016/0083-6656(67)90007-4).
- Bogdan, T.J., Gilman, P.A., Lerche, I., Howard, R.: 1988, Distribution of Sunspot Umbral Areas: 1917–1982. *Astrophys. J.* **327**, 451. doi:[10.1086/166206](https://doi.org/10.1086/166206).
- Boteler, D.H., Pirjola, R.J., Nevanlinna, H.: 1998, The Effects of Geomagnetic Disturbances on Electrical Systems at the Earth's Surface. *Adv. Space Res.* **22**, 17. doi:[10.1016/S0273-1177\(97\)01096-X](https://doi.org/10.1016/S0273-1177(97)01096-X).
- Brandt, P.N., Schmidt, W., Steinegger, M.: 1990, On the Umbra-Penumbra Area Ratio of Sunspots. *Sol. Phys.* **129**, 191. doi:[10.1007/BF00154373](https://doi.org/10.1007/BF00154373).
- Braunmühl, A.: 1891, *Christoph Scheiner als Mathematiker, Physiker und Astronom*, Buchner-sche Verlagsbuchhandlung, Bamberg, Germany.
- Brockhaus: 1991, *Brockhaus-Enzyklopädie, Vol. 16, Nos–Per*, F.A. Brockhaus, Mannheim, Germany.
- Brockhaus: 1992, *Brockhaus-Enzyklopädie, Vol. 19, Rut–Sch*, F.A. Brockhaus, Mannheim, Germany.
- Brouwer, M.P., Zwaan, C.: 1990, Sunspot Nests as Traced by a Cluster Analysis. *Sol. Phys.* **129**, 221. doi:[10.1007/BF00159038](https://doi.org/10.1007/BF00159038).

- Cafarella, L., De Santis, A., Meloni, A.: 1992, Secular Variation in Italy from Historical Geomagnetic Field Measurements. *Phys. Earth Planet. Int.* **73**, 206. doi:[10.1016/0031-9201\(92\)90091-9](https://doi.org/10.1016/0031-9201(92)90091-9).
- Caligari, P., Moreno-Insertis, F., Schüssler, M.: 1995, Emerging Flux Tubes in the Solar Convection Zone. I: Asymmetry, Tilt, and Emergence Latitude. *Astrophys. J.* **441**, 886. doi:[10.1086/175410](https://doi.org/10.1086/175410).
- Cameron, R.H., Jiang, J., Schmitt, D., Schüssler, M.: 2010, Surface Flux Transport Modeling for Solar Cycles 15–21: Effects of Cycle-Dependent Tilt Angles of Sunspot Groups. *Astrophys. J.* **719**, 264. doi:[10.1088/0004-637X/719/1/264](https://doi.org/10.1088/0004-637X/719/1/264).
- Cameron, R.H., Dasi-Espuig, M., Jiang, J., Işık, E., Schmitt, D., Schüssler, M.: 2013, Limits to Solar Cycle Predictability: Cross-Equatorial Flux Plumes. *Astron. Astrophys.* **557**, A141. doi:[10.1051/0004-6361/201321981](https://doi.org/10.1051/0004-6361/201321981).
- Carbonell, M., Oliver, R., Ballester, J.L.: 1993, On the Asymmetry of Solar Activity. *Astron. Astrophys.* **274**, 497.
- Carrington, R.C.: 1858, On the Distribution of the Solar Spots in Latitudes Since the Beginning of the Year 1854, with a Map. *Mon. Not. R. Astron. Soc.* **19**, 1. doi:[10.1093/mnras/19.1.1](https://doi.org/10.1093/mnras/19.1.1).
- Carrington, R.: 1863, *Observations of the Spots on the Sun from November 9, 1853, to March 24, 1861, Made at Redhill*, Williams & Norgate, London, Edinburgh.
- Casas, R., Vaquero, J.M., Vazquez, M.: 2006, Solar Rotation in the 17th Century. *Sol. Phys.* **234**, 379. doi:[10.1007/s11207-006-0036-2](https://doi.org/10.1007/s11207-006-0036-2).
- Chapman, G.A., Cookson, A.M., Dobias, J.J.: 1997, Solar Variability and the Relation of Facular to Sunspot Areas During Solar Cycle 22. *Astrophys. J.* **482**, 541. doi:[10.1086/304138](https://doi.org/10.1086/304138).
- Charbonneau, P.: 2010, Dynamo Models of the Solar Cycle. *Living Rev. Sol. Phys.* **7**, 3. doi:[10.12942/lrsp-2010-3](https://doi.org/10.12942/lrsp-2010-3).
- Chernosky, E.J.: 1954, A Relationship Between the Length and Activity of Sunspot Cycles. *Publ. Astron. Soc. Pac.* **66**, 241. doi:[10.1086/126706](https://doi.org/10.1086/126706).
- Choudhuri, A.R., Schüssler, M., Dikpati, M.: 1995, The Solar Dynamo with Meridional Circulation. *Astron. Astrophys.* **303**, L29.
- Clette, F., Lefèvre, L.: 2015, The New Sunspot Number: Re-Calibration, Re-Computation and Implications for the Solar Cycle. *IAU Gen. Ass.* **22**, 2256393.
- Clette, F., Lefèvre, L.: 2016, The New Sunspot Number: Assembling All Corrections. *Sol. Phys.* **291**, 2629. doi:[10.1007/s11207-016-1014-y](https://doi.org/10.1007/s11207-016-1014-y).
- Clette, F., Berghmans, D., Vanlommel, P., van der Linden, R.A.M., Koeckelenbergh, A., Wauters, L.: 2007, From the Wolf Number to the International Sunspot Index: 25 Years of SIDC. *Adv. Space Res.* **40**, 919. doi:[10.1016/j.asr.2006.12.045](https://doi.org/10.1016/j.asr.2006.12.045).
- Clette, F., Svalgaard, L., Vaquero, J.M., Cliver, E.W.: 2014, Revisiting the Sunspot Number. A 400-Year Perspective on the Solar Cycle. *Space Sci. Rev.* **186**, 35. doi:[10.1007/s11214-014-0074-2](https://doi.org/10.1007/s11214-014-0074-2).
- Cowling, T.G.: 1933, The Magnetic Field of Sunspots. *Mon. Not. R. Astron. Soc.* **94**, 39. doi:[10.1093/mnras/94.1.39](https://doi.org/10.1093/mnras/94.1.39).
- Cristo, A., Vaquero, J.M., Sánchez-Bajo, F.: 2011, HSUNSPOTS: A Tool for the Analysis of Historical Sunspot Drawings. *J. Atm. Solar-Terr. Phys.* **73**, 187. doi:[10.1016/j.jastp.2009.12.010](https://doi.org/10.1016/j.jastp.2009.12.010).

- Dasi-Espuig, M., Solanki, S.K., Krivova, N.A., Cameron, R., Peñuela, T.: 2010, Sunspot Group Tilt Angles and the Strength of the Solar Cycle. *Astron. Astrophys.* **518**, A7. doi:[10.1051/0004-6361/201014301](https://doi.org/10.1051/0004-6361/201014301).
- Dasi-Espuig, M., Solanki, S.K., Krivova, N.A., Cameron, R., Peñuela, T.: 2013, Sunspot Group Tilt Angles and the Strength of the Solar Cycle (Corrigendum). *Astron. Astrophys.* **556**, C3. doi:[10.1051/0004-6361/201014301e](https://doi.org/10.1051/0004-6361/201014301e).
- DeRosa, M.L.: 2006, Small-Scale Surface Flows and Their Implications for Solar Activity. In: Bothmer, V., Hady, A.A. (eds.) *Solar Activity and its Magnetic Origin, IAU Symp.* **233**, 25. doi:[10.1017/S1743921306001347](https://doi.org/10.1017/S1743921306001347).
- DeVore, C.R.: 1987, The Decay of the Large-Scale Solar Magnetic Field. *Sol. Phys.* **112**, 17. doi:[10.1007/BF00148484](https://doi.org/10.1007/BF00148484).
- DeVore, C.R., Boris, J.P., Sheeley, N.R. Jr.: 1984, The Concentration of the Large-Scale Solar Magnetic Field by a Meridional Surface Flow. *Sol. Phys.* **92**, 1. doi:[10.1007/BF00157230](https://doi.org/10.1007/BF00157230).
- Dezső, L., Kovács, A., Gerlei, O.: 1987, Debrecen Photoheliographic Results for the Year 1977. *Publ. Debrecen Obs. Heliogr. Ser., 1* **1**, 11.
- Diercke, A., Arlt, R., Denker, C.: 2015, Digitization of Sunspot Drawings by Spörer Made in 1861–1894. *Astron. Nachr.* **336**, 53. doi:[10.1002/asna.201412138](https://doi.org/10.1002/asna.201412138).
- Dikpati, M., Charbonneau, P.: 1999, A Babcock-Leighton Flux Transport Dynamo with Solar-Like Differential Rotation. *Astrophys. J.* **518**, 508. doi:[10.1086/307269](https://doi.org/10.1086/307269).
- Dikpati, M., Gilman, P.A.: 2012, Theory of Solar Meridional Circulation at High Latitudes. *Astrophys. J.* **746**, 65. doi:[10.1088/0004-637X/746/1/65](https://doi.org/10.1088/0004-637X/746/1/65).
- Dikpati, M., Gilman, P.A., de Toma, G., Ulrich, R.K.: 2010, Impact of Changes in the Sun's Conveyor-Belt on Recent Solar Cycles. *Geophys. Res. Lett.* **37**, L14107. doi:[10.1029/2010GL044143](https://doi.org/10.1029/2010GL044143).
- D'Silva, S., Choudhuri, A.R.: 1993, A Theoretical Model for Tilts of Bipolar Magnetic Regions. *Astron. Astrophys.* **272**, 621.
- Du, Z., Du, S.: 2006, The Relationship Between the Amplitude and Descending Time of a Solar Activity Cycle. *Sol. Phys.* **238**, 431. doi:[10.1007/s11207-006-0175-5](https://doi.org/10.1007/s11207-006-0175-5).
- Dumusque, X., Glenday, A., Phillips, D.F., Buchschacher, N., Collier Cameron, A., Ceconi, M., Charbonneau, D., Cosentino, R., Ghedina, A., Latham, D.W., Li, C.H., Lodi, M., Lovis, C., Molinari, E., Pepe, F., Udry, S., Sasselov, D., Szentgyorgyi, A., Walsworth, R.: 2015, HARPS-N Observes the Sun as a Star. *Astrophys. J. Lett.* **814**, L21. doi:[10.1088/2041-8205/814/2/L21](https://doi.org/10.1088/2041-8205/814/2/L21).
- Durney, B.R.: 1995, On a Babcock-Leighton Dynamo Model with a Deep-Seated Generating Layer for the Toroidal Magnetic Field. *Sol. Phys.* **160**, 213. doi:[10.1007/BF00732805](https://doi.org/10.1007/BF00732805).
- Eddy, J.A.: 1976, The Maunder Minimum. *Science* **192**, 1189. doi:[10.1126/science.192.4245.1189](https://doi.org/10.1126/science.192.4245.1189).
- Eddy, J.A.: 1977, Climate and the Changing Sun. *Clim. Change* **1**, 173. doi:[10.1007/BF01884410](https://doi.org/10.1007/BF01884410).
- Eddy, J.A., Gilman, P.A., Trotter, D.E.: 1976, Solar Rotation During the Maunder Minimum. *Sol. Phys.* **46**, 3. doi:[10.1007/BF00157550](https://doi.org/10.1007/BF00157550).
- Eddy, J.A., Gilman, P.A., Trotter, D.E.: 1977, Anomalous Solar Rotation in the Early 17th Century. *Science* **198**, 824. doi:[10.1126/science.198.4319.824](https://doi.org/10.1126/science.198.4319.824).
- Fan, Y.: 2004, Magnetic Fields in the Solar Convection Zone. *Living Rev. Sol. Phys.* **1**, 1.

- Fan, Y., Fisher, G.H.: 1996, Radiative Heating and the Buoyant Rise of Magnetic Flux Tubes in the Solar interior. *Sol. Phys.* **166**, 17. doi:[10.1007/BF00179354](https://doi.org/10.1007/BF00179354).
- Foukal, P., Bertello, L., Livingston, W.C., Pevtsov, A.A., Singh, J., Tlatov, A.G., Ulrich, R.K.: 2009, A Century of Solar Ca II Measurements and Their Implication for Solar UV Driving of Climate. *Sol. Phys.* **255**, 229. doi:[10.1007/s11207-009-9330-0](https://doi.org/10.1007/s11207-009-9330-0).
- Fröhlich, C.: 2016, Determination of Time-Dependent Uncertainty of the Total Solar Irradiance Records from 1978 to Present. *J. Space Weather Space Clim.* **6**, A18. doi:[10.1051/swsc/2016012](https://doi.org/10.1051/swsc/2016012).
- Gautier, A.: 1852, Relation Entre Les Taches Du Soleil Et Les Phénomènes Magnétiques. *Arch. Sci.* **21**, 194.
- Gavryuseva, E.: 2006, Relationships Between Photospheric Magnetic Field, Solar Wind and Geomagnetic Perturbations over Last 30 Years. In: Bothmer, V., Hady, A.A. (eds.) *Solar Activity and its Magnetic Origin, IAU Symp.* **233**, 291. doi:[10.1017/S1743921306002031](https://doi.org/10.1017/S1743921306002031).
- Gizon, L., Birch, A.C., Spruit, H.C.: 2010, Local Helioseismology: Three-Dimensional Imaging of the Solar Interior. *Ann. Rev. Astron. Astrophys.* **48**, 289. doi:[10.1146/annurev-astro-082708-101722](https://doi.org/10.1146/annurev-astro-082708-101722).
- Gnevyshev, M.N., Ohl, A.I.: 1948, On the 22-Year Cycle of Solar Activity. *Astron. Zh.* **25**, 18.
- González Hernández, I., Howe, R., Komm, R., Hill, F.: 2010, Meridional Circulation During the Extended Solar Minimum: Another Component of the Torsional Oscillation? *Astrophys. J. Lett.* **713**, L16. doi:[10.1088/2041-8205/713/1/L16](https://doi.org/10.1088/2041-8205/713/1/L16).
- González Hernández, I., Komm, R., van Driel-Gesztelyi, L., Baker, D., Harra, L., Howe, R.: 2013, Subsurface Flows Associated with Non-Joy Oriented Active Regions: A Case Study. **440**, 012050. doi:[10.1088/1742-6596/440/1/012050](https://doi.org/10.1088/1742-6596/440/1/012050).
- Gray, L.J., Beer, J., Geller, M., Haigh, J.D., Lockwood, M., Matthes, K., Cubasch, U., Fleitmann, D., Harrison, G., Hood, L., Luterbacher, J., Meehl, G.A., Shindell, D., van Geel, B., White, W.: 2010, Solar Influences on Climate. *Rev. Geophys.* **48**, RG4001. doi:[10.1029/2009RG000282](https://doi.org/10.1029/2009RG000282).
- Gyóri, L.: 1998, Automation of Area Measurement of Sunspots. *Sol. Phys.* **180**, 109. doi:[10.1023/A:1005081621268](https://doi.org/10.1023/A:1005081621268).
- Hagenaar, H.J., Schrijver, C.J., Title, A.M.: 2003, The Properties of Small Magnetic Regions on the Solar Surface and the Implications for the Solar Dynamo(s). *Astrophys. J.* **584**, 1107. doi:[10.1086/345792](https://doi.org/10.1086/345792).
- Haigh, J.D.: 1994, The Role of Stratospheric Ozone in Modulating the Solar Radiative Forcing of Climate. *Nature* **370**, 544. doi:[10.1038/370544a0](https://doi.org/10.1038/370544a0).
- Haigh, J.D., Lockwood, M., Giampapa, M.S., Rüedi, I., Güdel, M., Schmutz, W. (eds.): 2005, *The Sun, Solar Analogs and the Climate, Saas-Fee Advanced Course 34*, Springer, Berlin, Germany.
- Hale, G.E., Nicholson, S.B.: 1925, The Law of Sun-Spot Polarity. *Astrophys. J.* **62**, 270. doi:[10.1086/142933](https://doi.org/10.1086/142933).
- Hale, G.E., Ellerman, F., Nicholson, S.B., Joy, A.H.: 1919, The Magnetic Polarity of Sun-Spots. *Astrophys. J.* **49**, 153. doi:[10.1086/142452](https://doi.org/10.1086/142452).
- Harriot, T.: 1613, *Spots on the Sun*, Petworth House, HMC 241 VIII, West Sussex, England.

- Harvey, K.L., Martin, S.F.: 1973, Ephemeral Active Regions. *Sol. Phys.* **32**, 389. doi:[10.1007/BF00154951](https://doi.org/10.1007/BF00154951).
- Harvey, K.L., Zwaan, C.: 1993, Properties and Emergence of Bipolar Active Regions. *Sol. Phys.* **148**, 85. doi:[10.1007/BF00675537](https://doi.org/10.1007/BF00675537).
- Hathaway, D.H.: 1996, Doppler Measurements of the Sun's Meridional Flow. *Astrophys. J.* **460**, 1027. doi:[10.1086/177029](https://doi.org/10.1086/177029).
- Hathaway, D.H.: 2009, Solar Cycle Forecasting. *Space Sci. Rev.* **144**, 401. doi:[10.1007/s11214-008-9430-4](https://doi.org/10.1007/s11214-008-9430-4).
- Hathaway, D.H.: 2010, The Solar Cycle. *Living Rev. Sol. Phys.* **7**, 1. doi:[10.12942/lrsp-2010-1](https://doi.org/10.12942/lrsp-2010-1).
- Hathaway, D.H.: 2015, The Solar Cycle. *Living Rev. Sol. Phys.* **12**, 4. doi:[10.1007/lrsp-2015-4](https://doi.org/10.1007/lrsp-2015-4).
- Hathaway, D.H., Rightmire, L.: 2010, Variations in the Sun's Meridional Flow over a Solar Cycle. *Science* **327**, 1350. doi:[10.1126/science.1181990](https://doi.org/10.1126/science.1181990).
- Henney, C.J., Hock, R.A., Schooley, A.K., Toussaint, W.A., White, S.M., Arge, C.N.: 2015, Forecasting Solar Extreme and Far Ultraviolet Irradiance. *Space Weather* **13**, 141. doi:[10.1002/2014SW001118](https://doi.org/10.1002/2014SW001118).
- Herr, R.B.: 1978, Solar Rotation Determined from Thomas Harriot's Sunspot Observations of 1611 to 1613. *Science* **202**, 1079. doi:[10.1126/science.202.4372.1079](https://doi.org/10.1126/science.202.4372.1079).
- Herschel, W.: 1801, Observations Tending to Investigate the Nature of the Sun, in Order to Find the Causes or Symptoms of its Variable Emission of Light and Heat; With Remarks on the Use That May Possibly Be Drawn from Solar Observations. *Philosoph. Trans. Roy. Soc. Lond. Ser. I* **91**, 265.
- Hevelius, J.: 1647, *Selenographia Sive Lunae Descriptio*, Hünefeld, Danzig, Poland. doi:[10.3931/e-rara-238](https://doi.org/10.3931/e-rara-238).
- Hockey, T., Trimble, V., Williams, T.R., Bracher, K., Jarrell, R.A., Marché, J.D., Ragep, F.J., Palmeri, J., Bolt, M.: 2007, *The Biographical Encyclopedia of Astronomers*, Springer, New York, USA. doi:[10.1007/978-0-387-30400-7](https://doi.org/10.1007/978-0-387-30400-7).
- Houtgast, J., van Sluiter, A.: 1948, Statistical Investigations Concerning the Magnetic Fields of Sunspots I. *Bull. Astron. Inst. Netherlands* **10**, 325.
- Howard, R., Harvey, J.: 1970, Spectroscopic Determinations of Solar Rotation. *Sol. Phys.* **12**, 23. doi:[10.1007/BF02276562](https://doi.org/10.1007/BF02276562).
- Howard, R., Labonte, B.J.: 1980, The Sun Is Observed to be a Torsional Oscillator with a Period of 11 Years. *Astrophys. J. Lett.* **239**, L33. doi:[10.1086/183286](https://doi.org/10.1086/183286).
- Howard, R., Gilman, P.I., Gilman, P.A.: 1984, Rotation of the Sun Measured from Mount Wilson White-Light Images. *Astrophys. J.* **283**, 373. doi:[10.1086/162315](https://doi.org/10.1086/162315).
- Howard, R.F.: 1991, Axial Tilt Angles of Sunspot Groups. *Sol. Phys.* **136**, 251. doi:[10.1007/BF00146534](https://doi.org/10.1007/BF00146534).
- Howe, R., Christensen-Dalsgaard, J., Hill, F., Komm, R.W., Larsen, R.M., Schou, J., Thompson, M.J., Toomre, J.: 2000, Deeply Penetrating Banded Zonal Flows in the Solar Convection Zone. *Astrophys. J. Lett.* **533**, L163. doi:[10.1086/312623](https://doi.org/10.1086/312623).
- Hoyt, D.V., Schatten, K.H.: 1998, Group Sunspot Numbers: A New Solar Activity Reconstruction. *Sol. Phys.* **181**, 491. doi:[10.1023/A:1005056326158](https://doi.org/10.1023/A:1005056326158).

- Illarionov, E., Tlatov, A., Sokoloff, D.: 2015, The Properties of the Tilts of Bipolar Solar Regions. *Sol. Phys.* **290**, 351. doi:[10.1007/s11207-014-0612-9](https://doi.org/10.1007/s11207-014-0612-9).
- Inceoglu, F., Simoniello, R., Knudsen, M.F., Karoff, C., Olsen, J., Turck-Chiéze, S., Jacobsen, B.H.: 2015, Grand Solar Minima and Maxima Deduced from ^{10}Be and ^{14}C : Magnetic Dynamo Configuration and Polarity Reversal. *Astron. Astrophys.* **577**, A20. doi:[10.1051/0004-6361/201424212](https://doi.org/10.1051/0004-6361/201424212).
- Ivanov, V.G.: 2012, Joy's Law and its Features According to the Data of Three Sunspot Catalogs. *Geomag. Aeron.* **52**, 999. doi:[10.1134/S0016793212080130](https://doi.org/10.1134/S0016793212080130).
- Jafarzadeh, S., Cameron, R.H., Solanki, S.K., Pietarila, A., Feller, A., Lagg, A., Gandorfer, A.: 2014, Migration of Ca II H Bright Points in the Internetwork. *Astron. Astrophys.* **563**, A101. doi:[10.1051/0004-6361/201323011](https://doi.org/10.1051/0004-6361/201323011).
- Jiang, J., Cameron, R.H., Schüssler, M.: 2014a, Effects of the Scatter in Sunspot Group Tilt Angles on the Large-Scale Magnetic Field at the Solar Surface. *Astrophys. J.* **791**, 5. doi:[10.1088/0004-637X/791/1/5](https://doi.org/10.1088/0004-637X/791/1/5).
- Jiang, J., Cameron, R.H., Schmitt, D., Schüssler, M.: 2011a, The Solar Magnetic Field Since 1700. I. Characteristics of Sunspot Group Emergence and Reconstruction of the Butterfly Diagram. *Astron. Astrophys.* **528**, A82. doi:[10.1051/0004-6361/201016167](https://doi.org/10.1051/0004-6361/201016167).
- Jiang, J., Cameron, R.H., Schmitt, D., Schüssler, M.: 2011b, The Solar Magnetic Field Since 1700. II. Physical Reconstruction of Total, Polar and Open Flux. *Astron. Astrophys.* **528**, A83. doi:[10.1051/0004-6361/201016168](https://doi.org/10.1051/0004-6361/201016168).
- Jiang, J., Hathaway, D.H., Cameron, R.H., Solanki, S.K., Gizon, L., Upton, L.: 2014b, Magnetic Flux Transport at the Solar Surface. *Space Sci. Rev.* **186**, 491. doi:[10.1007/s11214-014-0083-1](https://doi.org/10.1007/s11214-014-0083-1).
- Keppens, R., Martínez Pillet, V.: 1996, The Magnetic Structure of Pores and Sunspots Derived from Advanced Stokes Polarimeter Data. *Astron. Astrophys.* **316**, 229.
- Kiess, C., Rezaei, R., Schmidt, W.: 2014, Properties of Sunspot Umbrae Observed in Cycle 24. *Astron. Astrophys.* **565**, A52. doi:[10.1051/0004-6361/201321119](https://doi.org/10.1051/0004-6361/201321119).
- Kilcik, A., Yurchyshyn, V., Clette, F., Ozguc, A., Rozelot, J.P.: 2016, Active Latitude Oscillations Observed on the Sun. *Sol. Phys.* **291**, 1077. doi:[10.1007/s11207-016-0890-5](https://doi.org/10.1007/s11207-016-0890-5).
- King, H.C.: 1955, *The History of the Telescope*, Dover Publications, Inc., Mineola, New York, USA.
- Kleczek, J.: 1952, Solar Flare Index Calculations. *Publ. Centr. Astron. Inst. Czech.* **22**.
- Kleorin, N.I., Rogachevskii, I.V., Ruzmaikin, A.A.: 1989, The Effect of Negative Magnetic Pressure and the Large-Scale Magnetic Field Instability in the Solar Convective Zone. *Pis'ma Astron. Zh.* **15**, 639.
- Komm, R.W., Howard, R.F., Harvey, J.W.: 1993a, Meridional Flow of Small Photospheric Magnetic Features. *Sol. Phys.* **147**, 207. doi:[10.1007/BF00690713](https://doi.org/10.1007/BF00690713).
- Komm, R.W., Howard, R.F., Harvey, J.W.: 1993b, Rotation Rates of Small Magnetic Features from Two- and One-Dimensional Cross-Correlation Analyses. *Sol. Phys.* **145**, 1. doi:[10.1007/BF00627979](https://doi.org/10.1007/BF00627979).
- Komm, R.W., Howard, R.F., Harvey, J.W.: 1993c, Torsional Oscillation Patterns in Photospheric Magnetic Features. *Sol. Phys.* **143**, 19. doi:[10.1007/BF00619094](https://doi.org/10.1007/BF00619094).

- Komm, R., González Hernández, I., Hill, F., Bogart, R., Rabello-Soares, M.C., Haber, D.: 2013, Subsurface Meridional Flow from HMI Using the Ring-Diagram Pipeline. *Sol. Phys.* **287**, 85. doi:[10.1007/s11207-012-0073-y](https://doi.org/10.1007/s11207-012-0073-y).
- Komm, R., González Hernández, I., Howe, R., Hill, F.: 2015, Solar-Cycle Variation of Subsurface Meridional Flow Derived with Ring-Diagram Analysis. *Sol. Phys.* **290**, 3113. doi:[10.1007/s11207-015-0729-5](https://doi.org/10.1007/s11207-015-0729-5).
- Kopp, G.: 2016, Magnitudes and Timescales of Total Solar Irradiance Variability. *J. Space Weather Space Climate* **6**, A30. doi:[10.1051/swsc/2016025](https://doi.org/10.1051/swsc/2016025).
- Korzennik, S.G., Eff-Darwich, A.: 2011, The Rotation Rate and its Evolution Derived from Improved Mode Fitting and Inversion Methodology. In: *J. Phys. Conf. Ser.* **271**, 012067. doi:[10.1088/1742-6596/271/1/012067](https://doi.org/10.1088/1742-6596/271/1/012067).
- Kosovichev, A.G., Stenflo, J.O.: 2008, Tilt of Emerging Bipolar Magnetic Regions on the Sun. *Astrophys. J. Lett.* **688**, L115. doi:[10.1086/595619](https://doi.org/10.1086/595619).
- Landsman, W.B.: 1993, The IDL Astronomy User's Library. In: *Astronomical Data Analysis Software and Systems II, ASP Conf. Ser.* **52**, 246.
- Larmor, J.: 1920, How Could a Rotating Body such as the Sun Become a Magnet? *Rep. Brit. Assoc. Adv. Sci* **87th Meeting**, 159.
- Lean, J.L., Warren, H.P., Mariska, J.T., Bishop, J.: 2003, A New Model of Solar EUV Irradiance Variability 2. Comparisons with Empirical Models and Observations and Implications for Space Weather. *J. Geophys. Res.: Space Phys.* **108**, 1059. doi:[10.1029/2001JA009238](https://doi.org/10.1029/2001JA009238).
- Leighton, R.B.: 1964, Transport of Magnetic Fields on the Sun. *Astrophys. J.* **140**, 1547. doi:[10.1086/148058](https://doi.org/10.1086/148058).
- Leussu, R., Usoskin, I.G., Arlt, R., Mursula, K.: 2013, Inconsistency of the Wolf Sunspot Number Series Around 1848. *Astron. Astrophys.* **559**, A28. doi:[10.1051/0004-6361/201322373](https://doi.org/10.1051/0004-6361/201322373).
- Leussu, R., Usoskin, I.G., Arlt, R., Mursula, K.: 2016, Properties of Sunspot Cycles and Hemispheric Wings Since the 19th Century. *Astron. Astrophys.* **592**, A160. doi:[10.1051/0004-6361/201628335](https://doi.org/10.1051/0004-6361/201628335).
- Li, K.J., Kong, D.F., Liang, H.F., Feng, W.: 2014, What do the Solar Activity Indices Represent? *Astron. Nachr.* **335**, 371. doi:[10.1002/asna.201312016](https://doi.org/10.1002/asna.201312016).
- Li, J., Ulrich, R.K.: 2012, Long-Term Measurements of Sunspot Magnetic Tilt Angles. *Astrophys. J.* **758**, 115. doi:[10.1088/0004-637X/758/2/115](https://doi.org/10.1088/0004-637X/758/2/115).
- Li, K.J., Wang, J.X., Xiong, S.Y., Liang, H.F., Yun, H.S., Gu, X.M.: 2002, Regularity of the North-South Asymmetry of Solar Activity. *Astron. Astrophys.* **383**, 648. doi:[10.1051/0004-6361:20011799](https://doi.org/10.1051/0004-6361:20011799).
- Lockwood, M.: 2002, An Evaluation of the Correlation Between Open Solar Flux and Total Solar Irradiance. *Astron. Astrophys.* **382**, 678. doi:[10.1051/0004-6361:20011666](https://doi.org/10.1051/0004-6361:20011666).
- Lockwood, M., Stamper, R.: 1999, Long-Term Drift of the Coronal Source Magnetic Flux and the Total Solar Irradiance. *Geophys. Res. Lett.* **26**, 2461. doi:[10.1029/1999GL900485](https://doi.org/10.1029/1999GL900485).
- Lockwood, M., Owens, M.J., Barnard, L.: 2014, Centennial Variations in Sunspot Number, Open Solar Flux, and Streamer Belt Width: 1. Correction of the Sunspot Number Record Since 1874. *J. Geophys. Res.: Space Phys.* **119**, 5172. doi:[10.1002/2014JA019970](https://doi.org/10.1002/2014JA019970).
- Mackay, D.H., Yeates, A.R.: 2012, The Sun's Global Photospheric and Coronal Magnetic Fields: Observations and Models. *Living Rev. Sol. Phys.* **9**, 6. doi:[10.12942/lrsp-2012-6](https://doi.org/10.12942/lrsp-2012-6).

- Mackay, D.H., Gaizauskas, V., van Ballegoijen, A.A.: 2000, Comparison of Theory and Observations of the Chirality of Filaments Within a Dispersing Activity Complex. *Astrophys. J.* **544**, 1122. doi:[10.1086/317244](https://doi.org/10.1086/317244).
- Mairan, J.J.: 1754, *Traité Physique et Historique de l'Aurora Boréale*, 2nd edn. Academie Royale des Sciences, Paris, France.
- Makarov, V.I., Tlatov, A.G., Sivaraman, K.R.: 2003, Duration of Polar Activity Cycles and Their Relation to Sunspot Activity. *Sol. Phys.* **214**, 41. doi:[10.1023/A:1024003708284](https://doi.org/10.1023/A:1024003708284).
- Malapertius, C.: 1620, *Oratio Habita Duaci dum Lectionem Mathematicam Auspicaretur*, Balthasar Beller, Douai, France.
- Malapertius, C.: 1633, *Austriaca Sidera Heliocyclia Astronomicis Hypothesibus Illigata*, Balthasar Beller, Douai, France.
- Malin, S.R.C., Bullard, E.: 1981, The Direction of the Earth's Magnetic Field at London, 1570–1975. *Philos. Trans. Roy. Soc. Lond. A* **299**, 357. doi:[10.1098/rsta.1981.0026](https://doi.org/10.1098/rsta.1981.0026).
- Martin-Belda, D., Cameron, R.H.: 2016, Surface Flux Transport Simulations: Effect of Inflows Toward Active Regions and Random Velocities on the Evolution of the Sun's Large-Scale Magnetic Field. *Astron. Astrophys.* **586**, A73. doi:[10.1051/0004-6361/201527213](https://doi.org/10.1051/0004-6361/201527213).
- Martínez Pillet, V., Lites, B.W., Skumanich, A.: 1997, Active Region Magnetic Fields. I. Plage Fields. *Astrophys. J.* **474**, 810. doi:[10.1086/303478](https://doi.org/10.1086/303478).
- Maunder, E.W.: 1890, Prof. Spörer's Researches on Sun-Spots. *Mon. Not. R. Astron. Soc.* **50**, 251. doi:[10.1093/mnras/50.4.251](https://doi.org/10.1093/mnras/50.4.251).
- Maunder, E.W.: 1904, Note on the Distribution of Sun-Spots in Heliographic Latitude, 1874–1902. *Mon. Not. R. Astron. Soc.* **64**, 747. doi:[10.1093/mnras/64.8.747](https://doi.org/10.1093/mnras/64.8.747).
- Mavromichalaki, H., Petropoulos, B., Zouganelis, I.: 2002, Long-Term Modulation of the Coronal Index of Solar Activity. *Sol. Phys.* **206**, 401. doi:[10.1023/A:1015091500023](https://doi.org/10.1023/A:1015091500023).
- Mavromichalaki, H., Petropoulos, B., Plainaki, C., Dionatos, O., Zouganelis, I.: 2005, Coronal Index as a Solar Activity Index Applied to Space Weather. *advsr* **35**, 410. doi:[10.1016/j.asr.2005.01.084](https://doi.org/10.1016/j.asr.2005.01.084).
- Mayaud, P.N.: 1973, *A Hundred Year Series of Geomagnetic Data, 1868–1967, Indices aa, Storm Sudden Commencements*, IUGG Publications, Paris, France.
- McClintock, B.H., Norton, A.A.: 2013, Recovering Joy's Law as a Function of Solar Cycle, Hemisphere, and Longitude. *Sol. Phys.* **287**, 215. doi:[10.1007/s11207-013-0338-0](https://doi.org/10.1007/s11207-013-0338-0).
- McClintock, B.H., Norton, A.A., Li, J.: 2014, Re-Examining Sunspot Tilt Angle to Include Anti-Hale Statistics. *Astrophys. J.* **797**, 130. doi:[10.1088/0004-637X/797/2/130](https://doi.org/10.1088/0004-637X/797/2/130).
- Mosher, J.M.: 1977, The Magnetic History of Solar Active Regions. PhD Thesis, California Institute of Technology, Pasadena, USA.
- Muñoz-Jaramillo, A., Senkpeil, R.R., Windmueller, J.C., Amouzou, E.C., Longcope, D.W., Tlatov, A.G., Nagovitsyn, Y.A., Pevtsov, A.A., Chapman, G.A., Cookson, A.M., Yeates, A.R., Watson, F.T., Balmaceda, L.A., DeLuca, E.E., Martens, P.C.H.: 2015, Small-Scale and Global Dynamoes and the Area and Flux Distributions of Active Regions, Sunspot Groups, and Sunspots: A Multi-Database Study. *Astrophys. J.* **800**, 48. doi:[10.1088/0004-637X/800/1/48](https://doi.org/10.1088/0004-637X/800/1/48).

- Neidig, D., Wiborg, P., Confer, M., Haas, B., Dunn, R., Balasubramaniam, K.S., Gullixson, C., Craig, D., Kaufman, M., Hull, W., McGraw, R., Henry, T., Rentschler, R., Keller, C., Jones, H., Coulter, R., Gregory, S., Schimming, R., Smaga, B.: 1998, The USAF Improved Solar Observing Optical Network (ISOON) and its Impact on Solar Synoptic Data Bases. In: Balasubramaniam, K.S., Harvey, J., Rabin, D. (eds.) *Synoptic Solar Physics, ASP Conf. Ser.* **140**, 519.
- Neuhäuser, R., Neuhäuser, D.L.: 2016, Sunspot Numbers Based on Historic Records in the 1610s: Early Telescopic Observations by Simon Marius and Others. *Astron. Nachr.* **337**, 581. doi:[10.1002/asna.201512292](https://doi.org/10.1002/asna.201512292).
- Nevanlinna, H., Kataja, E.: 1993, An Extension of the Geomagnetic Activity Index Series aa for Two Solar Cycles (1844–1868). *Geophys. Res. Lett.* **20**, 2703. doi:[10.1029/93GL03001](https://doi.org/10.1029/93GL03001).
- Newton, H.W., Milsom, A.S.: 1955, Note on the Observed Differences in Spottedness of the Sun's Northern and Southern Hemispheres. *Mon. Not. R. Astron. Soc.* **115**, 398. doi:[10.1093/mnras/115.4.398](https://doi.org/10.1093/mnras/115.4.398).
- Ortiz, A., Rast, M.: 2005, How Good is the Ca II K as a Proxy for the Magnetic Flux? *Mem. Soc. Astron. Ital.* **76**, 1018.
- Özgüç, A., Ataç, T., Rybák, J.: 2003, Temporal Variability of the Flare Index (1966–2001). *Sol. Phys.* **214**, 375. doi:[10.1023/A:1024225802080](https://doi.org/10.1023/A:1024225802080).
- Pap, J., Anklin, M., Fröhlich, C., Wehrli, C., Varadi, F., Floyd, L.: 1999, Variations in Total Solar and Spectral Irradiance as Measured by the VIRGO Experiment on SOHO. *Adv. Space Res.* **24**, 215. doi:[10.1016/S0273-1177\(99\)00503-7](https://doi.org/10.1016/S0273-1177(99)00503-7).
- Parker, E.N.: 1955, Hydromagnetic Dynamo Models. *Astrophys. J.* **122**, 293. doi:[10.1086/146087](https://doi.org/10.1086/146087).
- Pérez Aparicio, A.J., Vaquero, J.M., Cruz Gallego, M.: 2012, The Proposed “Waldmeier Discontinuity”: How Does it Affect to Sunspot Cycle Characteristics? *J. Space Weather Space Clim.* **2**, A12. doi:[10.1051/swsc/2012012](https://doi.org/10.1051/swsc/2012012).
- Petrie, G., Ettinger, S.: 2015, Polar Field Reversals and Active Region Decay. *Space Sci. Rev.* **210**, 77. doi:[10.1007/s11214-015-0189-0](https://doi.org/10.1007/s11214-015-0189-0).
- Pulkkinen, P.J., Brooke, J., Pelt, J., Tuominen, I.: 1999, Long-Term Variation of Sunspot Latitudes. *Astron. Astrophys.* **341**, L43.
- Rangarajan, G.K.: 1989, Indices of Geomagnetic Activity. *Geomagnetism* **3**, 323.
- Reeves, E., Van Helden, A.: 2010, *On Sunspots. Galileo Galilei and Christoph Scheiner*, University of Chicago Press, Chicago, USA.
- Rek, R.: 2010, The Maunder Minimum and the Sun as the Possible Source of Particles Creating Increased Abundance of the ^{14}C Carbon Isotope. *Sol. Phys.* **261**, 337. doi:[10.1007/s11207-009-9432-8](https://doi.org/10.1007/s11207-009-9432-8).
- Rempel, M.: 2011, Subsurface Magnetic Field and Flow Structure of Simulated Sunspots. *Astrophys. J.* **740**, 15. doi:[10.1088/0004-637X/740/1/15](https://doi.org/10.1088/0004-637X/740/1/15).
- Ribes, J.C., Nesme-Ribes, E.: 1993, The Solar Sunspot Cycle in the Maunder Minimum AD1645 to AD1715. *Astron. Astrophys.* **276**, 549.
- Ringnes, T.S., Jensen, E.: 1960, On the Relation Between Magnetic Fields and Areas of Sunspots in the Interval 1917–56. *Astrophys. Norv.* **7**, 99.

- Rüdiger, G.: 1989, *Differential Rotation and Stellar Convection: Sun and Solar-Type Stars, Fluid Mechanics of Astrophysics and Geophysics*, Gordon and Breach Science Publishers, New York, USA.
- Rüdiger, G., Kitchatinov, L.L., Hollerbach, R.: 2013, *Magnetic Processes in Astrophysics: Theory, Simulations, Experiments*, Wiley-VCH, Weinheim, Germany.
- Sabine, E.: 1852, On Periodical Laws Discoverable in the Mean Effects of the Larger Magnetic Disturbances.-No. II. *Phil. Trans. R. Soc. Lond.* **142**, 103. doi:[10.1098/rstl.1852.0009](https://doi.org/10.1098/rstl.1852.0009).
- Sanchez, S., Fournier, A., Aubert, J.: 2014, The Predictability of Advection-Dominated Flux-Transport Solar Dynamo Models. *Astrophys. J.* **781**, 8. doi:[10.1088/0004-637X/781/1/8](https://doi.org/10.1088/0004-637X/781/1/8).
- Sarychev, A.P., Roshchina, E.M.: 2009, Comparison of Three Solar Activity Indices Based on Sunspot Observations. *Sol. Syst. Res.* **43**, 151. doi:[10.1134/S0038094609020087](https://doi.org/10.1134/S0038094609020087).
- Sayce, A.H.: 1877, *Babylonian Literature*, S. Bagster and Sons, London, UK.
- Schad, T.A., Penn, M.J.: 2010, Structural Invariance of Sunspot Umbrae over the Solar Cycle: 1993–2004. *Sol. Phys.* **262**, 19. doi:[10.1007/s11207-009-9493-8](https://doi.org/10.1007/s11207-009-9493-8).
- Schatten, K.H., Orosz, J.A.: 1990, Solar Constant Secular Changes. *Sol. Phys.* **125**, 179. doi:[10.1007/BF00154787](https://doi.org/10.1007/BF00154787).
- Scheiner, C.: 1630, *Rosa Ursina sive Sol*, Andreas Phaeus, Bracciano.
- Scheiner, C.: 1651, *Prodromus pro sole mobili et terra stabili*, Collegium Nissense Societatis Iesu, Nysa, Silesia.
- Schou, J., Antia, H.M., Basu, S., Bogart, R.S., Bush, R.I., Chitre, S.M., Christensen-Dalsgaard, J., Di Mauro, M.P., Dziembowski, W.A., Eff-Darwich, A., Gough, D.O., Haber, D.A., Hoeksema, J.T., Howe, R., Korzennik, S.G., Kosovichev, A.G., Larsen, R.M., Pijpers, F.P., Scherrer, P.H., Sekii, T., Tarbell, T.D., Title, A.M., Thompson, M.J., Toomre, J.: 1998, Helioseismic Studies of Differential Rotation in the Solar Envelope by the Solar Oscillations Investigation Using the Michelson Doppler Imager. *Astrophys. J.* **505**, 390. doi:[10.1086/306146](https://doi.org/10.1086/306146).
- Schrijver, C.J., Harvey, K.L.: 1994, The Photospheric Magnetic Flux Budget. *Sol. Phys.* **150**, 1. doi:[10.1007/BF00712873](https://doi.org/10.1007/BF00712873).
- Schrijver, C.J., Martin, S.F.: 1990, Properties of the Large- and Small-Scale Flow Patterns in and Around AR 19824. *Sol. Phys.* **129**, 95. doi:[10.1007/BF00154367](https://doi.org/10.1007/BF00154367).
- Schrijver, C.J., Siscoe, G.L.: 2010, *Heliophysics: Evolving Solar Activity and the Climates of Space and Earth*, Cambridge University Press, London, UK.
- Schrijver, C.J., Title, A.M.: 1999, Active Regions Losing Their Moorings by Subsurface Reconnection. *Sol. Phys.* **188**, 331. doi:[10.1023/A:1005281526160](https://doi.org/10.1023/A:1005281526160).
- Schrijver, C.J., Zwaan, C.: 2000, *Solar and Stellar Magnetic Activity*, Cambridge University Press, New York, USA.
- Schrijver, C.J., DeRosa, M.L., Title, A.M.: 2002, What is Missing from our Understanding of Long-Term Solar and Heliospheric Activity? *Astrophys. J.* **577**, 1006. doi:[10.1086/342247](https://doi.org/10.1086/342247).
- Schüssler, M., Rempel, M.: 2005, The Dynamical Disconnection of Sunspots from Their Magnetic Roots. *Astron. Astrophys.* **441**, 337. doi:[10.1051/0004-6361:20052962](https://doi.org/10.1051/0004-6361:20052962).
- Schwabe, S.: 1844, Sonnenbeobachtungen im Jahre 1843. Von Herrn Hofrath Schwabe in Dessau. *Astron. Nachr.* **21**, 233.

- Senthamizh Pavai, V., Arlt, R., Dasi-Espuig, M., Krivova, N.A., Solanki, S.K.: 2015, Sunspot Areas and Tilt Angles for Solar Cycles 7–10. *Astron. Astrophys.* **584**, A73. doi:[10.1051/0004-6361/201527080](https://doi.org/10.1051/0004-6361/201527080).
- Senthamizh Pavai, V., Arlt, R., Diercke, A., Denker, C., Vaquero, J.M.: 2016, Sunspot Group Tilt Angle Measurements from Historical Observations. *Adv. Space Res.* **58**, 1468. doi:[10.1016/j.asr.2016.03.002](https://doi.org/10.1016/j.asr.2016.03.002).
- Sestini, B.: 1853, *Observations on Solar Spots Made at the Observatory of Georgetown College*, C. Alexander, Washington, USA.
- Sheeley, N.R. Jr.: 2005, Surface Evolution of the Sun's Magnetic Field: A Historical Review of the Flux-Transport Mechanism. *Living Rev. Sol. Phys.* **2**, 5. doi:[10.12942/lrsp-2005-5](https://doi.org/10.12942/lrsp-2005-5).
- Sheeley, N.R. Jr., DeVore, C.R., Boris, J.P.: 1985, Simulations of the Mean Solar Magnetic Field During Sunspot Cycle 21. *Sol. Phys.* **98**, 219. doi:[10.1007/BF00152457](https://doi.org/10.1007/BF00152457).
- Sheeley, N.R. Jr., Nash, A.G., Wang, Y.M.: 1987, The Origin of Rigidly Rotating Magnetic Field Patterns on the Sun. *Astrophys. J.* **319**, 481. doi:[10.1086/165472](https://doi.org/10.1086/165472).
- Sivaraman, K.R., Gupta, S.S., Howard, R.F.: 1993, Measurement of Kodaikanal White-Light Images. I. A Comparison of 35 Years of Kodaikanal and Mount Wilson Sunspot Data. *Sol. Phys.* **146**, 27. doi:[10.1007/BF00662168](https://doi.org/10.1007/BF00662168).
- Sivaraman, K.R., Gupta, S.S., Howard, R.F.: 1999, Measurement of Kodaikanal White-Light Images - IV. Axial Tilt Angles of Sunspot Groups. *Sol. Phys.* **189**, 69. doi:[10.1023/A:1005277515551](https://doi.org/10.1023/A:1005277515551).
- Smogulecz, J., Schönberger, G.: 1626, *Sol Illustratus ac Propugnatus*, T. Meyer, Freiburg im Breisgau, Germany.
- Snodgrass, H.B.: 1983, Magnetic Rotation of the Solar Photosphere. *Astrophys. J.* **270**, 288. doi:[10.1086/161121](https://doi.org/10.1086/161121).
- Sokoloff, D., Khlystova, A.I.: 2010, The Solar Dynamo in the Light of the Distribution of Various Sunspot Magnetic Classes over Butterfly Diagram. *Astron. Nachr.* **331**, 82. doi:[10.1002/asna.200911300](https://doi.org/10.1002/asna.200911300).
- Sokoloff, D., Khlystova, A., Abramenko, V.: 2015, Solar Small-Scale Dynamo and Polarity of Sunspot Groups. *Mon. Not. R. Astron. Soc.* **451**, 1522. doi:[10.1093/mnras/stv1036](https://doi.org/10.1093/mnras/stv1036).
- Solanki, S.K.: 1993, Small-Scale Solar Magnetic Fields – an Overview. *Space Sci. Rev.* **63**, 1. doi:[10.1007/BF00749277](https://doi.org/10.1007/BF00749277).
- Solanki, S.K., Krivova, N.A.: 2003, Can Solar Variability Explain Global Warming Since 1970? *J. Geophys. Res.: Space Phys.* **108**, 1200. doi:[10.1029/2002JA009753](https://doi.org/10.1029/2002JA009753).
- Solanki, S.K., Schüssler, M., Fligge, M.: 2000, Evolution of the Sun's Large-Scale Magnetic Field Since the Maunder Minimum. *Nature* **408**, 445. doi:[10.1038/35044027](https://doi.org/10.1038/35044027).
- Solanki, S.K., Schüssler, M., Fligge, M.: 2002, Secular Variation of the Sun's Magnetic Flux. *Astron. Astrophys.* **383**, 706. doi:[10.1051/0004-6361:20011790](https://doi.org/10.1051/0004-6361:20011790).
- Solanki, S.K., Usoskin, I.G., Kromer, B., Schüssler, M., Beer, J.: 2004, Unusual Activity of the Sun During Recent Decades Compared to the Previous 11,000 Years. *Nature* **431**, 1084. doi:[10.1038/nature02995](https://doi.org/10.1038/nature02995).
- Spörer, F.W.G.: 1883, Resultate aus Beobachtungen der Sonnenflecken. *Astron. Nachr.* **107**, 331.

- Spörer, G.: 1889a, *Ueber die Periodicität der Sonnenflecken seit dem Jahre 1618*, Wilh. Engelmann, Leipzig, Germany.
- Spörer, G.: 1889b, *Ueber die Periodicität der Sonnenflecken seit dem Jahre 1618*. In: *Nova Acta der Ksl. Leop.-Carol.*, Blochmann & Sohn, Halle, Germany.
- Steenbeck, M., Krause, F., Rädler, K.H.: 1966, Berechnung der Mittleren Lorentz-Feldstärke $\overline{\mathbf{v} \times \mathfrak{B}}$ für ein Elektrisch Leitendes Medium in Turbulenter, Durch Coriolis-Kräfte Beeinflußter Bewegung. *Z. Naturforsch. A* **21**, 369. doi:[10.1515/zna-1966-0401](https://doi.org/10.1515/zna-1966-0401).
- Steinhilber, F.: 2010, Total Solar Irradiance Since 1996: Is There a Long-Term Variation Unrelated to Solar Surface Magnetic Phenomena? *Astron. Astrophys.*, A391–. doi:[10.1051/0004-6361/200811446](https://doi.org/10.1051/0004-6361/200811446).
- Stenflo, J.O., Kosovichev, A.G.: 2012, Bipolar Magnetic Regions on the Sun: Global Analysis of the SOHO/MDI Data Set. *Astrophys. J.* **745**, 129. doi:[10.1088/0004-637X/745/2/129](https://doi.org/10.1088/0004-637X/745/2/129).
- Stephenson, F.R., Willis, D.M., Hallinan, T.J.: 2004, Aurorae: The Earliest Datable Observation of the Aurora Borealis. *Astron. Geophys.* **45**, 6. doi:[10.1046/j.1468-4004.2003.45615.x](https://doi.org/10.1046/j.1468-4004.2003.45615.x).
- Stothers, R.: 1979, Solar Activity Cycle During Classical Antiquity. *Astron. Astrophys.* **77**, 121.
- Stuiver, M., Braziunas, T.F.: 1989, Atmospheric ^{14}C and Century-Scale Solar Oscillations. *Nature* **338**, 405. doi:[10.1038/338405a0](https://doi.org/10.1038/338405a0).
- Stuiver, M., Braziunas, T.F., Becker, B., Kromer, B.: 1991, Climatic, Solar, Oceanic, and Geomagnetic Influences on Late-Glacial and Holocene Atmospheric $^{14}\text{C}/^{12}\text{C}$ Change. *Quat. Res.* **35**, 1. doi:[10.1016/0033-5894\(91\)90091-l](https://doi.org/10.1016/0033-5894(91)90091-l).
- Svalgaard, L., Schatten, K.H.: 2016, Reconstruction of the Sunspot Group Number: The Backbone Method. *Sol. Phys.* **291**, 2653. doi:[10.1007/s11207-015-0815-8](https://doi.org/10.1007/s11207-015-0815-8).
- Taylor, P.O.: 1985, Computation of American Relative Sunspot Numbers. *J. Am. Assoc. Variable Star Obs.* **14**, 28.
- Tian, L., Liu, Y., Wang, H.: 2003, Latitude and Magnetic Flux Dependence of the Tilt Angle of Bipolar Regions. *Sol. Phys.* **215**, 281. doi:[10.1023/A:1025686305225](https://doi.org/10.1023/A:1025686305225).
- Tinsley, B.A., Zhou, L.: 2006, Initial Results of a Global Circuit Model with Variable Stratospheric and Tropospheric Aerosols. *J. Geophys. Res.: Atm.* **111**, D16205. doi:[10.1029/2005JD006988](https://doi.org/10.1029/2005JD006988).
- Tlatov, A.G.: 2013, Long-Term Variations in Sunspot Characteristics. *Geomag. Aeron.* **53**, 953. doi:[10.1134/S0016793213080264](https://doi.org/10.1134/S0016793213080264).
- Tlatov, A.G., Pevtsov, A.A.: 2014, Bimodal Distribution of Magnetic Fields and Areas of Sunspots. *Sol. Phys.* **289**, 1143. doi:[10.1007/s11207-013-0382-9](https://doi.org/10.1007/s11207-013-0382-9).
- Tlatov, A.G., Vasil'eva, V.V., Pevtsov, A.A.: 2010, Distribution of Magnetic Bipoles on the Sun over Three Solar Cycles. *Astrophys. J.* **717**, 357. doi:[10.1088/0004-637X/717/1/357](https://doi.org/10.1088/0004-637X/717/1/357).
- Tlatov, A.G., Vasil'eva, V.V., Makarova, V.V., Otkidychev, P.A.: 2014, Applying an Automatic Image-Processing Method to Synoptic Observations. *Sol. Phys.* **289**, 1403. doi:[10.1007/s11207-013-0404-7](https://doi.org/10.1007/s11207-013-0404-7).
- Trichtchenko, L., Boteler, D.H.: 2002, Modelling of Geomagnetic Induction in Pipelines. *Ann. Geophys.* **20**, 1063. doi:[10.5194/angeo-20-1063-2002](https://doi.org/10.5194/angeo-20-1063-2002).
- Tuominen, J., Kyrolainen, J.: 1982, On the Latitude Drift of Sunspot Groups and Solar Rotation. *Sol. Phys.* **79**, 161. doi:[10.1007/BF00146980](https://doi.org/10.1007/BF00146980).

- Ulrich, R.K.: 2010, Solar Meridional Circulation from Doppler Shifts of the Fe I Line at 5250 Å as Measured by the 150-Foot Solar Tower Telescope at the Mt. Wilson Observatory. *Astrophys. J.* **725**, 658. doi:[10.1088/0004-637X/725/1/658](https://doi.org/10.1088/0004-637X/725/1/658).
- Ulrich, R.K., Boyden, J.E., Webster, L., Padilla, S.P., Snodgrass, H.B.: 1988, Solar Rotation Measurements at Mount Wilson. V. Reanalysis of 21 Years of Data. *Sol. Phys.* **117**, 291. doi:[10.1007/BF00147250](https://doi.org/10.1007/BF00147250).
- Usoskin, I.G.: 2017, A History of Solar Activity over Millennia. *Living Rev. Sol. Phys.* **14**, 3. doi:[10.1007/s41116-017-0006-9](https://doi.org/10.1007/s41116-017-0006-9).
- Usoskin, I.G., Kovaltsov, G.A.: 2006, Cosmic Ray Induced Ionization in the Atmosphere: Full Modeling and Practical Applications. *J. Geophys. Res.: Atm.* **111**, D21206. doi:[10.1029/2006JD007150](https://doi.org/10.1029/2006JD007150).
- Usoskin, I.G., Mursula, K., Kovaltsov, G.A.: 2001, Was One Sunspot Cycle Lost in Late XVIII Century? *Astron. Astrophys.* **370**, L31. doi:[10.1051/0004-6361:20010319](https://doi.org/10.1051/0004-6361:20010319).
- Usoskin, I.G., Solanki, S.K., Kovaltsov, G.A.: 2007, Grand Minima and Maxima of Solar Activity: New Observational Constraints. *Astron. Astrophys.* **471**, 301. doi:[10.1051/0004-6361:20077704](https://doi.org/10.1051/0004-6361:20077704).
- Usoskin, I.G., Mursula, K., Arlt, R., Kovaltsov, G.A.: 2009, A Solar Cycle Lost in 1793–1800: Early Sunspot Observations Resolve the Old Mystery. *Astrophys. J. Lett.* **700**, L154. doi:[10.1088/0004-637X/700/2/L154](https://doi.org/10.1088/0004-637X/700/2/L154).
- Usoskin, I.G., Arlt, R., Asvestari, E., Hawkins, E., Käpylä, M., Kovaltsov, G.A., Krivova, N., Lockwood, M., Mursula, K., O'Reilly, J., Owens, M., Scott, C.J., Sokoloff, D.D., Solanki, S.K., Soon, W., Vaquero, J.M.: 2015, The Maunder Minimum (1645–1715) was Indeed a Grand Minimum: A Reassessment of Multiple Datasets. *Astron. Astrophys.* **581**, A95. doi:[10.1051/0004-6361/201526652](https://doi.org/10.1051/0004-6361/201526652).
- Usoskin, I.G., Kovaltsov, G.A., Lockwood, M., Mursula, K., Owens, M., Solanki, S.K.: 2016a, A New Calibrated Sunspot Group Series Since 1749: Statistics of Active Day Fractions. *Sol. Phys.* **291**, 2685. doi:[10.1007/s11207-015-0838-1](https://doi.org/10.1007/s11207-015-0838-1).
- Usoskin, I.G., Gallet, Y., Lopes, F., Kovaltsov, G.A., Hulot, G.: 2016b, Solar Activity During the Holocene: the Hallstatt Cycle and its Consequence for Grand Minima and Maxima. *Astron. Astrophys.* **587**, A150. doi:[10.1051/0004-6361/201527295](https://doi.org/10.1051/0004-6361/201527295).
- van Ballegoijen, A.A., Cartledge, N.P., Priest, E.R.: 1998, Magnetic Flux Transport and the Formation of Filament Channels on the Sun. *Astrophys. J.* **501**, 866. doi:[10.1086/305823](https://doi.org/10.1086/305823).
- van Driel-Gesztelyi, L., Green, L.M.: 2015, Evolution of Active Regions. *Living Rev. Sol. Phys.* **12**, 1. doi:[10.1007/lrsp-2015-1](https://doi.org/10.1007/lrsp-2015-1).
- Vaquero, J.M., Trigo, R.M.: 2015, Redefining the Limit Dates for the Maunder Minimum. *New Astron.* **34**, 120. doi:[10.1016/j.newast.2014.06.002](https://doi.org/10.1016/j.newast.2014.06.002).
- Vaquero, J.M., Vázquez, M.: 2009, *The Sun Recorded Through History: Scientific Data Extracted from Historical Documents, Astrophysics and Space Science Library* **361**, Springer, New York, USA. doi:[10.1007/978-0-387-92789-3](https://doi.org/10.1007/978-0-387-92789-3).
- Vaquero, J.M., Svalgaard, L., Carrasco, V.M.S., Clette, F., Lefèvre, L., Gallego, M.C., Arlt, R., Aparicio, A.J.P., Richard, J.G., Howe, R.: 2016, A Revised Collection of Sunspot Group Numbers. *Sol. Phys.* **291**, 3061. doi:[10.1007/s11207-016-0982-2](https://doi.org/10.1007/s11207-016-0982-2).
- Viereck, R., Puga, L., McMullin, D., Judge, D., Weber, M., Tobiska, W.K.: 2001, The Mg II Index: A Proxy for Solar EUV. *Geophys. Res. Lett.* **28**, 1343. doi:[10.1029/2000GL012551](https://doi.org/10.1029/2000GL012551).

- Waldmeier, M.: 1935, Neue Eigenschaften der Sonnenfleckenkurve. *Astron. Mitt. Eidg. Sternwarte Zurich* **14**, 105.
- Waldmeier, M.: 1939, Die Zonenwanderung der Sonnenflecken. *Astron. Mitt. Eidg. Sternwarte Zurich* **14**, 470.
- Wang, Y.M.: 2004, The Sun's Large-Scale Magnetic Field and its Long-Term Evolution. *Sol. Phys.* **224**, 21. doi:[10.1007/s11207-005-4982-x](https://doi.org/10.1007/s11207-005-4982-x).
- Wang, Y.M., Sheeley, N.R. Jr.: 1989, Average Properties of Bipolar Magnetic Regions During Sunspot Cycle 21. *Sol. Phys.* **124**, 81. doi:[10.1007/BF00146521](https://doi.org/10.1007/BF00146521).
- Wang, Y.M., Sheeley, N.R. Jr.: 1992, On Potential Field Models of the Solar Corona. *Astrophys. J.* **392**, 310. doi:[10.1086/171430](https://doi.org/10.1086/171430).
- Wang, Y.M., Lean, J., Sheeley, N.R. Jr.: 2000, The Long-Term Variation of the Sun's Open Magnetic Flux. *Geophys. Res. Lett.* **27**, 505. doi:[10.1029/1999GL010744](https://doi.org/10.1029/1999GL010744).
- Wang, Y.M., Lean, J.L., Sheeley, N.R. Jr.: 2005, Modeling the Sun's Magnetic Field and Irradiance Since 1713. *Astrophys. J.* **625**, 522. doi:[10.1086/429689](https://doi.org/10.1086/429689).
- Wang, Y.M., Nash, A.G., Sheeley, N.R. Jr.: 1989a, Evolution of the Sun's Polar Fields During Sunspot Cycle 21: Poleward Surges and Long-Term Behavior. *Astrophys. J.* **347**, 529. doi:[10.1086/168143](https://doi.org/10.1086/168143).
- Wang, Y.M., Nash, A.G., Sheeley, N.R. Jr.: 1989b, Magnetic Flux Transport on the Sun. *Science* **245**, 712. doi:[10.1126/science.245.4919.712](https://doi.org/10.1126/science.245.4919.712).
- Wang, Y.M., Colaninno, R.C., Baranyi, T., Li, J.: 2015, Active-Region Tilt Angles: Magnetic Versus White-Light Determinations of Joy's Law. *Astrophys. J.* **798**, 50. doi:[10.1088/0004-637X/798/1/50](https://doi.org/10.1088/0004-637X/798/1/50).
- Warnecke, J., Losada, I.R., Brandenburg, A., Kleorin, N., Rogachevskii, I.: 2013, Bipolar Magnetic Structures Driven by Stratified Turbulence with a Coronal Envelope. *Astrophys. J. Lett.* **777**, L37. doi:[10.1088/2041-8205/777/2/L37](https://doi.org/10.1088/2041-8205/777/2/L37).
- Watson, F.T., Fletcher, L., Marshall, S.: 2011, Evolution of Sunspot Properties During Solar Cycle 23. *Astron. Astrophys.* **533**, A14. doi:[10.1051/0004-6361/201116655](https://doi.org/10.1051/0004-6361/201116655).
- Weber, M.A., Fan, Y., Miesch, M.S.: 2011, The Rise of Active Region Flux Tubes in the Turbulent Solar Convective Envelope. *Astrophys. J.* **741**, 11. doi:[10.1088/0004-637X/741/1/11](https://doi.org/10.1088/0004-637X/741/1/11).
- Weber, M.A., Fan, Y., Miesch, M.S.: 2013, Comparing Simulations of Rising Flux Tubes Through the Solar Convection Zone with Observations of Solar Active Regions: Constraining the Dynamo Field Strength. *Sol. Phys.* **287**, 239. doi:[10.1007/s11207-012-0093-7](https://doi.org/10.1007/s11207-012-0093-7).
- Willamo, T., Usoskin, I.G., Kovaltsov, G.A.: 2017, Updated Sunspot Group Number Reconstruction for 1749–1996 Using the Active Day Fraction Method. *Astron. Astrophys.* **601**, A109. doi:[10.1051/0004-6361/201629839](https://doi.org/10.1051/0004-6361/201629839).
- Willis, D.M., Stephenson, F.R.: 2001, Solar and Auroral Evidence for an Intense Recurrent Geomagnetic Storm During December in AD 1128. *Sol. Phys.* **19**, 289. doi:[10.5194/angeo-19-289-2001](https://doi.org/10.5194/angeo-19-289-2001).
- Wilson, R.M.: 1998, A Comparison of Wolf's Reconstructed Record of Annual Sunspot Number with Schwabe's Observed Record of 'Clusters of Spots' for the Interval of 1826–1868. *Sol. Phys.* **182**, 217. doi:[10.1023/A:1005046820210](https://doi.org/10.1023/A:1005046820210).
- Wilson, R.M., Hathaway, D.H., Reichmann, E.J.: 1998, An Estimate for the Size of Cycle 23 Based on Near Minimum Conditions. *J. Geophys. Res.* **103**, 6595. doi:[10.1029/97JA02777](https://doi.org/10.1029/97JA02777).

-
- Wolf, R.: 1852, Liaison Entre Les Taches Du Soleil Et Les Variations en Déclinaison De L'aiguille Aimantée. *Comptes Rendus H. Acad. Sci.* **35**, 364.
- Yallop, B.D., Hohenkerk, C., Murdin, L., Clark, D.H.: 1982, Solar Rotation from 17th Century Records. *Qtlly. J. Roy. Astron. Soc.* **23**, 213.
- Zharkov, S., Zharkova, V.V., Ipson, S.S.: 2005, Statistical Properties of Sunspots in 1996–2004: I. Detection, North-South Asymmetry And Area Distribution. *Sol. Phys.* **228**, 377. doi:[10.1007/s11207-005-5005-7](https://doi.org/10.1007/s11207-005-5005-7).
- Zinner, E.: 1957, *In Neue Deutsche Biographie. Dritter Band, eds. O. Graf zu Stolberg-Wernigerode, et al.*, Duncker & Humblot, Berlin, Germany.
- Zolotova, N.V., Ponyavin, D.I.: 2015, The Maunder Minimum is not as Grand as it Seemed to be. *Astrophys. J.* **800**, 42. doi:[10.1088/0004-637X/800/1/42](https://doi.org/10.1088/0004-637X/800/1/42).
- Zolotova, N.V., Ponyavin, D.I., Arlt, R., Tuominen, I.: 2010, Secular Variation of Hemispheric Phase Differences in the Solar Cycle. *Astron. Nachr.* **331**, 765. doi:[10.1002/asna.201011410](https://doi.org/10.1002/asna.201011410).

Acknowledgments

Firstly, I would like to express my sincere gratitude to my supervisor Dr. Rainer Arlt for the continuous support, patient guidance, motivation, and immense knowledge he has shared during the course of my research. I am indebted to his willingness to spare his time so generously whenever I approach him. I could not have imagined having a better supervisor for my doctoral study. I would like to express my great appreciation and sincere thanks to apl. Prof. Carsten Denker, for his advice and meticulous assistance in keeping my progress on schedule. My sincere thanks to my mentor Dr. Adriane Liermann for all her support during these years.

I am particularly grateful to Prof. Sami K. Solanki, Dr. Robert Cameron, and Dr. Natalie Krivova at Max Planck Institute for Solar System Research, and Dr. Jie Jiang at Key Laboratory of Solar Activity, National Astronomical Observatories, Chinese Academy of Sciences, China for the fruitful discussions and special thanks to Dr. Robert Cameron and Dr. Jie Jiang for helping with the SFTM code. I express my warm gratitude to all my colleagues at the AIP who have made my doctoral journey pleasant. I would like to thank Andrea Diercke and Dr. Philipp Gast for proof-reading the bibliography and German abstract, respectively. I would like to thank Julian Kern for inspecting the spots in Schwabe's magnified drawings, Regina v. Berlepsch for digitizing the Rosa Ursina by Christoph Scheiner in the library of Leibniz Institute for Astrophysics Potsdam, Nadya Zolotova from Sankt Petersburg for drawing our attention to [Scheiner \(1651\)](#), Ralph Neuhäuser from Jena University for many helpful comments, and to Daniela Luge from Jena University for translating some Latin phrases. I would also like to thank each and everyone who worked on the digitization of sunspot drawings and extraction of sunspot data sets. I am also indebted to all my teachers and professors who have been the pillars to my academic progress.

I wish to acknowledge the financial grant provided by the German *Deutsche Forschungsgemeinschaft*, *DFG* project number Ar 355/10-1 with which this thesis work was carried out.

My acknowledgment would stand incomplete if I do not mention the affection, motivation, patience, and trust I was blessed with through my parents Mr. K. Valliappan and Mrs. V. Parimala and my siblings for their support. I feel very privileged to have beloved family and friends, without whose help and support I could have never succeeded in this adventure. My special thanks to Appa, Prati, Priya, Nethra, and Vaishu for proof-reading the thesis.

Appendix A – List of acronyms

AAVSO	American Association of Variable Star Observers
AIP	Leibniz-Institut für Astrophysik Potsdam
ARSN	American Relative Sunspot Number
AU	Astronomical Unit
BMR	Bipolar Magnetic Regions
CDS	Centre de Données astronomiques de Strasbourg
CIR	Corotating Interaction Region
CMD	Central Meridian Distance
CME	Coronal Mass Ejection
EUV	Extreme Ultra-Violet
FWHM	Full Widths at Half-Maximum
GCR	Galactic Cosmic Ray
GPS	Global Positioning System
GSN	Group Sunspot Number
IDL	Interactive Data Language
IMF	Interplanetary Magnetic Field
ISN	International Sunspot Number
MDI	Michelson Doppler Imager
MHD	Magnetohydrodynamic
MPS	Max Planck Institute for Solar System Research
MSD	Millionths of the Solar Disk
MSH	Millionths of the Solar Hemisphere
NOAA	National Oceanic and Atmospheric Administration
POLSP	Polarity Separation
RGO	Royal Greenwich Observatory
SEM	Standard Error of the Mean
SEP	Solar Energetic Particle
SFTM	Surface Flux Transport Model
SMF	Solar Magnetic Field
SOHO	Solar and Heliospheric Observatory
SOON	Solar Optical Observing Network
TSI	Total Solar Irradiance
USAF	U.S. Air Force
WDC-SILSO	World Data Center – Sunspot Index and Long-term Solar Observations
WSN	Wolf Sunspot Number